AD-A142 690   MODEL CLOUD RELATIONSHIPS(U) COLORADO STATE *UNIV FORT*   *1/2*
COLLINS DEPT OF ATMOSPHERIC SCIENCE   W R COTTON *ET AL.*
30 OCT 83 AFGL-TR-84-0028 F19628-82-K-0003

UNCLASSIFIED   F/G *4/2*   NL

MICROCOPY RESOLUTION TEST CHART

NATIONAL BUREAU OF STANDARDS 1963 A

AFGL-TR-84-0028

MODEL CLOUD RELATIONSHIPS

William R. Cotton
Edward E. Hindman
Gregory Tripoli
Ray L. McAnelly
C. Chen
C. Tremback
P. Flatau
K. Knupp

Department of Atmospheric Sciences
Colorado State University
Ft. Collins, Colorado 80523

Final Report
26 November 1981 - 30 September 1983

October 30, 1983

Approved for public release; distribution unlimited

AIR FORCE GEOPHYSICS LABORATORY
AIR FORCE SYSTEMS COMMAND
UNITED STATES AIR FORCE
HANSCOM AFB, MASSACHUSETTS 01731

DTIC
SELECTED
JUL 0 6 1984
E

84 07 05 051

This report has been reviewed by the ESD Public Affairs Office (PA) and is releasable to the National Technical Information Service (NTIS).

"This technical report has been reviewed and is approved for publication"
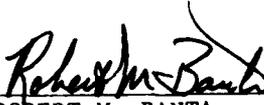
ROBERT M. BANTA
Contract Manager

ARNOLD A. BARNES, JR.
Chief, Cloud Physics Branch

FOR THE COMMANDER

ROBERT A. McCLATCHEY
Director, Atmospheric Sciences Division

REPORT DOCUMENTATION PAGE

1a. REPORT SECURITY CLASSIFICATION Unclassified			1b. RESTRICTIVE MARKINGS			
2a. SECURITY CLASSIFICATION AUTHORITY			3. DISTRIBUTION/AVAILABILITY OF REPORT Approved for Public Release; Distribution Unlimited			
2b. DECLASSIFICATION/DOWNGRADING SCHEDULE						
4. PERFORMING ORGANIZATION REPORT NUMBER(S)			5. MONITORING ORGANIZATION REPORT NUMBER(S) AFGL-TR-84-0028			
6a. NAME OF PERFORMING ORGANIZATION Department of Atmospheric Sciences, Colorado State Univ.		6b. OFFICE SYMBOL (If applicable)	7a. NAME OF MONITORING ORGANIZATION Air Force Geophysics Laboratory			
6c. ADDRESS (City, State and ZIP Code) Ft Collins, Colorado 80523			7b. ADDRESS (City, State and ZIP Code) Hanscom AFB Massachusetts 01731 Contract Manager: Robert Banta/LYC			
8a. NAME OF FUNDING/SPONSORING ORGANIZATION		8b. OFFICE SYMBOL (If applicable)	9. PROCUREMENT INSTRUMENT IDENTIFICATION NUMBER F19628-82-K-0003			
8c. ADDRESS (City, State and ZIP Code)			10. SOURCE OF FUNDING NOS.			

			PROGRAM ELEMENT NO.	PROJECT NO.	TASK NO.	WORK UNIT NO.
11. TITLE (Include Security Classification) Model Cloud Relationships						

12. PERSONAL AUTHOR(S) William R. Cotton, Edward E. Hindman, Gregory Tripoli, Ray L. McAnelly, C. Chen, C. Tremback, P. Flatau, K. Knupp

13a. TYPE OF REPORT Final	13b. TIME COVERED FROM 26 Nov 81 TO 30 Sep 83	14. DATE OF REPORT (Yr., Mo., Day) 1983 October 30	15. PAGE COUNT 152

16. SUPPLEMENTARY NOTATION

17. COSATI CODES			18. SUBJECT TERMS (Continue on reverse if necessary and identify by block number)
FIELD	GROUP	SUB. GR.	Radar Reflectivity; Precipitation Size-Spectra
			Cloud Model Predictions;
			Ice Microphysics;

19. ABSTRACT (Continue on reverse if necessary and identify by block number)
The two-year study involved a series of investigations which are summarized below.

Radar Reflectivity Studies

The factors contributing to the variability of radar reflectivity - water content relationships are investigated using a combination of numerical simulations using the 3-D cloud/mesoscale model and field measurements. It was found that model predictions of reflectivities due to ice crystals are inaccurate due to a lack of information on predicting the concentrations of ice crystals in cloud. In contrast, it was found that model-predicted PPI and RHI reflectivities compared favorably to measured reflectivities for Florida cumulus. Raindrops and graupel particles caused the measured reflectivities; ice crystals contributed negligibly. The model predicted reflectivities were deemed sufficiently accurate, from the Florida comparison, to investigate the causes for the variability in water content-radar reflectivity relationships.

20. DISTRIBUTION/AVAILABILITY OF ABSTRACT UNCLASSIFIED/UNLIMITED ☐ SAME AS RPT. ☐ DTIC USERS ☐	21. ABSTRACT SECURITY CLASSIFICATION UNCLASSIFIED	
22a. NAME OF RESPONSIBLE INDIVIDUAL Robert Banta	22b. TELEPHONE NUMBER (Include Area Code) (617) 861-2943	22c. OFFICE SYMBOL AFGL/LYC

DD FORM 1473, 83 APR   EDITION OF 1 JAN 73 IS OBSOLETE   Unclassified

Aircraft simulated 'penetrations' of cumulus clouds using the 3-D model revealed regions near cloud edge where water contents were low and reflectivities were high due to the presence of a few large graupel particles. This finding was supported by an analysis of aircraft penetrations of northeast Colorado hailstorms.

Additional analysis of these hailstorm data revealed a relationship between water-content (M) and reflectivity (Z) of M (gm^{-3}) = 0.065 $Z^{0.196}$ $(m^6 m^{-3})$. The exponent of 0.196 varies from more common 0.5 to 1.0 values due to the presence of large hail. The Marshall-Palmer size distribution used in the 3-D model causes M to be proportional to $Z^{1.0}$. Hence, the 3-D model is not able to simulate reflectivities in hailstorms.

Aircraft Icing Studies

The 3-D cloud/mesoscale model was adapted to simulate, in an orographic cloud, the production of liquid water and the removal by various ice crystal processes. To adapt the model, an ice crystal nucleation parameterization, an ice crystal aggregation parameterization and an ice crystal removal parameterization were developed. Preliminary simulations have revealed an interesting relationship between ice crystal nucleation and the existence of supercooled water. The production of aggregates also affected the existence of liquid water because they removed large numbers of ice crystals and thus affected the overall balance.

One-Dimensional Cloud/Turbulence Model Investigations

The theory of the one dimensional cloud/turbulence model, which satisfactorily simulates many features of the cloud-capped atmospheric boundary layer, was extended to include ice processes. As a result of this investigation, a simplified model was being developed.

Hydrostatic Mesoscale Model Investigations

The non-hydrostatic 3D cloud/mesoscale model was successfully adapted to a hydrostatic mesoscale model. The hydrostatic mesoscale model provides greater computational efficiency for large-scale simulations. A data assimilation and analysis package was developed to initialize the hydrostatic model with standard meteorological measurements.

Investigations of Wind Shears Produced by Precipitating Convective Clouds

Strong, transient, low-level wind shears were analyzed from data collected in South Park, Colorado and Miles City, Montana thunderstorms. Model simulations based on the data, reveal similar wind shear and the causal processes. The shears are primarily associated with thunderstorm outflow regions which were driven by precipitation.

Recent Change in the 3-D Cloud/Mesoscale Model Sent to Kirtland AFB.

Recent changes, which improved the current model formulation are detailed.

1.0 Summary of the Report

The two-year study involved a series of investigations which are summarized below.

1.1 Radar Reflectivity Studies

The factors contributing to the variability of radar reflectivity – water content relationships are investigated using a combination of numerical simulations using the 3-D cloud/mesoscale model and field measurements. It was found that model predictions of reflectivities due to ice crystals are inaccurate due to a lack of information on predicting the concentrations of ice crystals in cloud. In contrast, it was found that model-predicted PPI and RHI reflectivities compared favorably to measured reflectivities for Florida cumulus. Raindrops and graupel particles caused the measured reflectivities; ice crystals contributed negligibly. The model-predicted reflectivities were deemed sufficiently accurate, from the Florida comparison, to investigate the causes for the variability in water content-radar reflectivity relationships.

Aircraft simulated 'penetrations' of cumulus clouds using the 3-D model revealed regions near cloud edge where water contents were low and reflectivities were high due to the presence of a few large graupel particles. This finding was supported by an analysis of aircraft penetrations of northeast Colorado hailstorms.

Additional analysis of these hailstorm data revealed a relationship between water-content (M) and reflectivity (Z) of M (gm^{-3}) = 0.065 $Z^{0.196}$ $(m^6 m^{-3})$. The exponent of 0.196 varies from more common 0.5 to 1.0 values due to the presence of large hail. The Marshall-Palmer size distribution used in the 3-D model causes M to be proportional to $Z^{1.0}$.

Hence, the 3-D model is not able to simulate reflectivities in hailstorms.

1.2 Aircraft Icing Studies

The 3-D cloud/mesoscale model was adapted to simulate, in an orographic cloud, the production of liquid water and the removal by various ice crystal processes. To adapt the model, an ice crystal nucleation parameterization, an ice crystal aggregation parameterization and an ice crystal removal parameterization were developed. Preliminary simulations have revealed an interesting relationship between ice crystal nucleation and the existence of supercooled water. The production of aggregates also affected the existence of liquid water because they removed large numbers of ice crystals and thus affected the overall balance.

1.3 One-Dimensional Cloud/Turbulence Model Investigations

The theory of the one dimensional cloud/turbulence model, which satisfactorily simulates many features of the cloud-capped atmospheric boundary layer, was extended to include ice processes. As a result of this investigation, a simplified model was being developed.

1.4 Hydrostatic Mesoscale Model Investigations

The non-hydrostatic 3D cloud/mesoscale model was successfully adapted to a hydrostatic mesoscale model. The hydrostatic mesoscale model provides greater computational efficiency for large-scale simulations. A data assimilation and analysis package was developed to initialize the hydrostatic model with standard meteorological measurements.

1.5 Investigations of Wind Shears Produced by Precipitating Convective Clouds

Strong, transient, low-level wind shears were analyzed from data collected in South Park, Colorado and Miles City, Montana thunderstorms. Model simulations based on the data, reveal similar wind shear and the causal processes. The shears are primarily associated with thunderstorm outflow regions which were driven by precipitation.

1.6 Recent Change in the 3-D Cloud/Mesoscale Model Sent to Kirtland AFB.

Recent changes, which improved the current model formulation are detailed.

2.0 Introduction

The estimation of water contents of clouds using conventional radar has become important, recently, because zones of high liquid water contents may result in the destruction of aerospace vehicles upon re-entry into the troposphere. Empirical relationships between the liquid (or ice) water content of precipitation (M) and radar reflectivity (Z) generally have been derived for cloud systems with one predominant precipitation phase (eg., either ice or water). Recently, Plank et al. (1980) have presented empirical M-Z relationships for ice hydrometeors using data collected from new electro-optic sensors (Knollenberg, 1970).

In this study we investigated M-Z relationships in mixed-phase clouds. We employed both measured M-Z relationships and relationships predicted using the three-dimensional cloud/mesoscale numerical simulation of Tripoli and Cotton (1982). A unique feature of this research was the coupling of measured and simulated M-Z relationships. Using this approach, it was found that much of the variability in the relationships can be explained.

2.1 Objectives

The initial objectives of the proposal (for the period November 1981 through March 1983) were as follows:

* To compare model-predicted liquid water (M) - radar reflectivity
  (Z) relationships with measured M-Z relationships from Florida,
  Colorado and Montana cumulus clouds.

* To determine the dominant factors contributing to the
  variability in M-Z relationships using model-predicted and
  measured data.

The final objectives of the project (for the period November 1982 to September 1983) were as follows:

- Use the 3-D cloud/mesoscale model to define potential regions for aircraft icing.

- Determine the feasibility of adapting the existing 1-D cloud/turbulence model to include ice processes and modify the model accordingly.

- Expand the CSU 3-D cloud model into a hydrostatic mesoscale model to study regional cloud formations with application to predictions of EM energy propagation, low-level wind fields atmospheric transport, etc.

- Investigate causes of extreme wind shears in the atmosphere

- Descriptions of the updates to the CSU cloud/mesoscale mode which is currently installed on the Kirtland AFB computer for AFGL/LYC use.

3.0 Radar Reflectivity Studies

3.1 Model Predicted Radar Reflectivity

As our first step in analyzing the variability of liquid water (M) versus radar reflectivity (Z), we have introduced algorithms in the 3D model to analyze and display radar reflectivity. The details of the algorithms are given in the Appendix (section 3.6). The standard definition of radar reflectivity is of the form

$$Z = \sum_{vol} n_i D_i^6 \quad , \tag{3.1}$$

where n_i represents the concentration of scattering elements per unit volume of diameter D_i. This definition, however, does not include any effects of the phase of the scattering elements which modulate the amplitude of the complex index of refraction.

Therefore, we defined a complex index of refraction-weighted reflectivity $\tilde{Z}$ such that

$$\tilde{Z} = |k|^2 \sum_{vol} n_i D_i^6 \tag{3.2}$$

where we assume $|k|^2$ is 0.93×10^{12} for liquid particles and 0.19×10^{12} for ice particles. Ice particles in the melting zone are assumed to be water-coated and therefore have a $|k|^2$ of 0.93×10^{12}. (The 10^{12} is a unit conversion factor such that if D_i is in cm and n_i in cm^{-3}, $\tilde{Z}$ is in $mm^6 m^{-3}$.)

By using $\tilde{Z}$ we can examine the effects of particle size distributions and the phase of precipitation elements on the variability of M vs. $\tilde{Z}$ relationships.

In the 3D model analysis we introduced algorithms for computing the

modified reflectivity for raindrops Z_r, graupel particles Z_g, ice crystals Z_i, and aggregates Z_a. Under the assumed particle size distribution functions in the model, the reflectivities for the individual components are as follows.

For raindrops,

$$\tilde{Z}_r = \frac{2^6 \; \Gamma(7) \; r_m^3}{8\pi \; \rho_w} \; \rho_o |k_1|^2 \; r_r = 1.7\mathrm{x}10^{15} \; R_m \; \rho_o \; \bar{r}_r \qquad (3.3)$$

where R_m is a characteristic drop radius for the distribution, ρ_w is the density of water, ρ_o index of refraction and r_r is the mixing ratio of raindrops.

For graupel,

$$\tilde{Z}_g = \frac{\Gamma(7)\rho_o D_{mg}^3}{\pi \rho_g} \; |k_i|^2 (1+H(T-273.16)*3.9) r_g$$

$$= 4.35\mathrm{x}10^{13}(1+H(T-273.16)*3.9)D_{mg}^3 \frac{\rho_o \bar{r}_g}{\rho_g} \qquad (3.4)$$

where ρ_g is the density of a graupel particle, D_{mg} is the characteristic diameter of graupel, $|k_i|^2$ is the ice-phase complex index of refraction, T is temperature, $H(x)$ is the heaviside-step function and r_g is the mixing ratio of graupel particles. Note, the formulation differs from the first quarterly report due to recent reformulation of the assumed graupel distribution from the assumption of constant concentration to the assumption of constant mean diameter.

For ice crystals

$$\tilde{Z}_i = |k_i|^2 N_i d_i^6 \qquad (3.5)$$

where N_i is the ice crystal concentration and d_i is the diameter of the ice crystals.

For aggregates,

$$\tilde{Z}_a = \frac{\Gamma(7) D_{ma}^3}{\pi \rho_{ag}} \rho_o |k_i|^2 [1 + 3.9 H (T - 273.16)] \bar{r}_a$$

$$= 2.9 \times 10^{15} [1 + 3.9 H (T - 273.16)] D_{ma}^{3.6} \rho_o \bar{r}_a \qquad (3.6)$$

where D_{ma} is the characteristic diameter of aggregates, $|k|^2$ is the ice-phase complex index of refraction, r_a is the mixing ratio of aggregate particles and ρ_{ag} is the aggregate density given by

$$\rho_{ag} = 0.015 \, D_{ma}^{0.6} \quad . \qquad (3.7)$$

The total reflectivity factor $\tilde{Z}_T$ was assumed to be

$$\tilde{Z}_T = \tilde{Z}_g + \tilde{Z}_i + \tilde{Z}_a \qquad (3.8)$$

This can be compared with the total mass-density of all precipitation elements (M_T) given by:

$$M_T = \rho_o (r_r + r_g + r_i + r_a) \qquad (3.9)$$

3.2 Simulations of a South Park, Colorado Thunderstorm

The analysis procedure was applied to data obtained from the simulation of a quasi-steady storm observed during the 1977 South Park

Area Cumulus Experiment (SPACE). The 3D model was used to predict $\bar{r}_r$, $\bar{r}_i$ and $\bar{r}_g$ and the corresponding reflectivities. Figure 3.1a,b,c show the fields of reflectivity for rainwater, graupel and ice crystals, respectively in units of dBZ, i.e., $10 \log_{10} (Z)$. Figure 3.2 shows the resultant total field of reflectivity or $\tilde{Z}_p$ in dBZ. The total reflectivity field shows the combined influence of graupel particles in the main updraft region of the storm and ice crystals in the outflow region at about the 6.5 km level in the rear quadrant of the simulated storm.

These illustrations (Fig. 3.1 and 3.2) demonstrate some of the problems encountered when trying to use the 3D model to predict radar reflectivity. Clearly the peak 55 dBZ obtained for graupel in Fig. 3.1b is realistic and, in fact, compares well with radar measurements made on that day. The rain radar reflectivities in Fig. 3.1a also look realistic although their peaks are confined to very close to the ground. The ice crystal reflectivities, however, demonstrate a major problem with the reflectivity predictions. As we can see in Fig. 3.1c, the reflectivity generally increases downward until a sharp cut off at the melting zone where we assume the crystals melt simultaneously. This reduction in reflectivity is because we are diagnosing the crystal concentration from the Fletcher temperature-concentration relationship which gives approximately a one order of magnitude decrease in concentration for each $4^\circ C$ rise in temperature. Therefore, ice crystal populations produced near $-20^\circ C$ which settle to the melting zone decrease strongly in number and therefore their diagnosed size increases strongly. Since Z_i is proportional to D_i^6, a very strong increase in dBZ is predicted. So strong is this effect, that the Z_i actually completely

19 JULY,1977 SØUTH PARK, CØLØRADØ
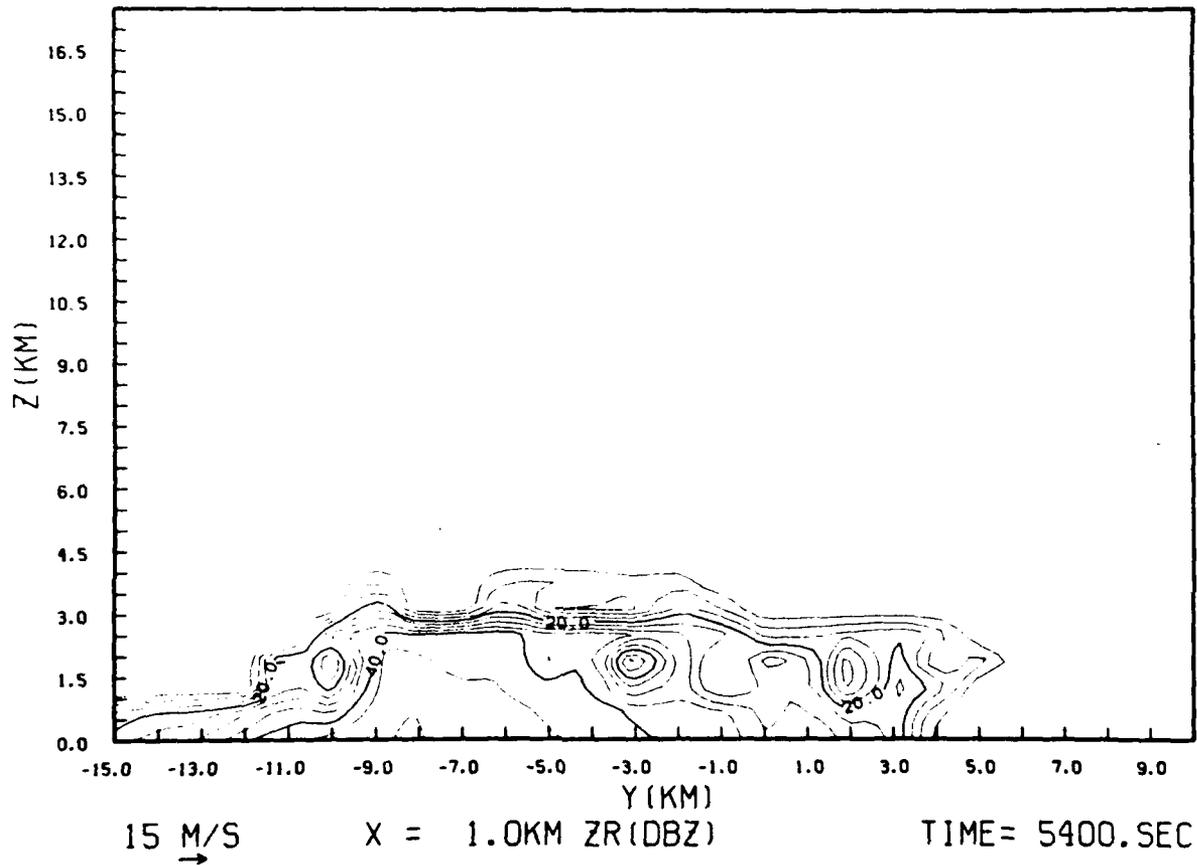
Figure 3.1a: $\tilde{Z}$ for raindrops at 5400s of simulated time. The contour interval is 5 dBZ.
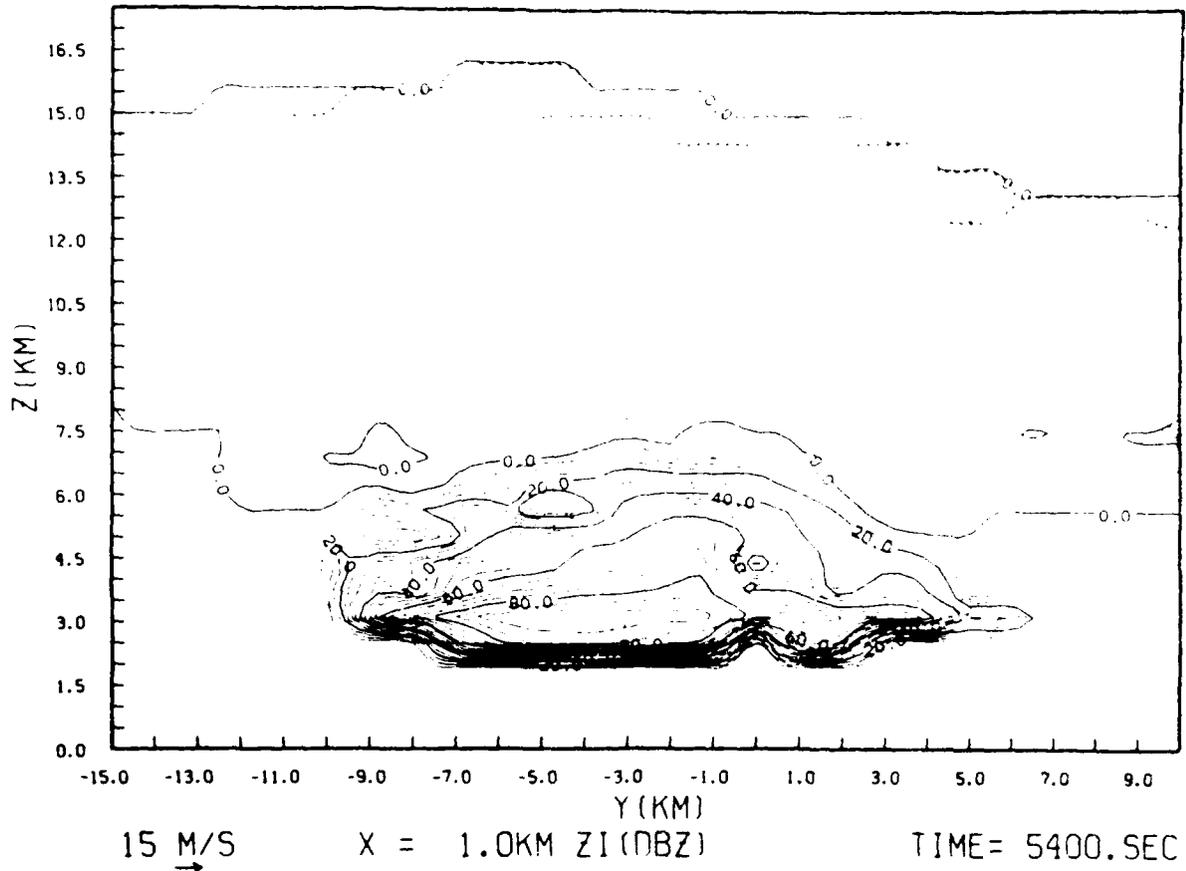
Figure 3.1b: Same as 3.1a except for ice crystals.

19 JULY.1977 SOUTH PARK. COLORADO
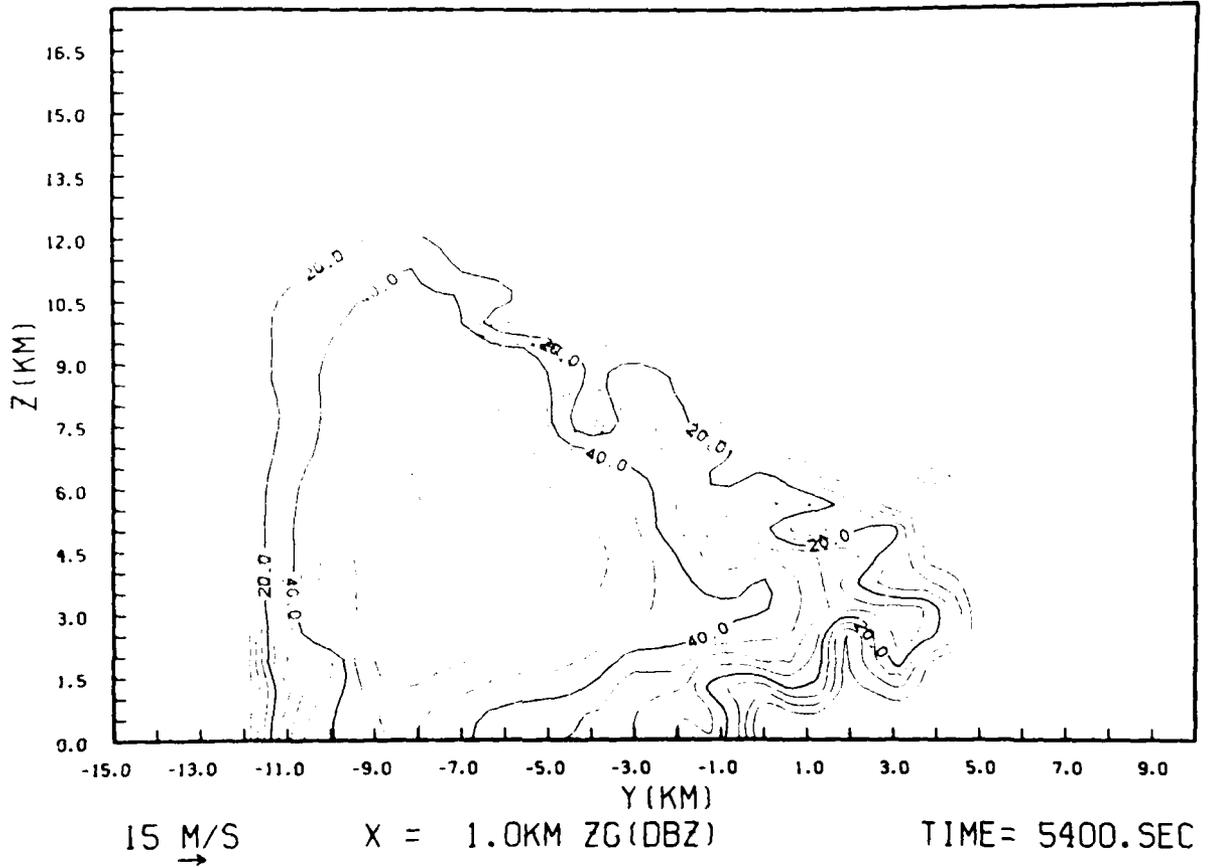
Figure 3.1c: Same as 3.1a except for graupel.

dominates the total reflectivities just above the melting zone.

We thought this problem would be overcome with the prediction of ice crystal concentration, since large numbers of crystals higher in the cloud would lower the mean sizes below. The implementation of a crystal prediction has been accomplished in our orographic cloud study. The results of ice crystals reflectivities produced in that study are shown in Figure 3.2a. In this wintertime case, the freezing level is near the ground. Although the dominating tendency for Z_i to be simply a function of temperature is absent, we now find the existence of random pockets of unrealistically high Z_i values coexisting with realistic Z_i values. The random pockets occur most often on the cloud boundaries. We can explain these results as follows: Unlike all other quantities predicted in the model, N_i is poorly behaved. Whereas $\overline{r_i}$ may vary by one order of magnitude in the cloudy region, N_i may vary by 5-10 orders of magnitude. Consequently, the meaningful prediction of transport and diffusion of N_i on a finite difference grid will be much less accurate than for the prediction of r_i especially in regions where N_i is changing sharply. Such regions are most often at the cloud boundaries. It, therefore, appears that the prediction of N_i improves Z_i predictions in the cloud interior, but leads to unacceptably noisy and large dBZ patterns near the boundary of the ice crystal region. These problems with ice crystal concentration predictions are less severe for the prediction of crystal mixing ratios since the noisy regions usually have very small ice contents. However, the predictions will have left us with an unreliable M-Z relationship for ice crystals, near the cloud boundaries, although realistic predictions appear possible in the cloud interior.

19 JULY.1977 SOUTH PARK. COLORADO

15 M/S   X = 1.0KM ZP(DBZ)   TIME= 5400.SEC
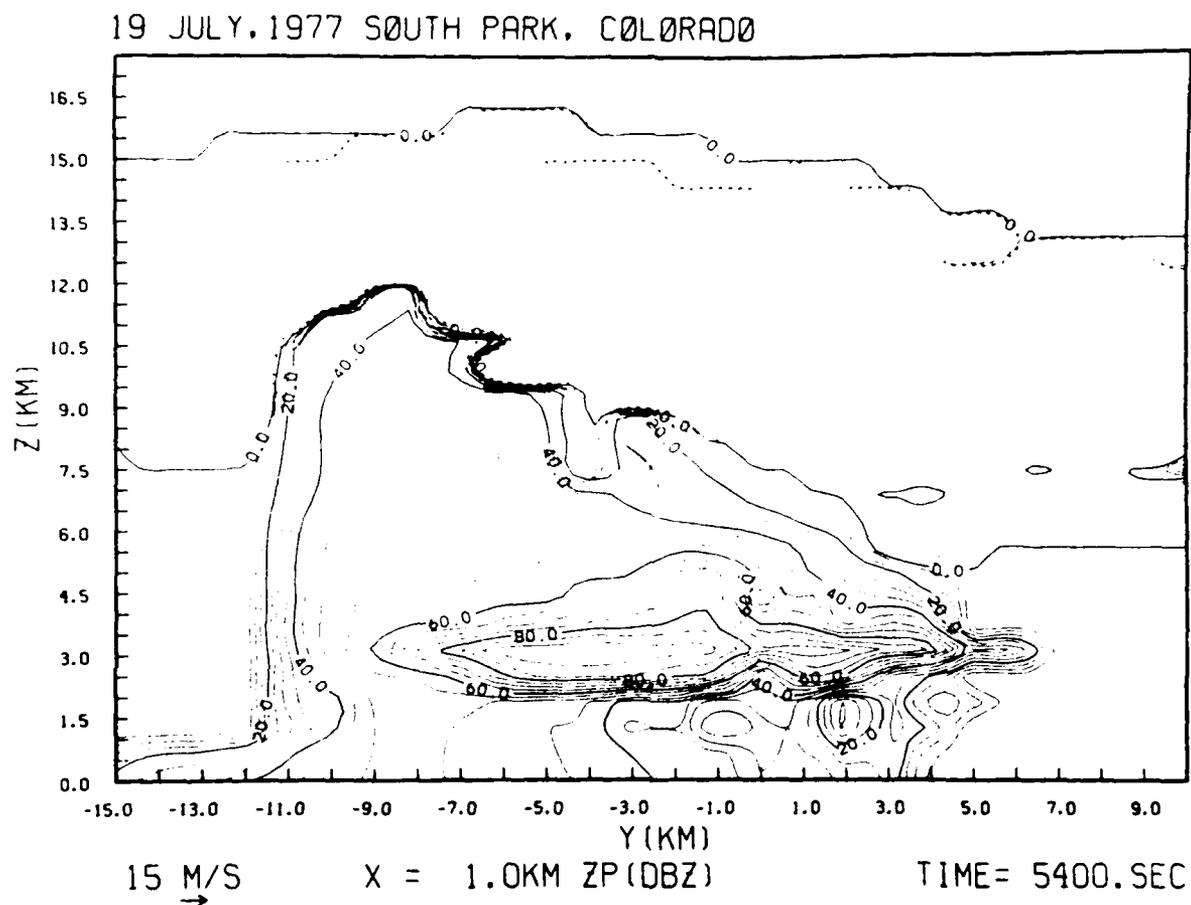
Figure 3.2a: Total reflectivity for all precipitation elements.
               Contour interval is 5 dBZ.

HAYDEN 24 NØVEMBER. 1979
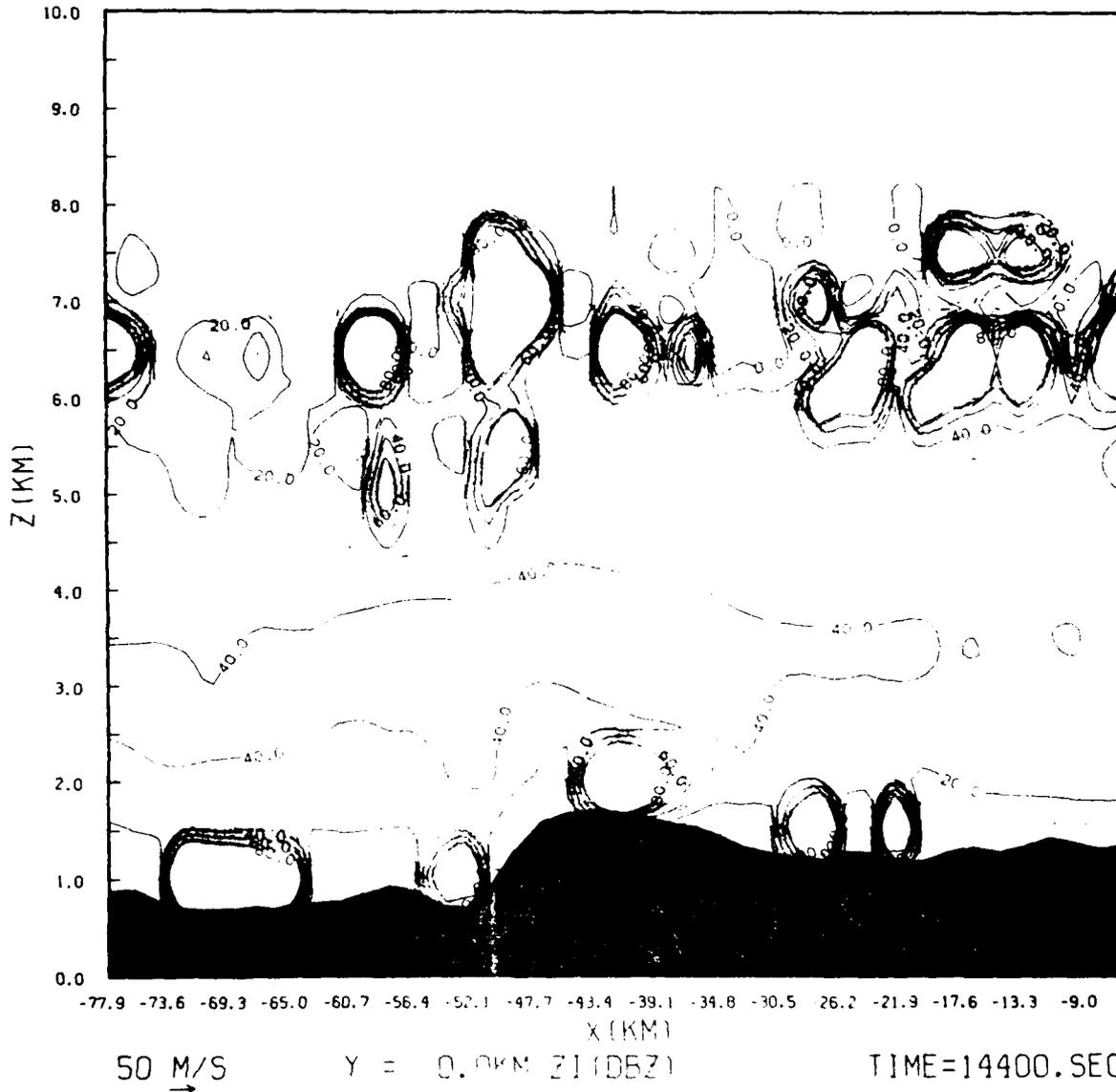
Figure 3.2b: Ice crystal reflectivities for ice crystals when N_i is predicted. Contour intervals are 5 dBZ.

3.3 Measured and Predicted Radar Reflectivities for Florida Cumulus

The measured radar reflectivities were obtained from the University of Miami Doppler radar courtesy of John Cunning (1981, personal communication). Cunning reported the radar was simultaneously operated with the similar NCAR CP-4 radar (prime calibration, signal generation) and the UM radar values were adjusted to the CP-4 values. Cunning et al. (1979) presents a brief discussion of the visual appearance of the investigated clouds on 25 August 1975 as well as the PPI radar characteristics. Here, we present the PPI reflectivity values with superimposed flight tracks of the sampling aircraft (NOAA-C130) in Fig. 3.3.

The measured reflectivity (Z) values were obtained from Fig. 3.3 using the following procedure. Particle spectra shown in Fig. 3.4 were derived from the entire aluminum foil sample for a penetration of the C-130 aircraft, hence producing an average spectrum and water content (M) for a particular penetration. Consequently, it was not possible to correlate "M" values with "Z" values as they varied along a penetration path. Instead, area-averaged "Z" values along a penetration path were determined from Fig. 3.3. The results are listed in Table 3.1. It can be seen by inspecting Fig. 3.3 for peak "Z" values and Table 3.1 for area-averaged "Z" values, that the peak values ranged from 30 to 50 dBZ while the average values range from 18 to 30 dBZ.

The calculated and predicted radar reflectivity values were obtained from, respectively, the particle spectra in Fig. 3.4 and from the three-dimensional numerical simulations of Levy (1982).
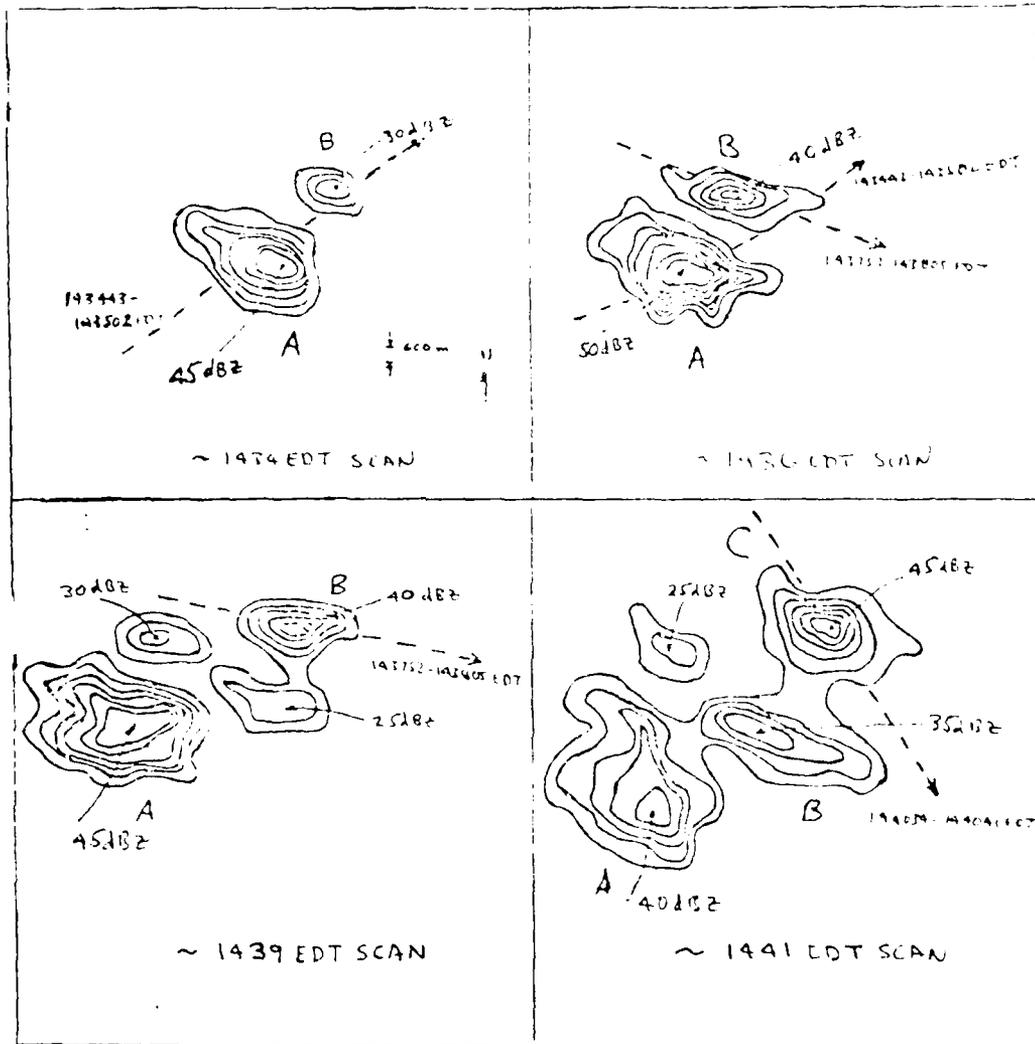
Figure 3.3: Radar reflectivity values (dBZ) measured on 25 August 1975 in South Florida. The initial contour corresponds to 15 dBZ, with 5 dBZ increments thereafter. The aircraft penetrations are given by the dashed lines with corresponding beginning and ending times. The PPI radar images are from the 6 km level and the approximate scan times are given.
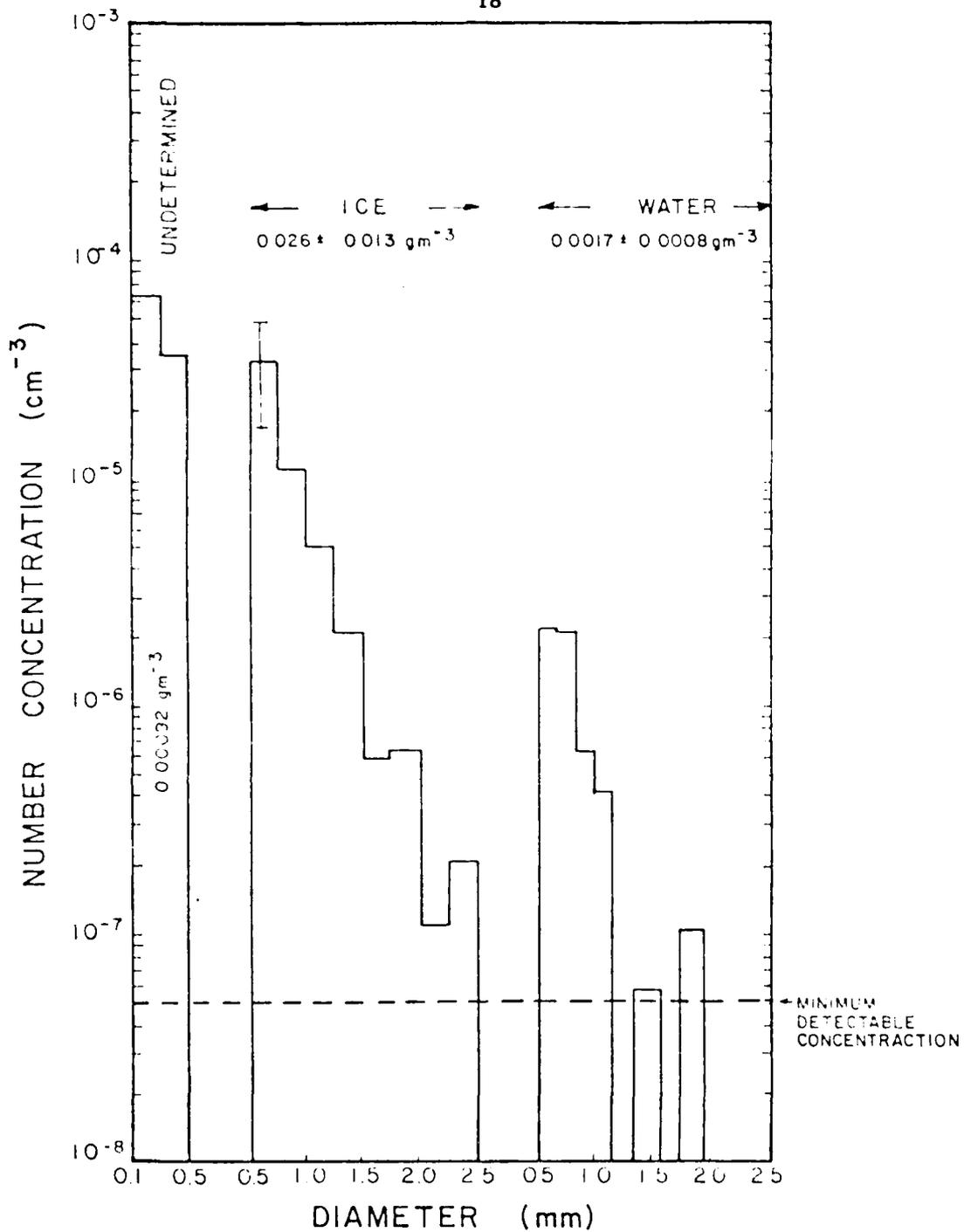
Figure 3.4a: Size distributions of ice and liquid particles at the -10°C level in a Florida cumulus tower, 25 August 1975, 143443 to 143507 EDT. The undetermined particles are either ice or water or both. The water contents derived from the size distributions are given. The size distributions and water contents are accurate to ± 50%, based on the data reduction strategy discussed in the text.
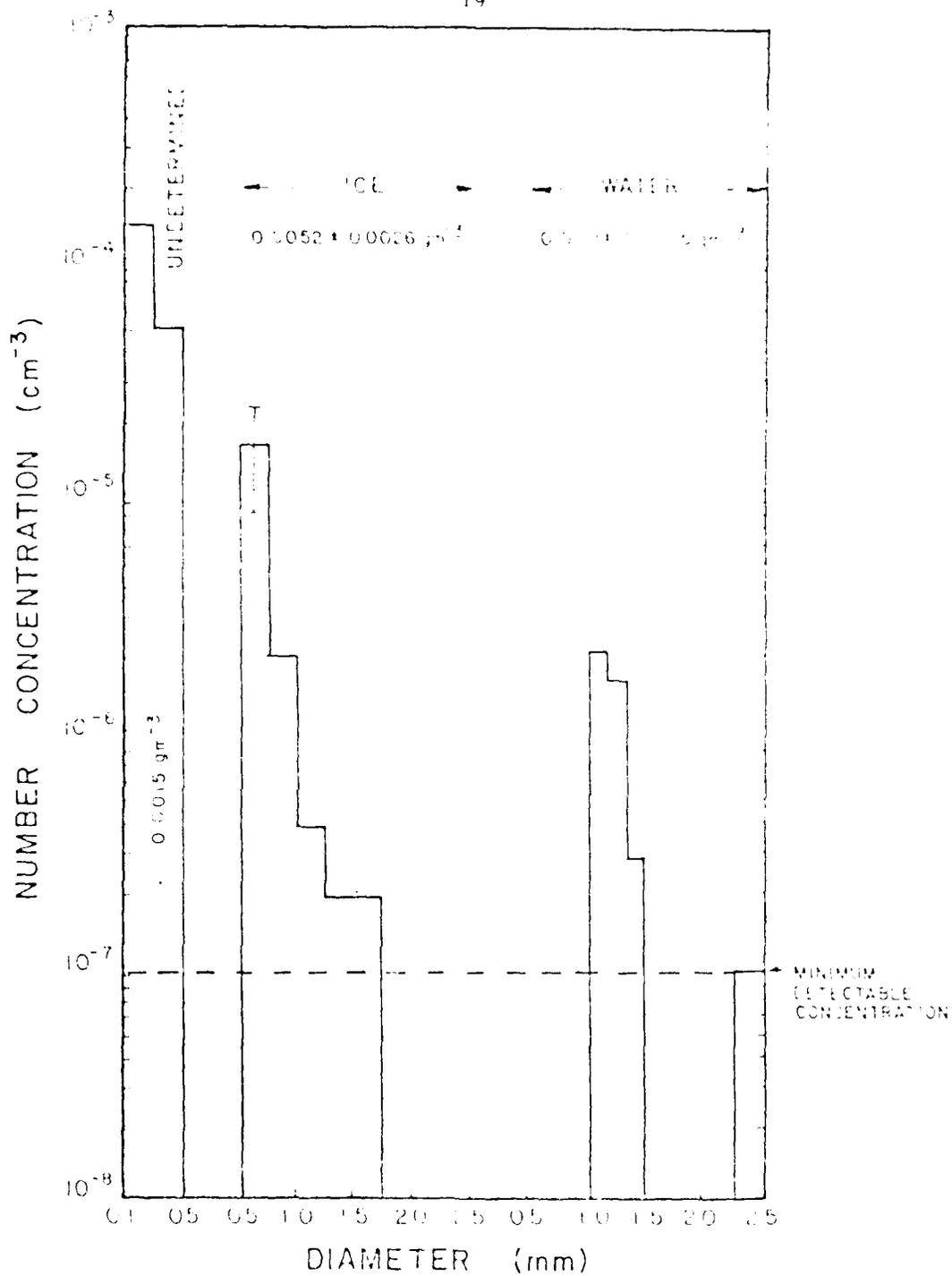
Figure 3.4b: Particle size distributions and water contents from an adjacent tower, 25 August 1975, 143752-143805 EDT.
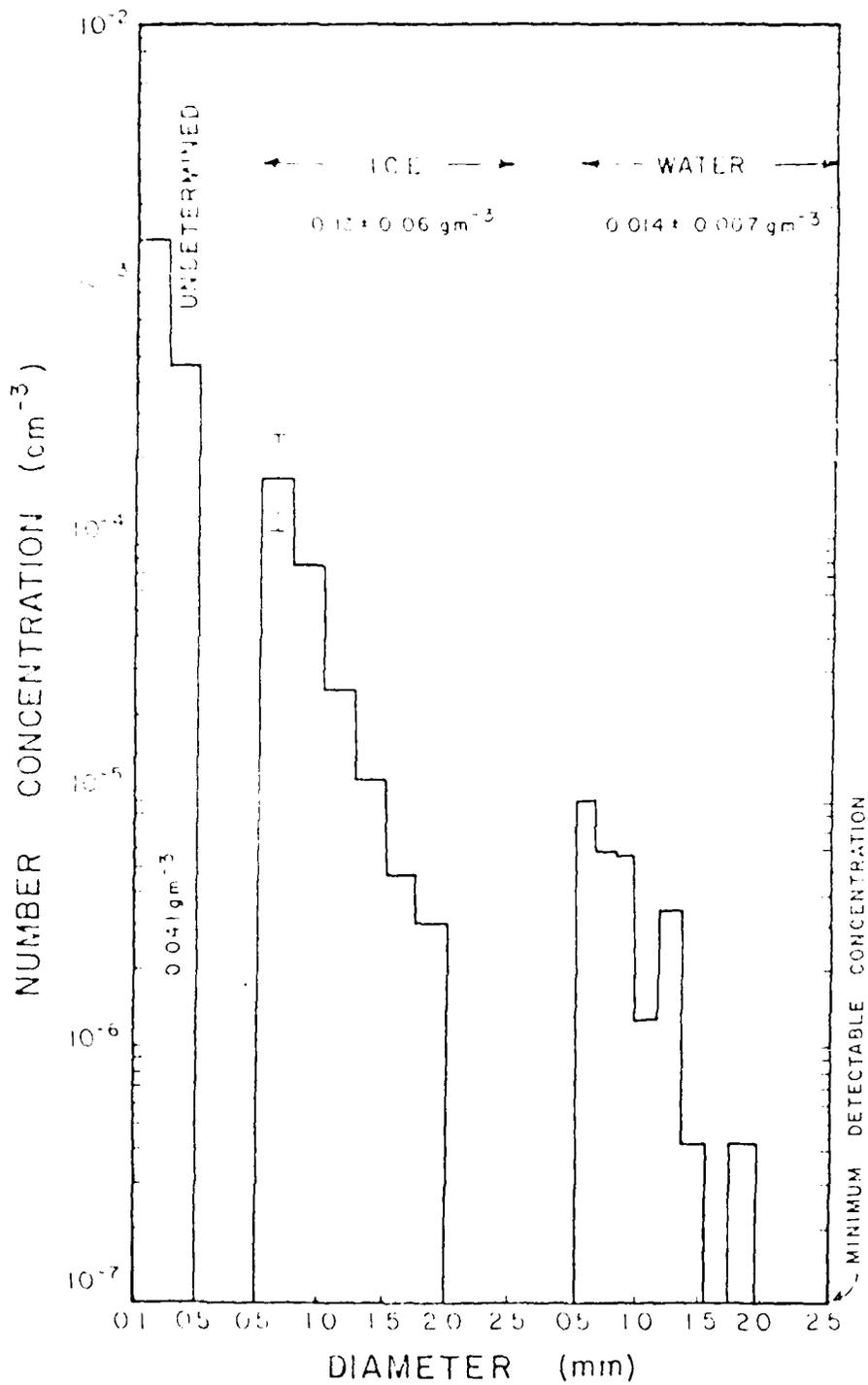
Figure 3.4c: Particle size distributions and water contents from a tower adjacent to the previous two, 25 August 1975, 144034-144041 EDT.

The reflectivities were calculated from the particle size spectra using the following expression:

$$Z = \sum_{i-1}^{n} N_i D_i^6 \qquad [mm^6 \, m^{-3}] \qquad (3.10)$$

where N_i is the number of particles in diameter interval i to $i + 1$ and D_i is the melted diameter of the particles in the interval defined by the geometric diameter $D_g = \sqrt{D_i \cdot D_{i+1}}$. Following the procedure developed in Section 3.1, Eq. (3.10) becomes

$$\tilde{Z} = |k|^2 \sum_{i=1}^{n} N_i D_i^6 \qquad (3.11)$$

where $\tilde{Z}$ is an index-of-refraction weighted reflectivity. We assume $|k|^2$ is 0.93 for liquid particles and 0.19 for ice particles. Finally, the total reflectivity value Z_t is defined as

$$\tilde{Z}_t = \tilde{Z}_r + \tilde{Z}_g + \tilde{Z}_i \qquad (3.12)$$

The reflectivities ($\tilde{Z}_r$, $\tilde{Z}_g$, $\tilde{Z}_i$, and $\tilde{Z}_t$) calculated from the particle spectra are given in Table 3.1 in terms of dBZ (10 log Z = dBZ).

Three features are apparent in Table 3.1 between the radar-measured reflectivities and the reflectivities calculated from the particle spectra. First, the measured and calculated total reflectivities track: 25 – 30 vs. 14.6 dBZ (Cell A), 18 – 23 vs. 7.3 dBZ (Cell B) and 25 vs. 20.5 dBZ (Cell C). Second, the measured values are consistently greater than the calculated values. Third, the graupel water usually contributes the greatest to the $\tilde{Z}_t$ values.

The model reflectivities were obtained from the three-dimensional

TABLE 3.1

Measured and Predicted
Reflectivity Values (dBZ)
25 August 1975

MEASURED

Scan Time (EDT)	Cell A	Cell B	Cell C
1434	25	18	--
1436	30	15 (1st penetration)	--
		23 (2nd penetration)	--
1439	--	24	--
1441	--	--	25

CALCULATED (from particle measurements)

Pass Time (EDT)	Rain Water (Z_r)	Graupel Water (Z_g)	Crystal Ice (Z_i)	Total (Z_t)
143438-143507 (Cell A)	7.7	13.7	0	15.6
143752-143803 (Cell B)	5.0	1.8	0	7.3
144036-144041 (Cell C)	17.9	18.6	0	20.5

PREDICTED (from the 3-D cloud simulation)

Time From Convection Initiation (Sec)	Rain Water (Z_r)	Graupel Water (Z_g)	Crystal Ice (Z_i)	Total (Z_t)
2400	17	0	0	17
2600	22	<10	0	22
2800	14	15	0	19
3000	15	15	0	18
3200	22	<10	0	22
3400	23	0	0	23

numerical simulations of Levy (1982) following the area-averaging
procedure used with the measured PPI reflectivities. The results of the
three-dimensional simulations were in the form of PPI reflectivity plots
at the $-10^{\circ}C$ level (6.3 km, aircraft penetration level) as a function of
time after initiation of convection. The $\tilde{Z}_r$, $\tilde{Z}_g$, $\tilde{Z}_i$ and $\tilde{Z}_t$ values
derived from the plots are listed in Table 3.1 in terms of dBZ.

Two features are apparent in Table 3.1 between the radar-measured
reflectivities and the reflectivities calculated with the model. First,
the measured values range between 15 and 30 dBZ and the calculated
values range between 17 and 23 dBZ. This result demonstrates a
remarkable agreement between the measurements and predictions. Second,
the model-predicted $\tilde{Z}_r$ values contribute more to $\tilde{Z}_t$ than the $\tilde{Z}_g$ values.
In contrast, the $\tilde{Z}_g$ values calculated from the particle spectra
contributed more to $\tilde{Z}_t$ than the $\tilde{Z}_r$ values. It is not possible from
these conflicting results to determine which type of precipitation
contributes the most to the reflectivity values. Nevertheless, it is
clear that $\tilde{Z}_r$ and $\tilde{Z}_g$ values are significant contributors. Additional
data sets are required to determine the major contribution. This was
accomplished in Section 3.4 using NHRE data.

Vertical cross-sections of the measured radar reflectivity were
also compared to model-predicted radar cross-sections. Measured
reflectivities shown in Fig. 3.5a-d are contoured in intervals of 10 dBZ
up to 40 dBZ and at 5 dBZ intervals thereafter. The model-predicted
reflectivities in Fig. 3.5e and 3.5f are contoured at uniform 10 dBZ
intervals. In general the model-predicted reflectivities are the same
as observed and the general cell evolution is similar. The upper level
maximum of $\tilde{Z}$ predicted by the model corresponds to the early stages of
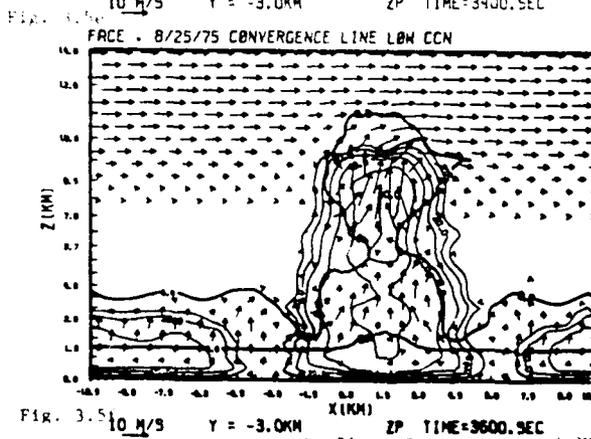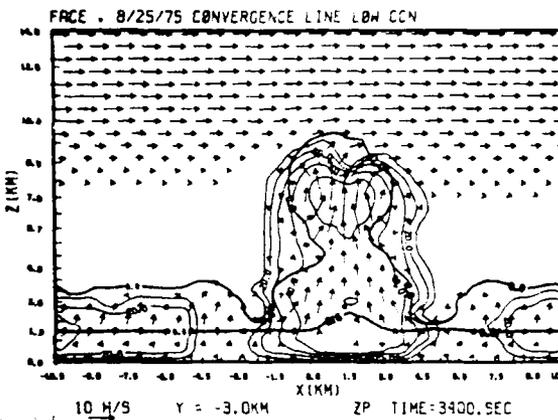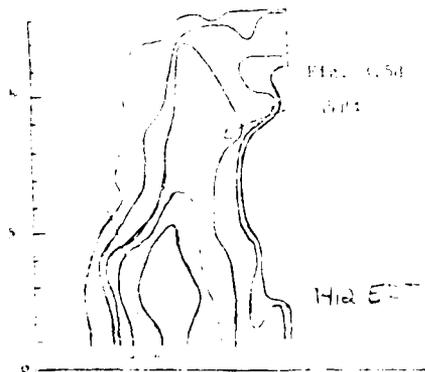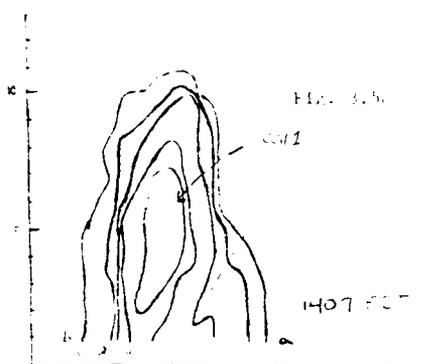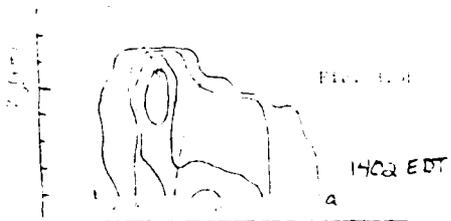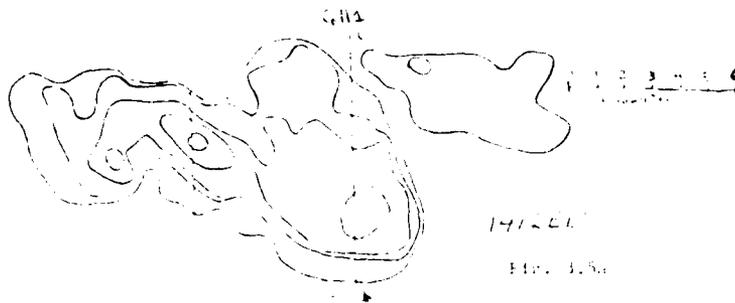
Figure 3.5: Measured reflectivities (a-d) and corresponding model predicted reflectivities (e-f).

graupel formation. Such a maximum was not measured, however.

In summary, the measured PPI reflectivity values were consistently greater than the reflectivities calculated from the particle spectra. In contrast, the measured reflectivities (PPI and RHI) were remarkably consistent with the reflectivities resulting from the three-dimensional simulation. The $\widetilde{Z}_r$ and $\widetilde{Z}_g$ values contributed to the $\widetilde{Z}_t$ values. It was not possible to determine the dominant precipitation type because the $\widetilde{Z}_r$ and $\widetilde{Z}_g$ values resulting from the particle measurements and three-dimensional simulations were not consistent.

There are two possible explanations for these discrepancies between the measured and calculated reflectivities. First, the radar-derived reflectivities may be overestimated because the reflectivities are presumably caused by liquid particles. We have shown that graupel particles contribute significantly to the reflectivities. Second, the measure of rain water and graupel water contents may have been underestimated due to limited sample volumes leading to the underestimated Z values from the particle spectra. Nevertheless, differences between the calculations, predictions and the measurement were on the order of the uncertainties of the measurements. Consequently, the model-predicted reflectivities are suitable for investigating the causes for the variability in water content-radar reflectivity relationships.

3.4 Investigations of Variations in Water Content (M) - Radar Reflectivity (Z) Relationships

3.4.1 Model investigations

The model investigation of M-Z variations first focused on investigating 'simulated' aircraft penetrations. The results from the 3-D model calculations of the Florida cumulus were used to construct three

'simulated' aircraft penetrations at the 6.3 km (-10 C) level (see Fig. 3.6). It can be seen in Figure 3.6 that the simulations consisted of rain and graupel water contents (ρ_r and ρ_g), radar reflectivities (10logZ'), and the ratio of 10logZ' and ($\rho_r + \rho_g$) as functions of distance in the cloud [Z' is the index of refraction-weighted reflectivity, equal to Z x 0.93 for liquid and Z X 0.19 for ice]. The latter ratio was calculated to evaluate any region where the total reflectivity behaved anomalously with respect to the total mass. The significant result from these simulations are the regions of high reflectivities and low water contents near the edge of the cloud caused by a relatively few large particles. The water contents in these regions are less than 10% of the maximum water contents in the cloud. Consequently, the anomalous regions contribute little to the total water content of the cloud. But, at low water contents, a sufficiently large number of large particles are produced through the $\rho_g \propto N(D)$ parameterization to affect the reflectivity ($\propto D^6$) but not the water content ($\propto D^3$). Further, in the high reflectivity regions in the center of the cloud, the ratios are constant with distance in the cloud. These results were investigated further in the next section to determine their realism based on comparison with measurements in cumulvs clouds. It wll be shown that the model predicted "anamalous M vs. Z" regions are physically real.

3.4.2 NHRE case study: $M \propto Z^{0.2}$

The case selected for investigation was a hailstorm in northeast Colorado that was well observed and measured during the 1976 field program of the National Hail Research Experiment (NHRE). The case was chosen primarily because of the availability of detailed hydrometeor habit and size data. The analysis to be described required a data set
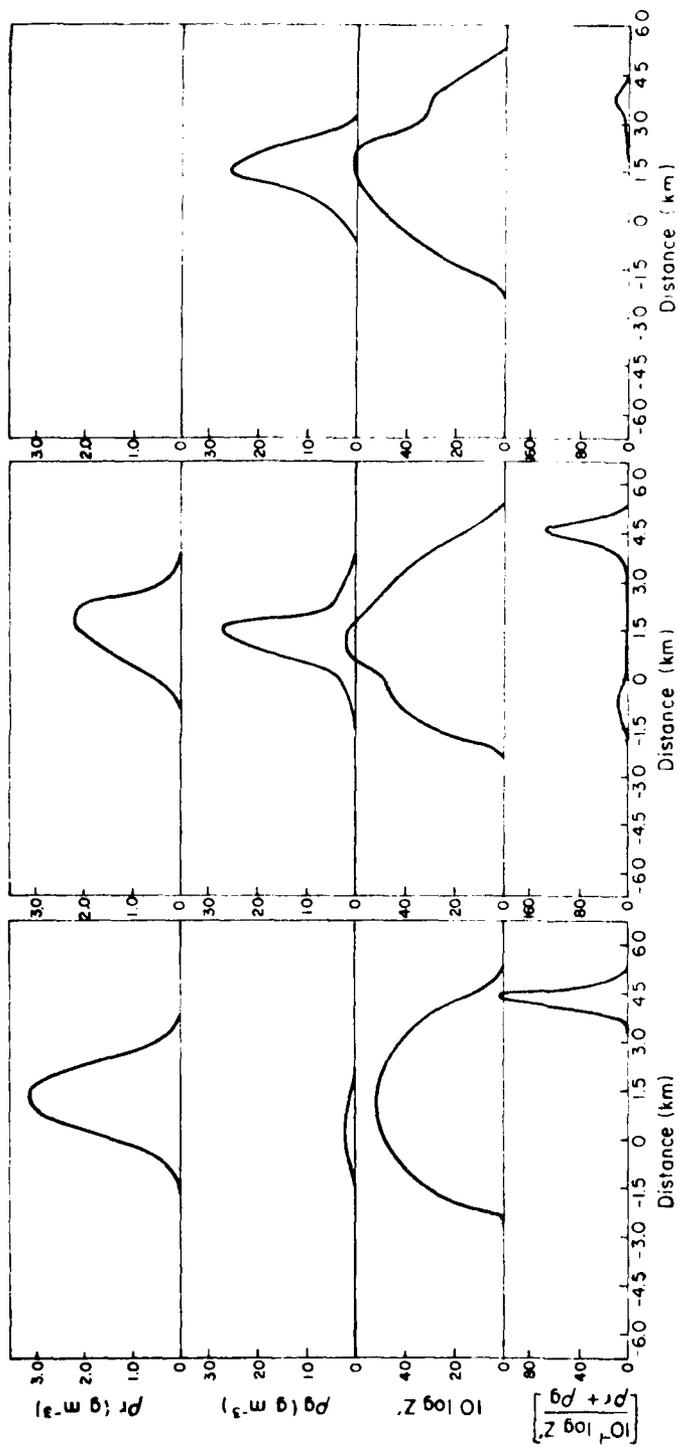
Figure 3.6: Results of 3-D model simulations for a Florida cumulus at 3300s (left), 3400s (middle), and 3600s (right) after initiation of the cloud. The data were from the 6.3 km (-10°C) level in the simulated cloud. Parameters are: ρ_r (rain content), ρ_g (graupel content), and 10logZ' (index of rafraction-weighted reflectivity).

of simultaneous water contents and reflectivities along a flight track. Ideally, surface-based radar reflectivities should have been used to match with simultaneous aircraft measurements. However, the available radar data for the NHRE case were insufficient in spatial and temporal resolution to allow meaningful comparisons. The reflectivities were, therefore, derived from the same airborne hydrometeor size and concentration measurements used to derive the hydrometeor masses. Thus, the identical resolution between the M and Z values was achieved.

The selected hailstorm occurred on 25 July 1976 and is described by Sanborn (1979). The aircraft data were collected by the South Dakota School of Mines and Technology armored T-28 aircraft during three penetrations of the storm complex. Figure 3.7a-c, reproduced from an analysis of the storm by Hunter (1980), illustrate the flight tracks through the storm complex. The tracks are superimposed on representative radar reflectivity PPI displays. The flight level averaged about 6.5 km MSL, with the temperature between -10 and -15 C. The three penetrations sampled a wide variety of conditions.

Hydrometeor data were collected with two particle measuring sensors on board the T-28 aircraft: a Particle Measuring Systems (PMS) 2-D cloud probe and a hail spectrometer. These instruments and the methods employed to reduce the data at NCAR are described by Heymsfield and Parrish (1979). Table 3.2 gives the size ranges of the spectral channels into which the measured particles were grouped. Each particle's habit was classified into one of the six categories listed in Table 3.3. For particle sizes between 400 and 10,000 μm, the habit was determined objectively from the 2-D images and microphysical measurements, as outlined by Heymsfield and Parrish (1979). Smaller particles were assumed
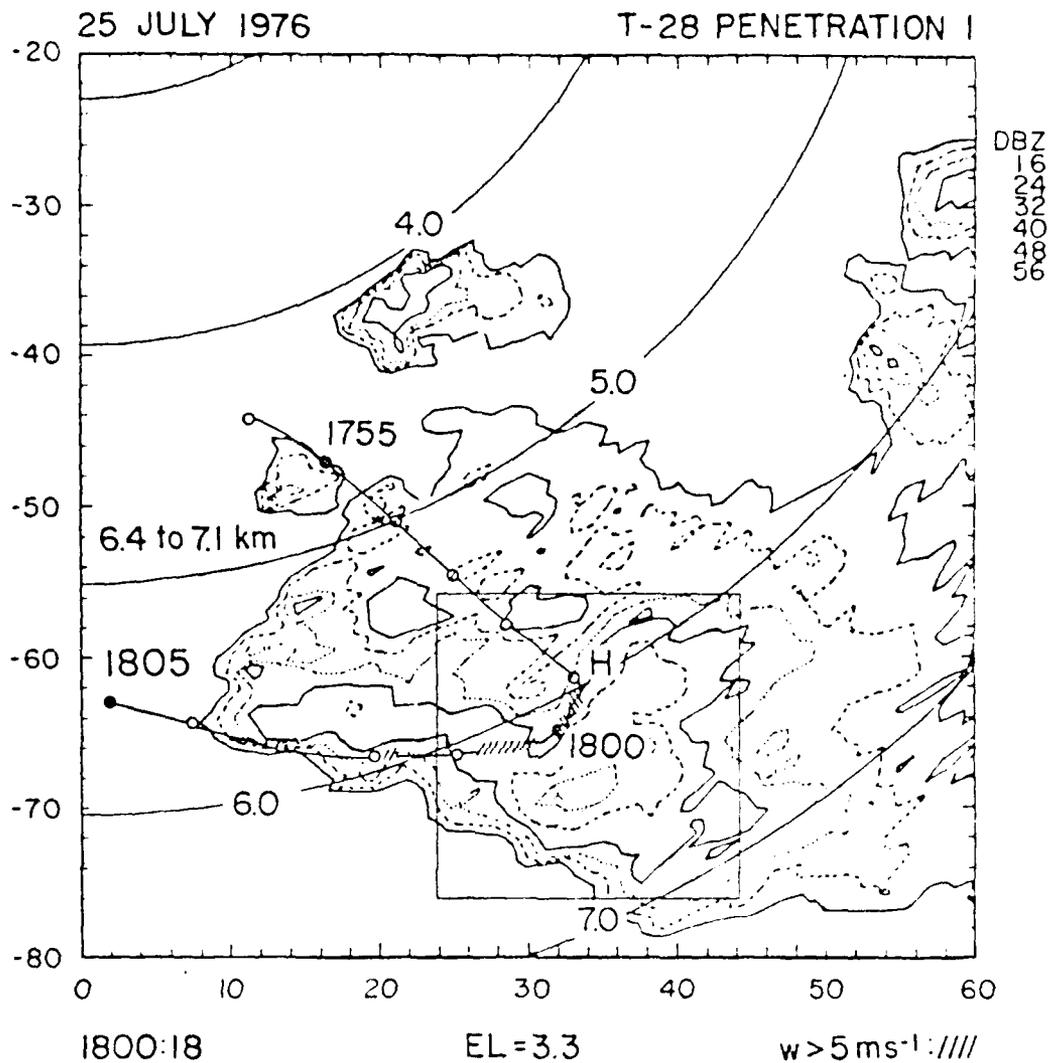
Figure 3.7a: Radar reflectivity at 1800:18 MDT and 3.3° elevation angle showing corrected T-28 track for penetration 1 from 1754 to 1805 MDT. The track is cross-hatched where > 5 m s^{-1} updrafts were encountered, and positions are marked every minute and labelled every five minutes. The altitude range of the penetration is given at the left side of the figure. A 'H' denotes a location where hail was collected at the surface. Reflectivity contours are given by the legend at the upper right and arcs of constant elevation are labelled in kilometers (from Hunter, 1980).
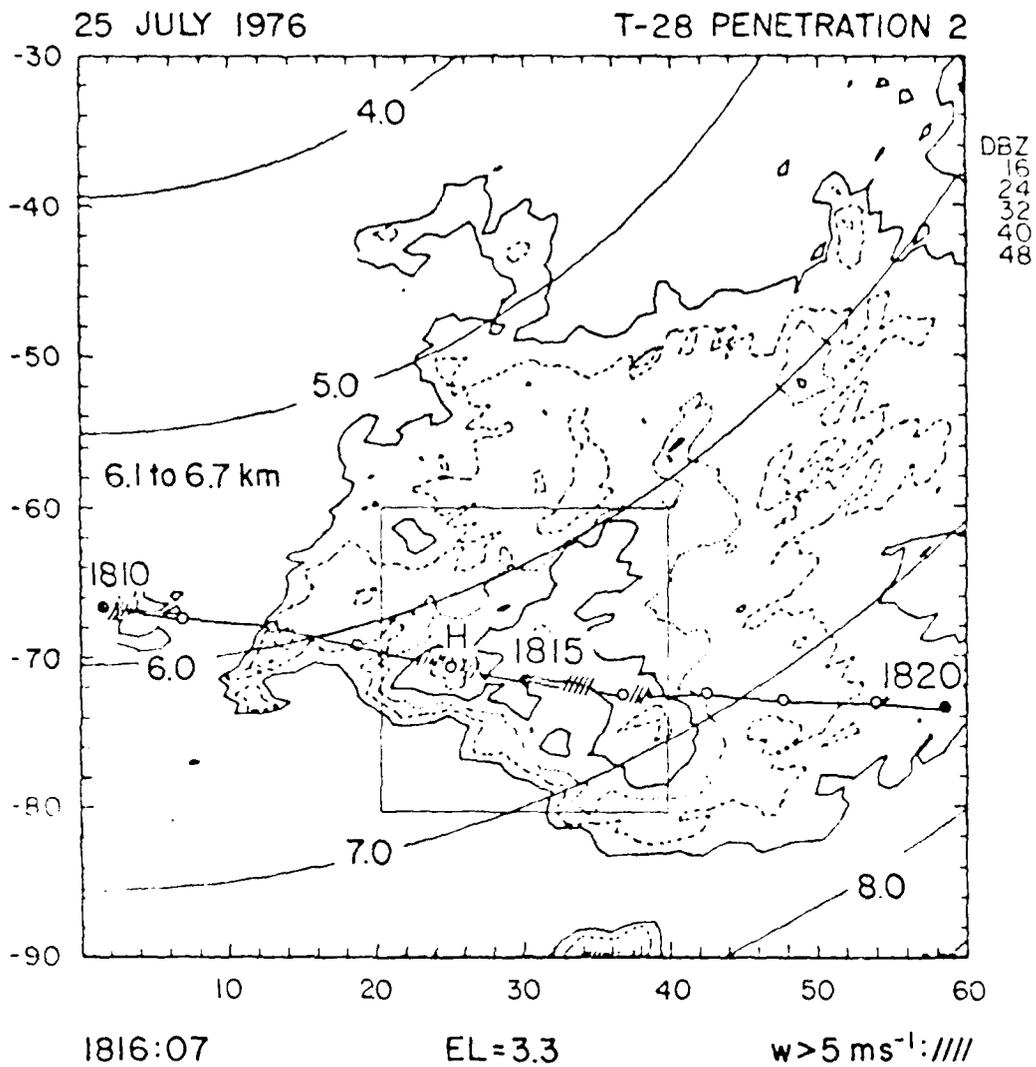
Figure 3.7b: Same as Fig. 3.7a except PPI is at 1816:07 MDT and track is for penetration 2 from 1810 to 1820 MDT (from Hunter, 1980).
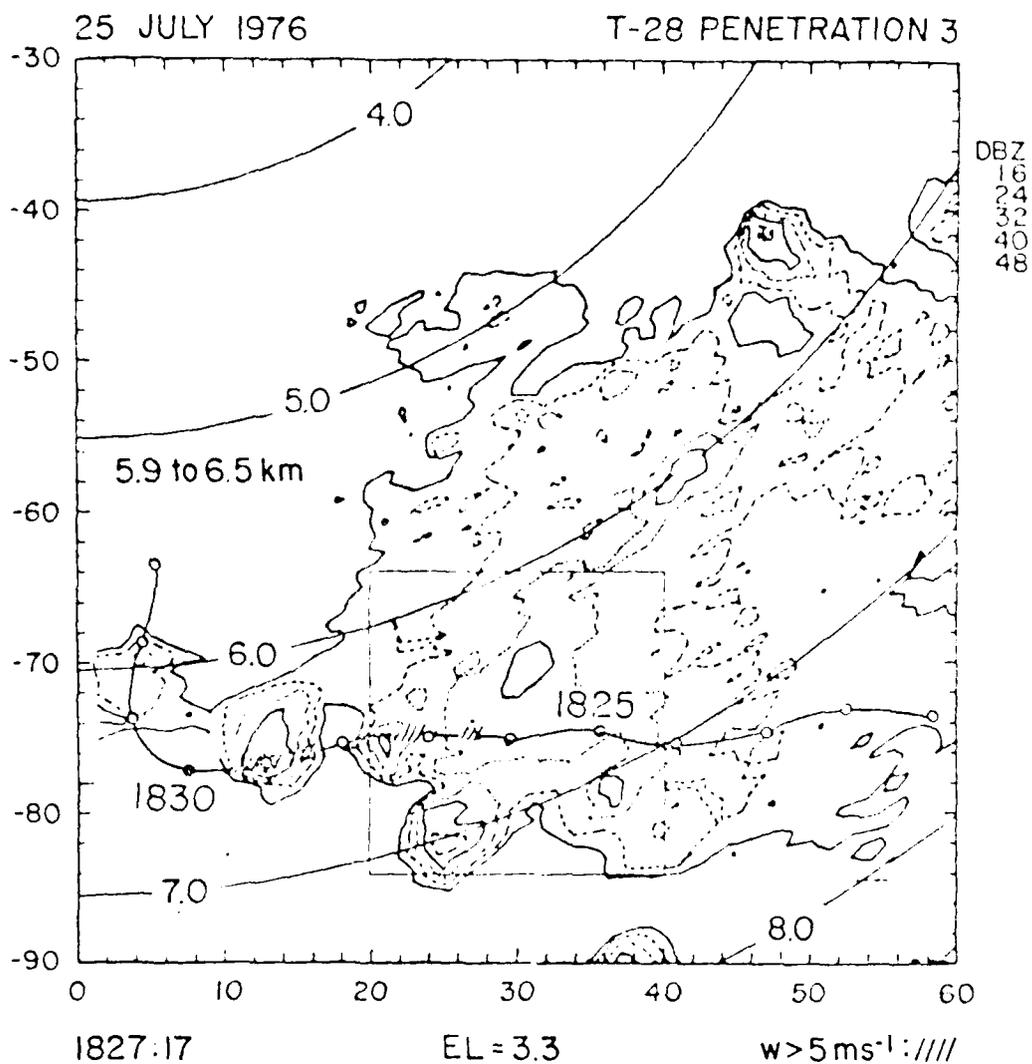
Figure 3.7c: Same as Fig. 3.7a except PPI is at 1827:17 MDT and track
               is for penetration 3 from 1820 to 1833 MDT (from Hunter,
               1980).

TABLE 3.2

Spectral Size Intervals and Assumed Particle Dimensions from
the Concatenation of PMS 2-D Cloud Probe and Hail Spectrometer Data

2-D Cloud Probe

Channel	Size Range (μm)	Assumed Particle Dimension (μm)
1	25-50	37.5
2	50-150	100
3	150-250	200
4	250-350	300
5	350-450	400
6	450-550	500
7	550-650	600
8	650-750	700
9	750-850	800
10	850-950	900
11	950-1000	975
12	1000-1500	1250
13	1500-2000	1750
14	2000-3000	2500
15	3000-4000	3500

Hail Spectrometer

Channel	Size Range (μm)	Assumed Particle Dimension (μm)
16*	4700-6050	5375
17*	6050-7000	6525
18*	7000-7950	7475
19*	7950-8850	8400
20*	8850-9750	9300
21*	9750-10650	10200
22	10650-11750	11200
23	11750-13350	12550
24	13350-15200	14275
25	15200-17900	16550
26	17900-22900	20400
27	22900-29800	26350
28	29800-38950	34375
29	38950-118100	73525

*Habit information available from 2-D cloud probe

to be plates and larger particles were assumed to be graupel/hail. Note in Table 3.3 that there is no category for liquid particles. Recent research with PMS 2-D data by Heymsfield (1982, personal communication) on NHRE and Oklahoma cases, and our own experience with a cumulonimbus case in Montana, have indicated that even at levels of near -10°C, supercooled drops appear in the 2-D images and should be classified as a separate particle category. However, their sizes and concentrations are sufficiently small that their contribution to total water mass and reflectivity is negligible in contrast to the

TABLE 3.3

Habits Used for Classification of Hydrometeors

ID Code Habit Symbol

1 Graupel/Hail GR

2 Rimed Dendrite RD

3 Rimed Aggregate of Dendrites RA

4 Plates PL

5 Umrimed Dendrite UD

6 Unrimed Aggregates of Dendrites UA

7 Shedded Particle (Rejected)

graupel contribution. Consequently, no category for supercooled rain appears in Table 3.3.

The processed T-28 data from NCAR consisted of particle concentrations as a function of habit and spectral channel for 10-s samples along the flight tracks in Fig. 3.7. Thus, for the flight speed of near 100 m/s, each sample was collected over a distance of about 1 km. Particle mass concentrations (M) were calculated using the following relationship,

$$M = \sum_i \sum_j N_{ij} m_{ij} \quad , \tag{3.13}$$

where i represents all channel sizes (Table 3.2), j represents all habits (Table 3.3), N_{ij} is the particle concentration, and m_{ij} is the mass of an individual particle. As described by Heymsfield and Parrish (1979), particle mass is related to its dimension L through power functions of the form $m_{ij} = aL^b$, with each habit having a unique set of empirical constants a and b. The radar reflectivity factors (Z) were calculated using the relationship from Heymsfield and Parrish

$$Z_e = \sum_i \sum_j N_{ij} m_{ij}^2 \times 3.648 \times 10^9 \times (0.19/0.93) \tag{3.14}$$

where N_{ij} is in units of 1^{-1} and m_{ij} is in units of $g \ m^{-3}$. The factor 3.648×10^9 is a unit-conversion factor relating the square of the particle's mass to the 6th power of its melted diameter. The ratio (0.19/0.93) converts the reflectivity factor for the ice particles (Z) to an 'effective reflectivity factor' (Z_e) that assumes a dielectric constant for liquid water. (Hereafter, 'reflectivity' will be used to mean 'effective reflectivity factor.')

The mass concentrations calculated from the airborne measurements using Eq. (3.13) (M_A) are plotted as a function of time in Fig. 3.8a and 8b. The total mass concentrations are plotted, along with the mass concentrations for graupel, plates, and rimed dendrites. The mass concentrations and sample-to-sample variability of rimed aggregates, unrimed dendrites and unrimed aggregates were similar to the values for the rimed dendrite plot; these additional habits are omitted from the figures for clarity. It can be seen in Figures 3.8a and 3.8b, that the
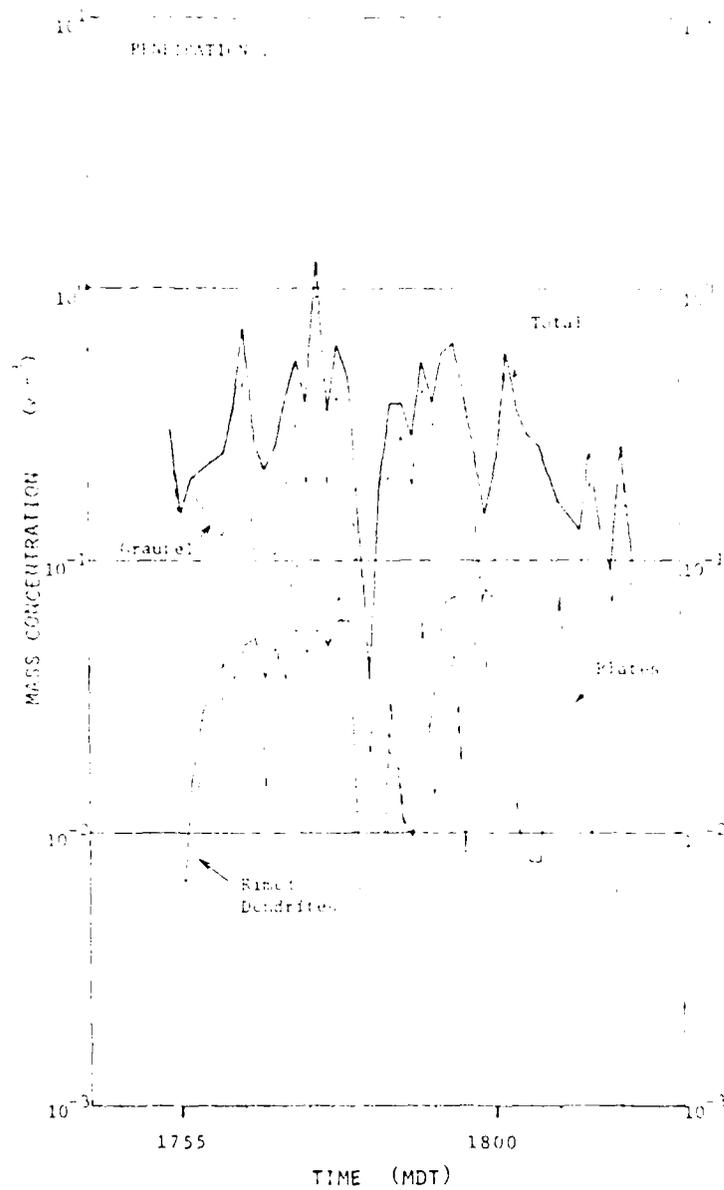
Figure 3.8a: Mass concentrations of particles from airborne
measurements on 25 July 1976, Penetration 1. Included are
plots for total mass concentration and contributions due
to graupel, plates, and rimed dendrites.
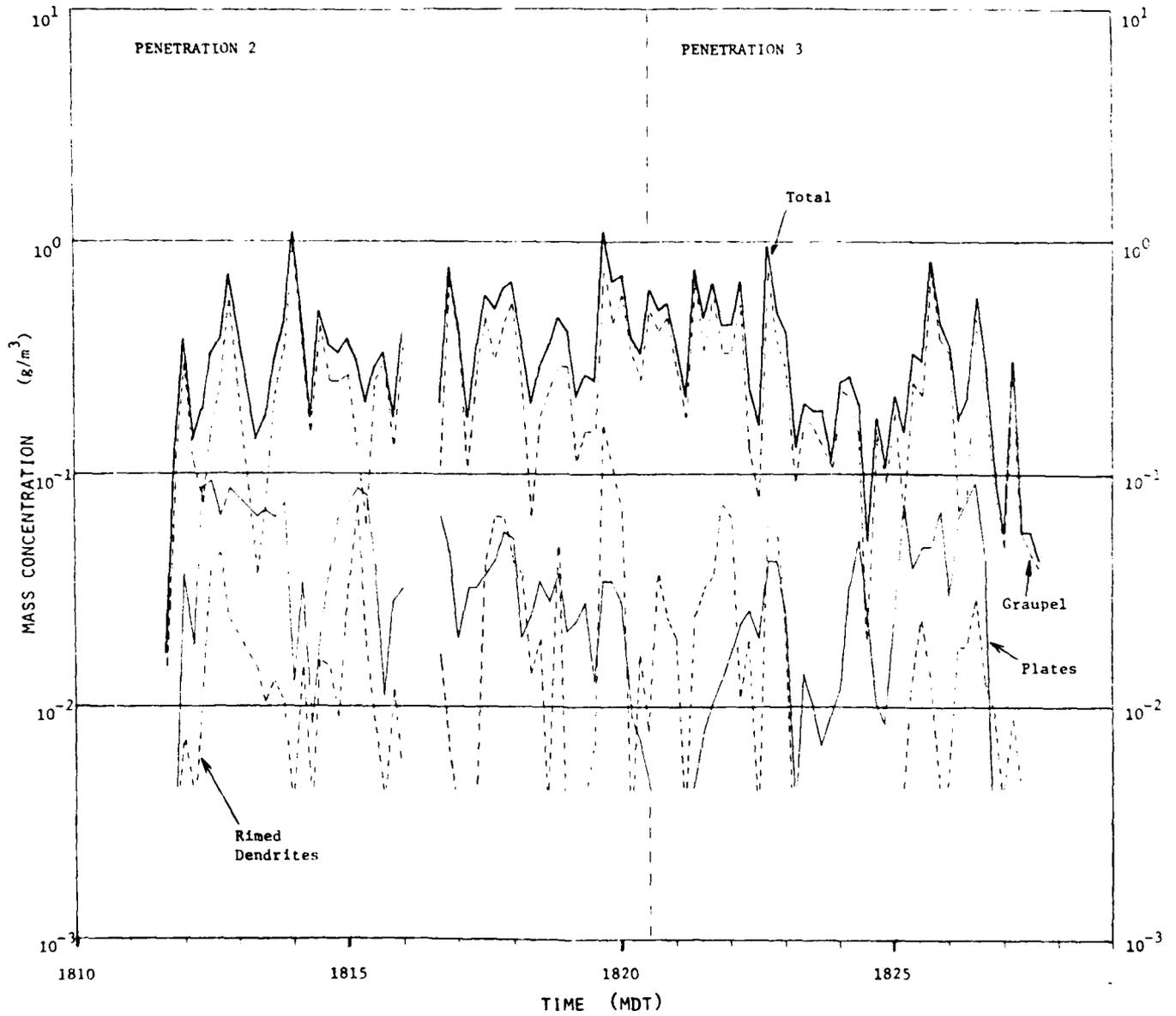
Figure 3.8b: Same as Fig. 3.8a except for Penetrations 2 and 3.

variation of M_A along the flight track is large, with successive 10-s samples frequently differing by a factor of 5, and that graupel particles contribute most to the total M_A.

The reflectivities calculated from the particle measurements (Z_{Ae}) using (3.14) are plotted as dBZ versus time in Fig. 3.9a and 3.9b. Considerable variability is evident in the reflectivity values in the figures. Hail occurrence near 1800 and 1815 MDT caused the highest reflectivities. The contribution of graupel to total reflectivities is so large that the graupel reflectivity values are not plotted, since they nearly coincide with the total reflectivity curve. The contribution due to the other particle habits are very small, typified by the curve included for rimed dendrites. The contribution of plates to the total M_A is comparable to all habits except the dominant graupel category (Fig. 3.8). However, the effect of plates on reflectivities is negligible, implying large concentrations of small particles. The average particle spectra (from penetrations 1, 2 and 3) for each habit, gr phed in Fig. 3.10, confirm the large number of small plates. Fig. 3.10 also illustrates the dominance of graupel at larger sizes.

In order to study the factors which cause variability in M-Z relationships, a least-square, best-fit power function of the form

$$M_A = aZ_{Ae}^b \qquad (3.15)$$

was derived, where Z_{Ae} is the effective-reflectivity (mm^6/m^3) determined from the airborne particle measurements using ‵‵. ‵4). M_A is the mass concentration (g/m^3) derived from (3.13) and a and b are constants of the functon. Included in the sample were all pairs of M_A and Z_{Ae} for which 10 dBZ_e < ($10logZ_{Ae}$) < 65 dBZ_e, or 160 samples. These pairs are
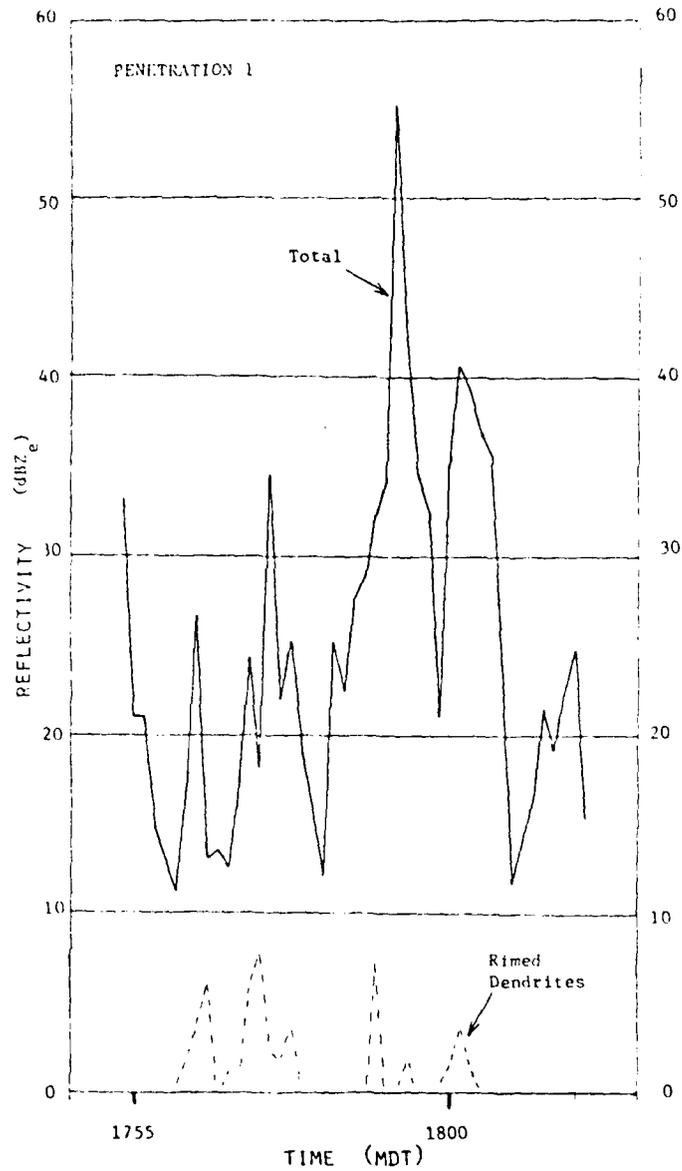
Figure 3.9a: Radar effective-reflectivity factors calculated from the airborne particle measurements from 25 July 1976, Penetration 1. Included are plots for total reflectivity and contributions due to rimed dendrites. The plot for graupel is omitted, since it nearly coincides with the total plot.
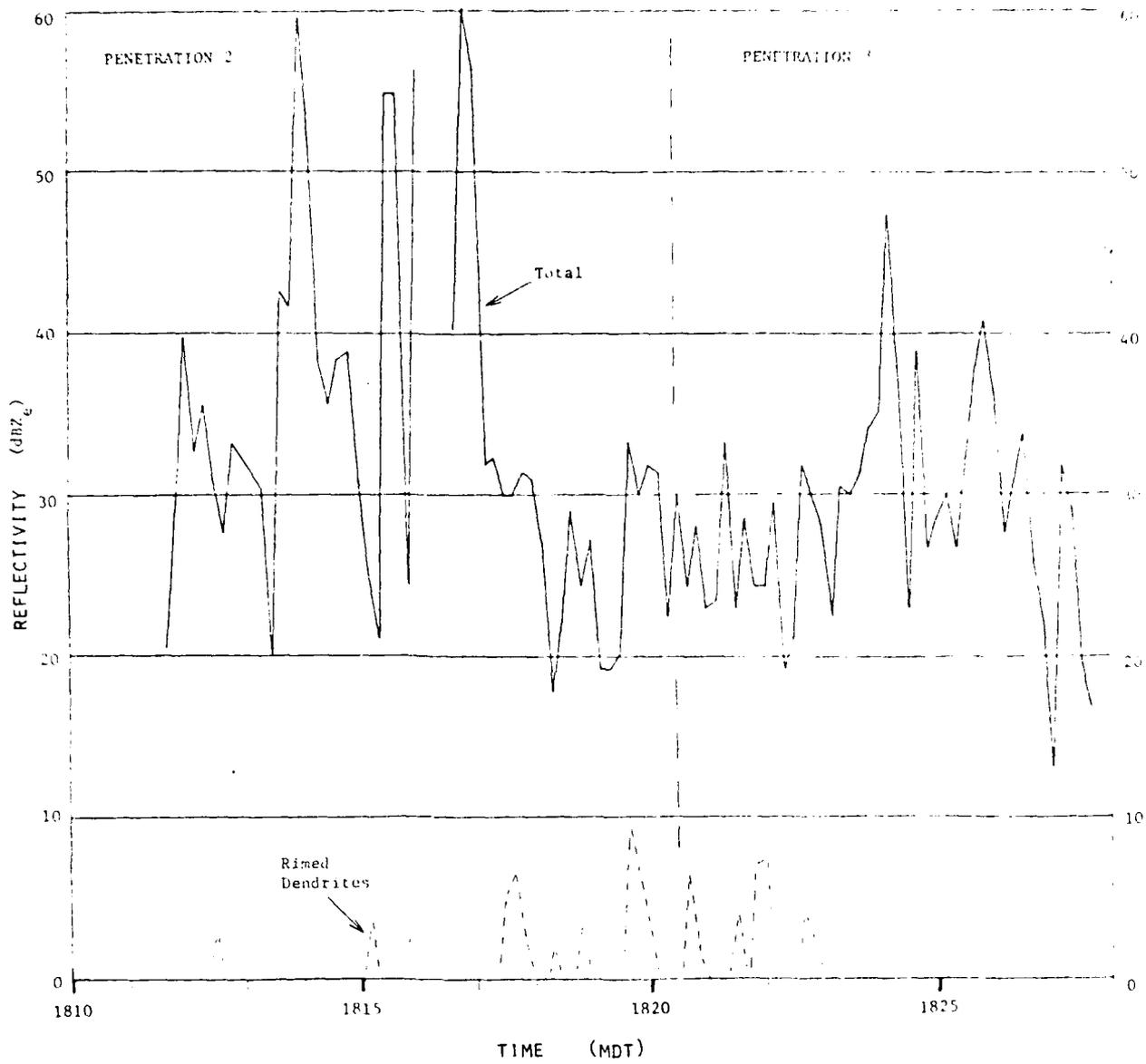
Figure 3.9b: Same as Fig. 3.9a except for Penetrations 2 and 3.
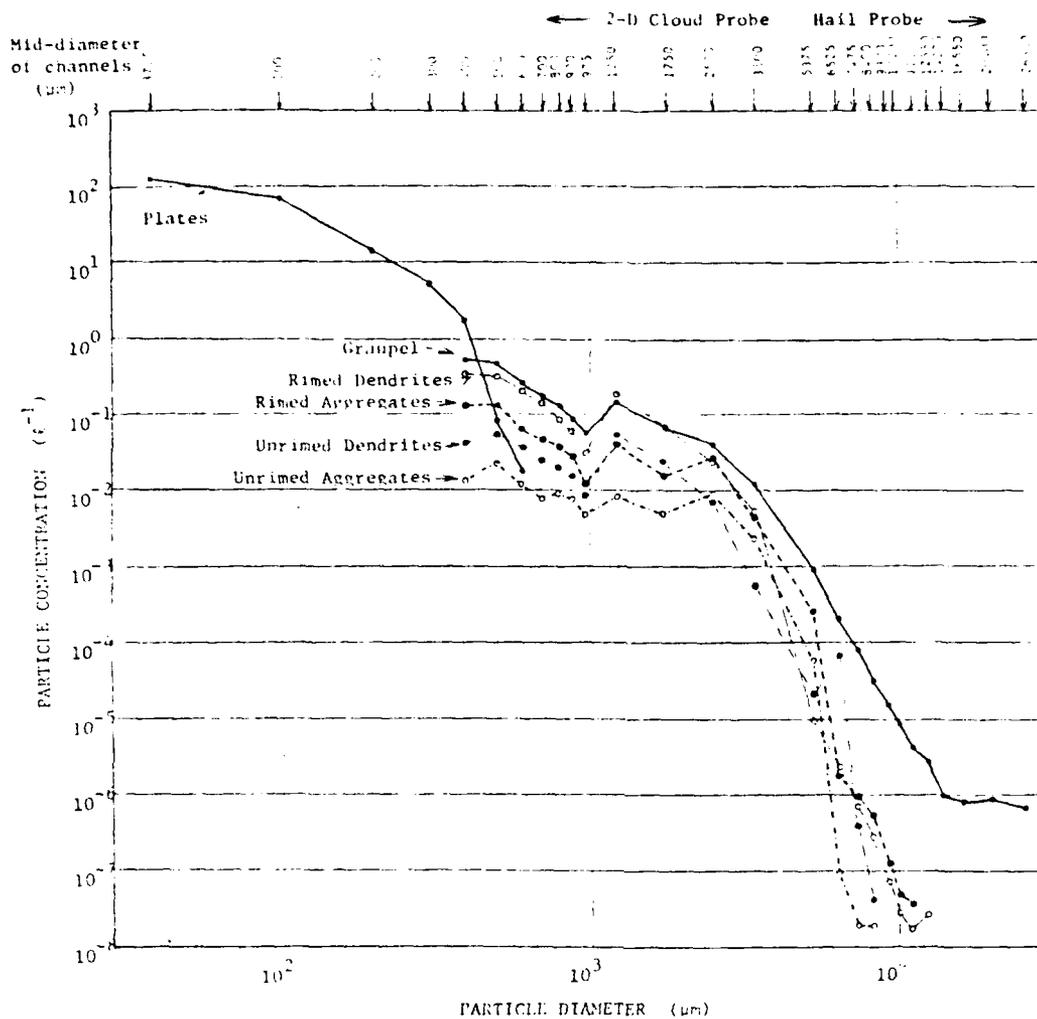
Figure 3.10: Average particle spectra for the six identified habits from Penetrations 1, 2, and 3 on 25 July 1976. Included in the spectra are the 160 samples for which $10 \leq 10\log Z_e \leq 65$ dBZe. The contribution due to particles grouped into each spectral channel is plotted at the mid-point of that channels' spectral range, noted at the top (see also Table 3.2).

plotted in Fig. 3.11 as a scatter-gram of $\log M$ vs. $\log Z_e$. Solving for the best-fit line to these data, a and b in (3.15) become 0.065 and 0.196, respectively, yielding a correlation coefficent of 0.50 and a standard error factor of 0.349. This best-fit line is plotted in Fig. 3.11.

Now, (3.15) becomes

$$M_D = 0.065 \ Z_{Ae}^{0.196} \qquad\qquad (3.16)$$

where M_D is a derived mass concentration that lies along the solid line in Fig. 3.11. Values of M_D were calculated using this expression for each Z_{Ae} value in Fig. 3.9 and plotted, along with the corresponding M_A value, versus time in Figs. 3.12a and 3.12b.

Coherent periods of generally under-estimated M_D values ($M_D < M_A$) occur in Figures 3.12a and 3.12b between 1755 and 1800 MDT and between 1817 and 1823 MDT. Slightly less coherent periods of over-estimated values ($M_D > M_A$) occur between 1812 and 1817 MDT and after 1823 MDT. The coherent patterns of over-estimated and under-estimated M values suggest that the variations are real and not instrument noise. The 160 (M_A, Z_{Ae}) pairs were then divided into two groups, $M_D > M_A$ (below the best-fit M_D line in Fig. 3.11) and $M_D < M_A$ (above the line in Fig. 3.11), in order to determine the cause(s) for the two groups.

The average M_A and Z_{Ae} values for each group were computed for each particle habit and for all habits combined. The results are graphed in Fig. 3.13. Values of $\overline{M}_A$ and $\overline{Z}_{Ae}$ for all habits combined are plotted in the center column of the left and right panels in Figure 3.12. The values of $\overline{M}_A$ and $\overline{Z}_{Ae}$ for the over-estimated ($M_D > M_A$) and under-estimated ($M_D < M_A$) groups are plotted to the left and right,
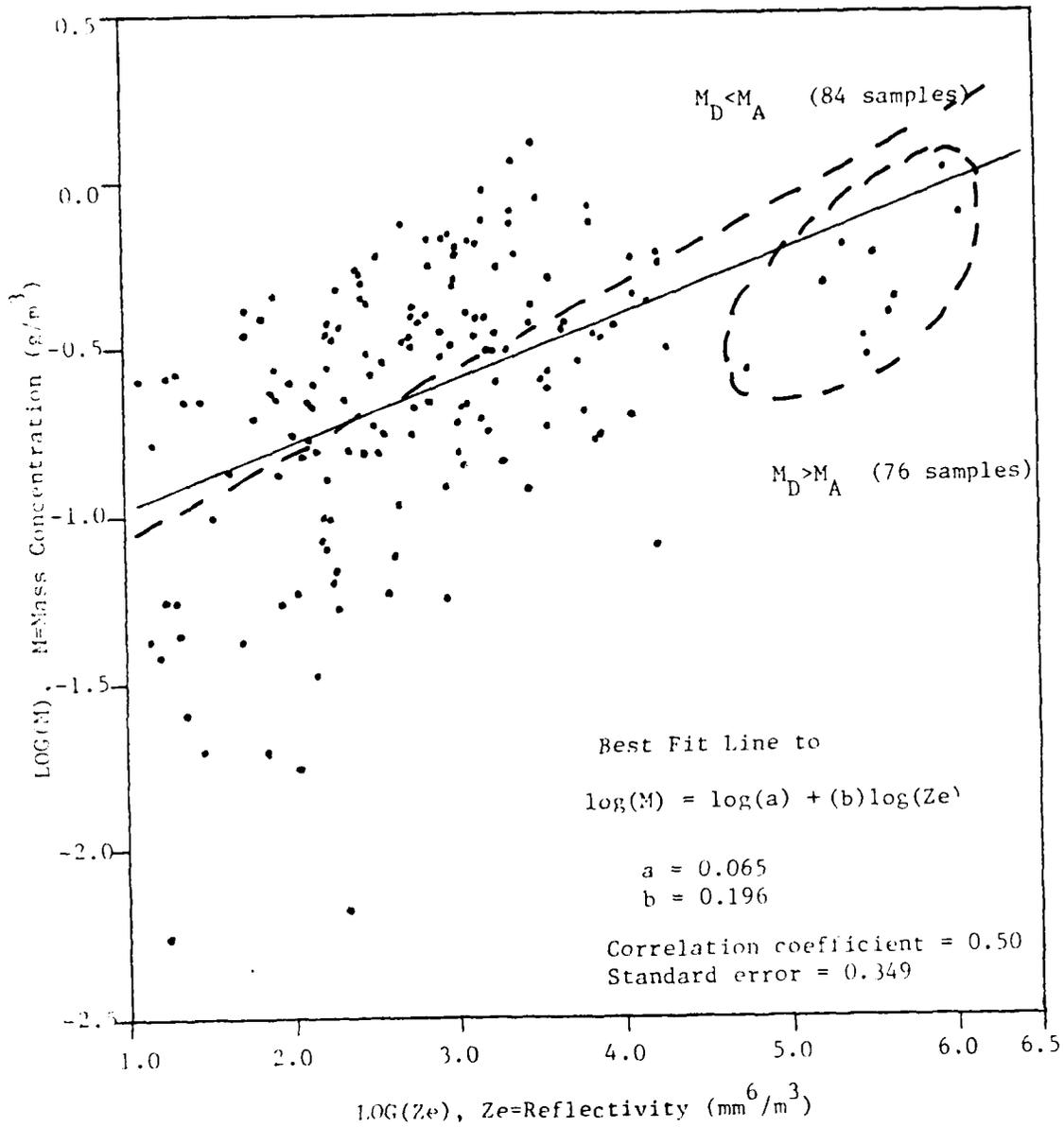
Figure 3.11: Scatter-gram of pairs of (M_A, Z_{Ae}), calculated from airborne particle measurements. The best-fit least-squares line for the log-log plot of these data is shown (solid line), with constants a and b for the power function $M = aZe^b$ of 0.065 and 0.196, respectively. The line gives the derived value of $M_D = f(Z_{Ae})$, separating the data into two sets, $M_D > M_A$ (76 points below the line) and $M_D < M_A$ (84 points above the line). The dashed line is the best-fit to the points with the highest ten Z_e values (dashed perimenter) removed.
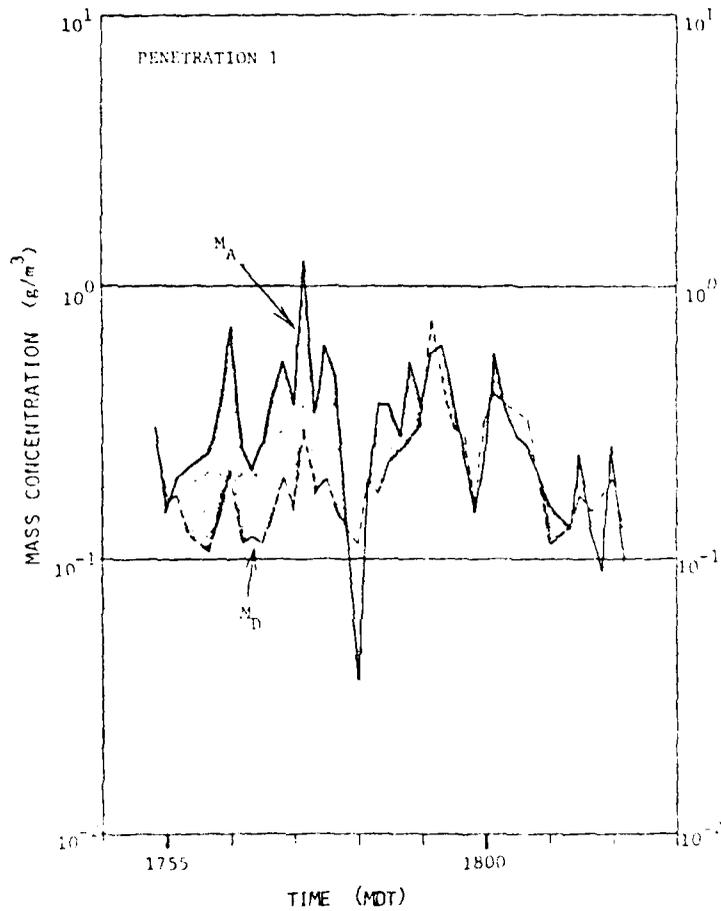
Figure 3.12a: Values of mass concentrations calculated from particle spectra (M_A), and calculated from M_D vs. Z_{Ze} relationship (M_D), plotted versus time for Penetration 1. Darkly shaded regions between the plots show portions of the flight track where $M_D < M_A$, and lightly shaded regions are where $M_D > M_A$.
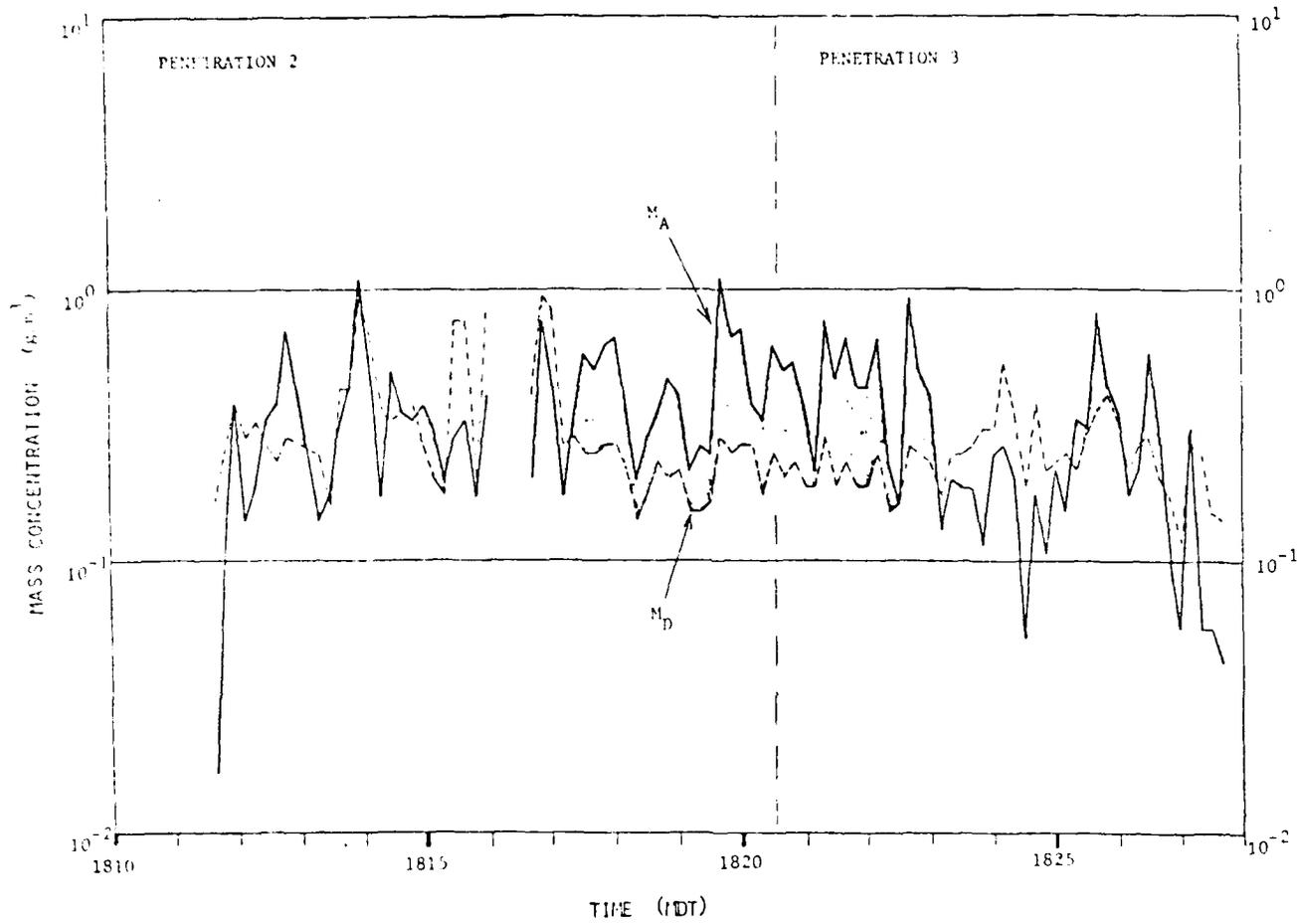
Figure 3.12b: Same as Fig. 3.12a, except for Penetrations 2 and 3.
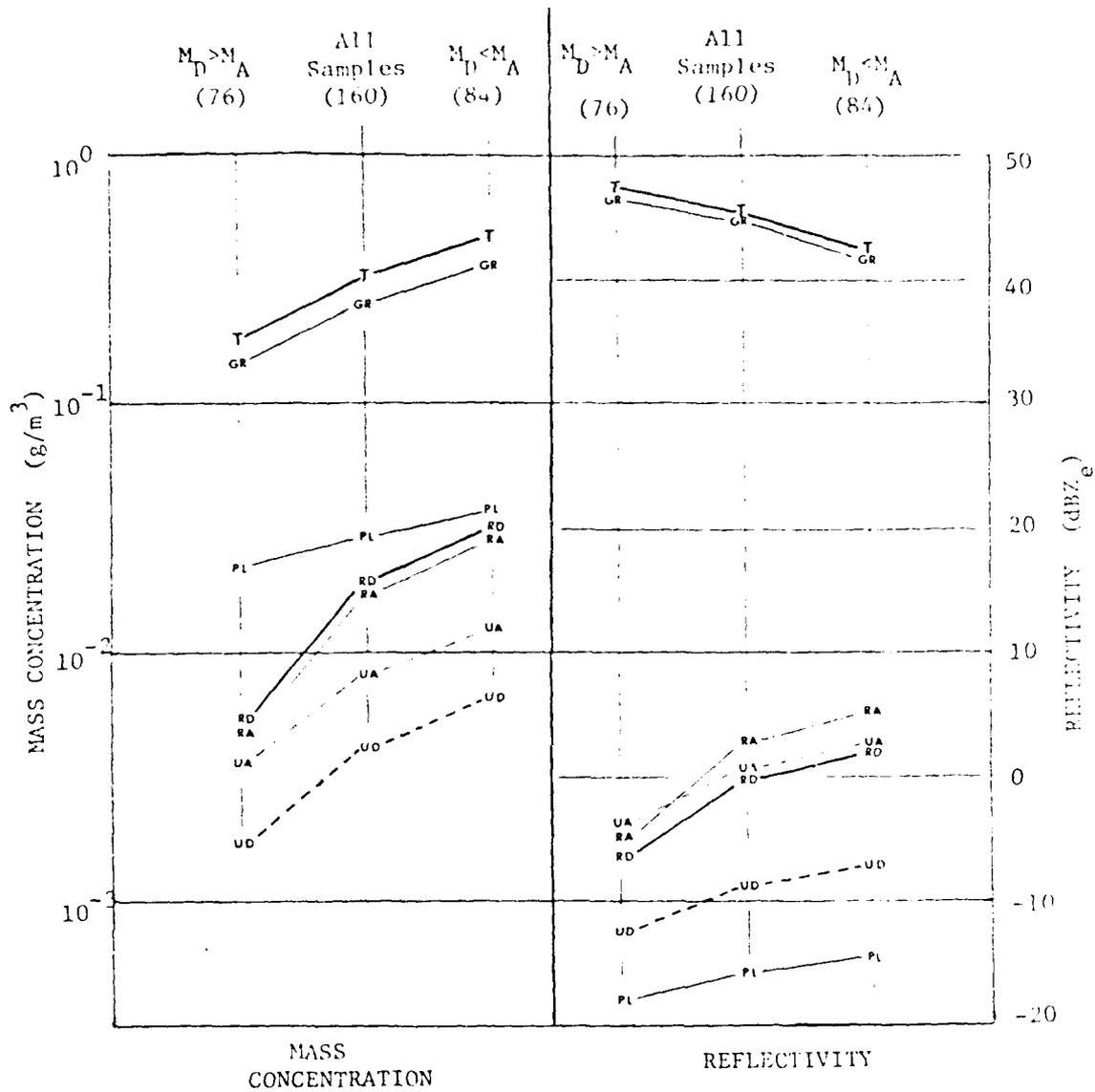
Figure 3.13: Values of $\overline{M_A}$ (left panel) and $\overline{Z_{Ae}}$ (right panel) for the total set of 160 samples (center columns of each panel), for the 76 samples where $M_D > M_A$ (left columns), and for the 84 samples where $M_D < M_A$ (right columns). Plotted are values for each habit specified in Fig. 3.10 and for all habits combined ('T').

respectively, of the center columns in Figure 3.13. It can be seen in Figure 3.13, amplifying the results indicated in Figs. 3.8 and 3.9, that graupel (GR) contributes most to total M_A and Z_{Ae} values (T). The contributions by the other five habits are much less, 1 to 2 orders less for M_A and 4 to 6 orders less for Z_{Ae}. Plates (PL), due to their large concentrations of small sizes, contribute the most of these five habits to M_A, but the least to Z_{Ae}. The dominance of graupel to M_A and Z_{Ae} values for both groups, along with no significant variation in the contribution from the other habits, indicates that variations in the graupel size distribution must account for the systematic differences between the $M_D > M_A$ and $M_D < M_A$ groups.

In Fig. 3.14, the average graupel spectra are plotted for both the $M_D > M_A$ and $M_D < M_A$ groups (the average graupel spectrum for the entire sample in Fig. 3.10 lies between the spectra here). Also plotted in Fig. 3.14 are the spectral M_A and Z_{Ae} values for the groups.

It can be seen in Figure 3.14, that there are more large graupel particles (d $\geq$ ~ 6000μm) in the $M_D > M_A$ group than in the $M_D < M_A$ group. Conversely, there are fewer small graupel particles (d < 6000μm) in the $M_D > M_A$ group than in the $M_D < M_A$ group. These particle concentration variations cause an increase in the mass distribution for particles with d $\geq$ ~ 6000μm and a decrease for particles with d < 6000μm in the $M_D > M_A$ group, relative to the $M_D < M_A$ group. The increase in mass is less than the decrease, causing a net decrease in the total mass concentration (M_A);

$$M_{A_{(M_D > M_A)}} < M_{A_{(M_D < M_A)}}$$

as seen in Figure 3.13.

47
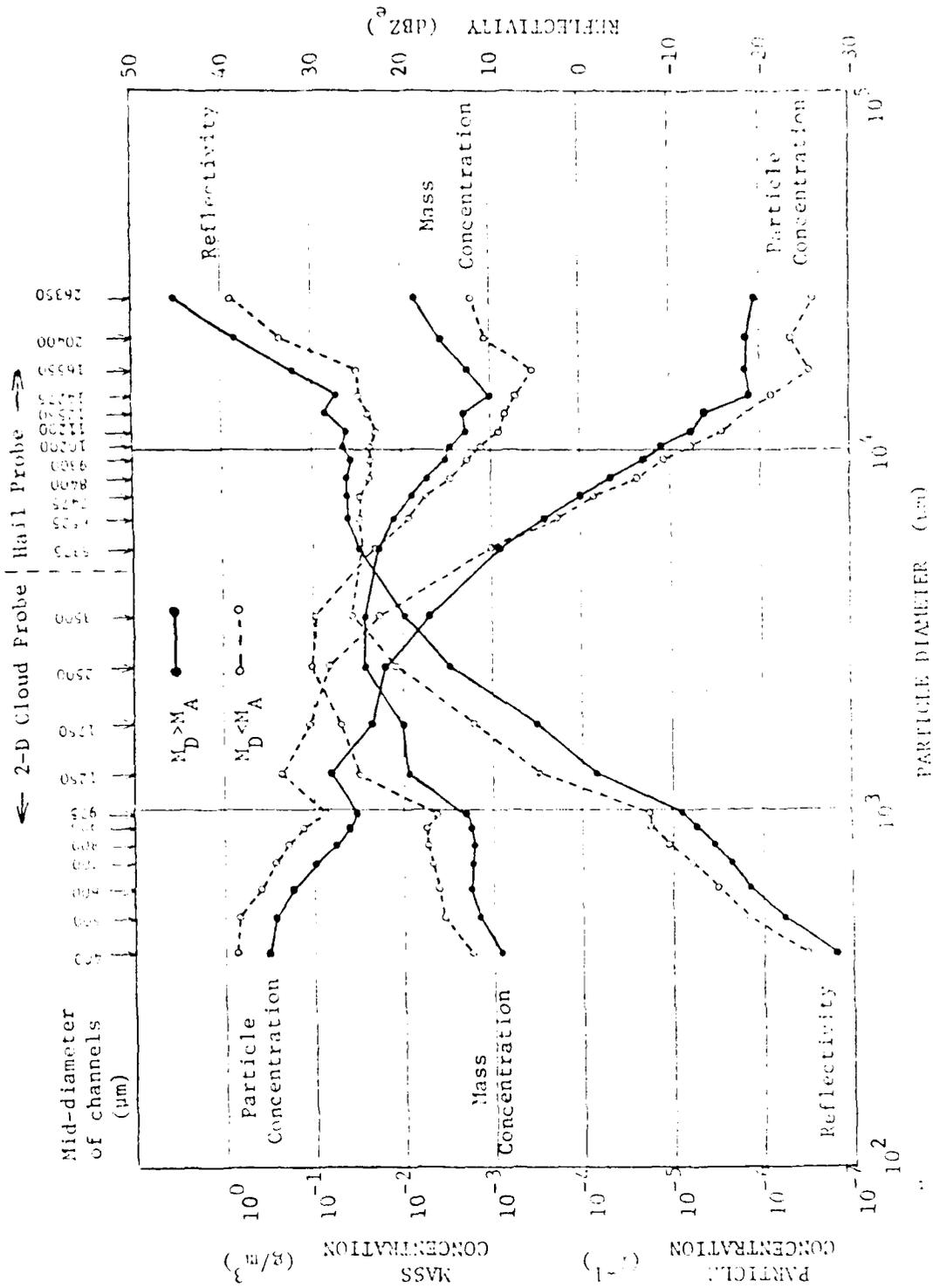
Figure 3.14: Spectral values of average graupel number and mass concentrations and corresponding reflectivity values for the 2 sets of samples, $M_D > M_A$ (solid line) and $M_D < M_A$ (dashed line). The spectral values are plotted as in Fig. 3.10.

Further, because of the variation in particle concentration, there is a corresponding variation in reflectivity values between the $M_D < M_A$ and $M_D > M_A$ groups as shown in Figure 3.13: the $M_D > M_A$ group shows an increase for particles with d > 6000 μm and a decrease for smaller particles, relative to the $M_D < M_A$ group. The increase in reflectivity values for particles with d > 6000μm is orders of magnitude greater than the decrease for smaller particles, due to Z being proportional to d^6. Thus, a net increase in $\bar{Z}_{Ae}$ results as shown in Figure 3.13;

$$\bar{Z}_{Ae_{(M_D > M_A)}} > \bar{Z}_{Ae_{(M_D < M_A)}} .$$

The larger $\bar{Z}_{Ae}$ value for the $M_D > M_A$ group predicts a larger $\bar{M}_D$ value using (3.16) than for the $M_D < M_A$ group. However, the measured mass concentration was greater for the $M_D < M_A$ group (Fig. 3.13). The reason for this discrepancy can be seen from Fig. 3.14. Given the approximate linear nature of the log-log particle concentration distribution, maximum sensitivity of M_A to particle concentration variation occurs at sizes below 6000μm, peaking near 3000μm. On the other hand, maximum sensitivity of Z_{Ae} occurs at the largest sizes (> 6000μm). Thus, samples with relatively large numbers of particles > 6000μm and/or small numbers of particles near 3000μm (represented by the $M_D > M_A$ distribution in Fig. 3.14) have larger Z_{Ae} values and/or smaller M_A values relative to the best fit Z-M relationship, giving the cluster of points below the line in Fig. 3.11. Samples with relatively large numbers of particles near 3000μm and/or small numbers of particles > 6000μm (represented by the $M_D < M_A$ distribution in Fig. 3.14) have larger M_A values and smaller Z_{Ae} values relative to the best-fit relationship, giving the cluster of points above the line in Fig. 3.11.

It also can be implied from an examination of Figs. 3.11 and 3.14 that the samples with the highest reflectivities ($\geq 10^5$ mm^6/m^3) are most likely due to the presence of hailstones $\geq$ 1 cm. Consequently, if the ten or so largest Z_{Ae} samples are eliminated from the scattergram in Fig. 3.11, the best-fit line to the remaining data would have a steeper slope, 0.256 instead of 0.196.

This analysis has shown that the graupel size distribution was most critical to the variability of the Z-M relationship in a northeast Colorado hailstorm. This variability is due to different spectral sizes at which M and Z variations are most sensitive to change in number concentrations. This conclusion supports an earlier result from our measurement and modeling studies of Florida cumulus. Consequently, accurate representation of graupel formation and the distribution of graupel particles in the 3-D numerical simulation model is critical to proper reflectivity predictions.

The total mass concentration values in Figures 3.8a and 3.8b were utilized along with the corresponding total reflectivity values in Figures 3.9a and 3.9b to compute values of 10logZ'/mass concentration for comparison with model-predicted values in Figure 3.6. The computed ratios are illustrated in Figure 3.15 Two results are apparent upon comparing the ratios in Figures 3.6 and 3.15. First, the variability in the model-predicted and measured ratios are low. Second the regions with the largest ratios are at cloud edge. These results, although based on a limited data set, are in _qualitative_ agreement. This agreement indicates that the predicted water content and reflectivity values are reasonable. This conclusion is consistent with those made from our earlier measurement and modeling studies of Florida cumulus.
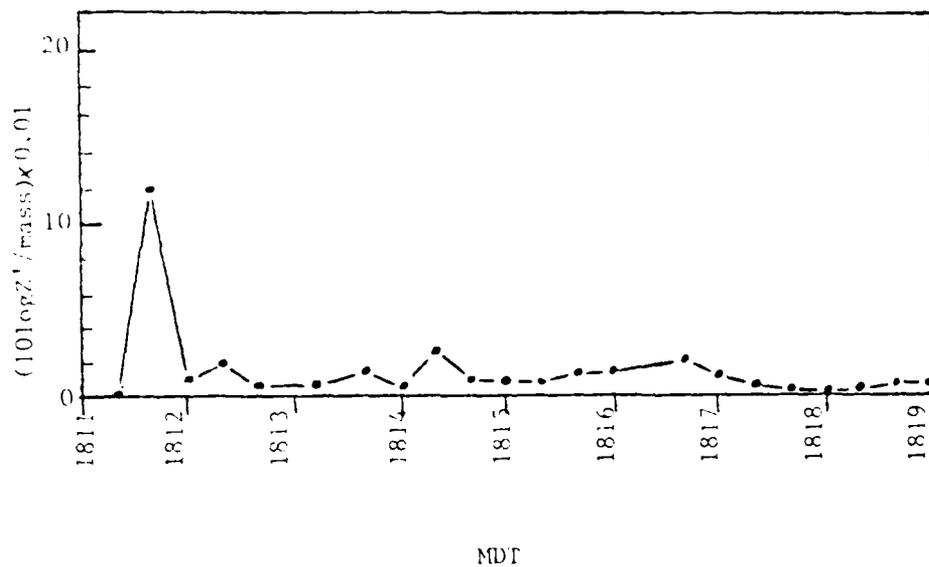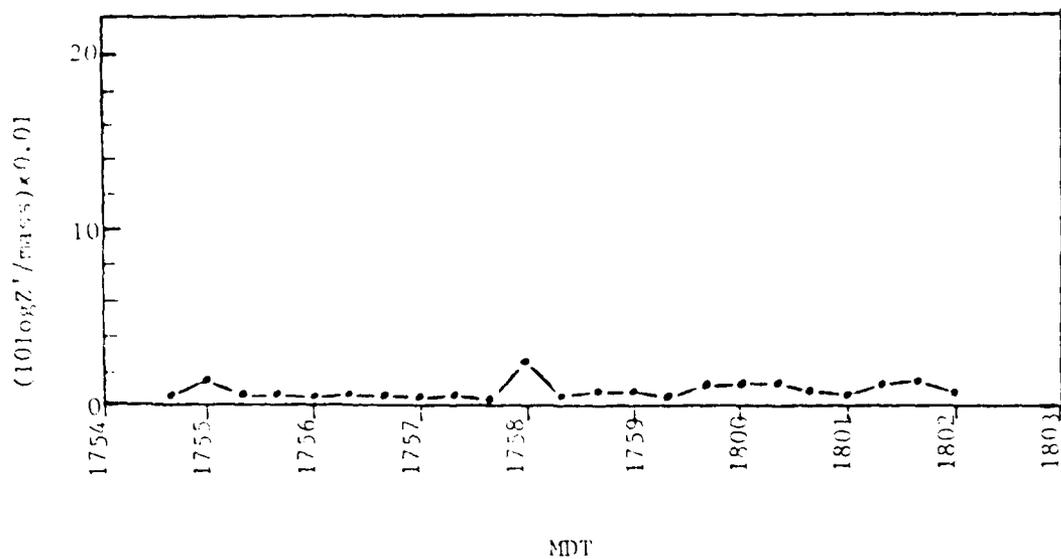
Figure 3.15: Ratios of 10logZ' (dBZ) and mass concentration M (g m^{-3}). Z' is an index of refraction-weighted reflectivity. For ice, Z' = Z x 0.19. M and Z values from Figs. 3.8 and 3.9, respectively, are used.

In summary, detailed airborne hydrometeor measurements were analyzed for a northeast Colorado hailstorm. The analyses focused on determining the variations in the relationship between water contents and radar reflectivities and the cause(s) for the variations. It was found that systematic variations existed in the hailstorm; regions where water-contents calculated from radar reflectivity values were greater than the measured contents and vice versa. The variations were caused by relatively greater concentrations of the largest graupel particles (> 6 mm dia.) combined with smaller concentrations of particles near 3 mm in regions with over-estimated water contents, and lower concentrations of particles larger than 6 mm combined with larger concentrations of particles near 3 mm in regions with under-estimated water contents.

The hydrometeor measurements were used to estimate ratios of radar reflectivity to water content for comparison with ratios calculated from 3-D model simulations. It was found that the measured and calculated ratios were in qualitative agreement: regions of high ratios occurred primarily at cloud edges where a few large graupel particles existed.

The results of this study demonstrate the importance of graupel particles to radar reflectivity measurement and calculations. Consequently, accurate representation of graupel formation and particle spectra in the 3-D numerical simulation model is critical for proper reflectivity predictions.

3.5 Explanations of Variations in M-Z Relationships

We reported in section 3.4 that systematic variations in M-Z relationships were identified that were caused primarily by variations in the concentrations of graupel particles with diameters greater than 6 mm and with diameters near 3 mm. We found that variations in Z were highly

sensitive to variations in the number-concentrations of the graupel particles $\geq$ 6 mm, while variations in M were most sensitive to variations in the number-concentrations of the particles near 3 mm. We reported an average relationship (Eq. 3.16) from our analysis of M (g m^{-3}) = 0.065 $Z_e^{0.196}$ (mm^{6}m^{-3}).

As a result of these findings, Plank (1982, personal communication) questioned why we found an exponent of ~ 0.2 instead of the 0.5 exponent used in our 3-D model. The purpose of this section is to explore that question and related questions.

It can be seen in the derivation of graupel reflectivity Z_g in Appendix A that $Z_g \propto \frac{1}{N_{tg}} M_g^2$, where the graupel mass concentration M_g is a product of air density and the graupel mixing ratio r_g. Values of r_g are the basic space- and time-dependent variable predicted by the model and drive the graupel reflectivity parameterization. In this parameterization, a Marshall-Palmer size distribution is assumed in which N_{tg}, a "total graupel number concentration," must be specified. In the South Florida cumulus simulations in section 3.3, N_{tg} was set constant, so that the Z-M relation indeed had an exponent of 0.5, or $M_g \propto Z_g^{0.5}$. Because this resulted in an apparent over-estimation of N_{tg}, especially at early stages of graupel formation, the N_{tg} formulation in the model was revised such that $N_{tg} \propto M_g$. Thus, the model M-Z relation became $M_g \propto Z_g^{1.0}$, with an exponent of 1.0 built in rather than 0.5. (Battan (1973) cites several M-Z relations for hail in which the exponent is near 1.0.)

In the following analyses, the behavior of the model M-Z relationship (with its 1.0 exponent) is compared to the empirical relationship derived in the last section (with its ~ 0.2 exponent). The M and Z

values from the *average* measured particle concentration spectrum are compared with the M and Z values from a model-parameterized Marshall-Palmer spectrum.

We consider only the total-sample average spectra in the analyses, since the differences between the model formulation and the measured spectra are much greater than those between the different measured samples. While not explicitly depicted in Fig. 3.14, the total-sample average spectra for the measured particle number and mass concentrations and reflectivities all lie between the respective $M_D > M_A$ and $M_D < M_A$ spectra.

3.5.1 Model Formulation of Graupel Particle Spectrum

The graupel particle spectrum in the 3-D model is after the Marshall-Palmer (M-P) distribution:

$$N(D) = \frac{N_{tg}}{D_o} e^{-D/D_o} \, , \qquad (3.17)$$

where $N(D)$ $[cm^{-4}]$ is the particle concentration per unit size interval at particle diameter D $[cm]$, N_{tg} $[cm^{-3}]$ is the total graupel particle concentration, and D_o $[cm]$ is a characteristic diameter of the distribution. D_o is a constant of the distribution which must be specified.

For the Florida reflectivity studies, the constant D_o is set to an equivalent melted diameter of 0.054 cm (related to a characteristic dimension of a M-P raindrop distribution which tends to stabilize due to drop breakup). N_{tg} is calculated as a function of D_o and the total graupel mass concentration, M_g $[g/cm^3]$:

$$N_{tg} = \frac{M_g}{\pi/6 \; \rho_1 \; D_o^3} \quad , \tag{3.18}$$

where M_g is a product of air density ρ_a (g/cm^3) and graupel mixing ratio r_g (g/g), ρ_1 is liquid water density (1.0 g/cm^3), and D_o is the characteristic equivalent melted particle diameter (cm). Thus N_{tg} is a derived total particle concentration, such that if all N_{tg} particles had a melted diameter D_o, the total mass concentration would be M_g.

Because radar reflectivity is proportional to the 6th power of an ice particle's equivalent melted diameter (i.e., the square of its mass), the formulation for reflectivity in the model, based on Eq. (3.17), would be more accurate if D is given in terms of melted diameter (which is currently not done). Thus, modelled spectral values of graupel reflectivity, Z_i, as well as spectral mass concentrations, M_i, depend on the assumed values of ice density, ρ_g, at the graupel size D_i. However, as will be shown, Z_i and M_i are relatively insensitive to differences in liquid vs. ice water density, compared to more dominant assumptions concerning N_{tg} and D_o.

To examine how the model would simulate the 25 July 1976 storm analyzed in section 3.4.2, we solve for N_{tg} in Eq. (3.18) using the measured average total mass concentration M_g = 0.25 g/m^3 and D_o = 0.027 cm to get N_{tg} = 2.43 x 10^{-2} cm^{-3}. Using these N_{tg} and D_o values and the mid-channel D values defined by the various channels of the 2-D cloud probe and hail spectrometer reported in Table 3.2, N(D) values were calculated using Eq. (3.17). The results are depicted in Fig. 3.16. The result using a frozen diameter directly in Eq. (3.17) is seen in Fig. 3.16 as a straight line on the log-linear plot, a characteristic of a M-P distribution. The other two lower curves of the three lower curves
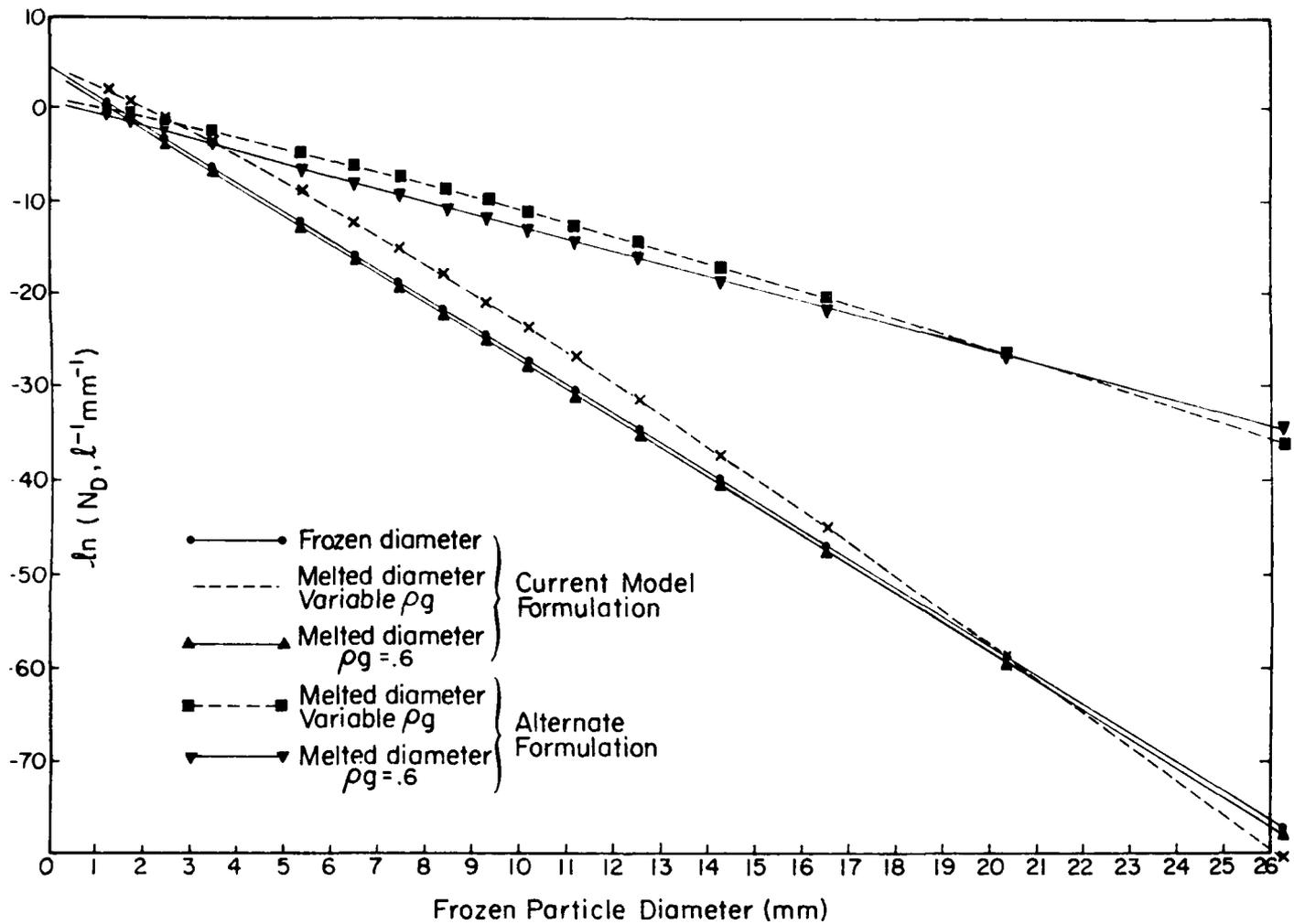
Figure 3.16: Plot of various Marshall-Palmer formulations of graupel
size distributions. Results of calculations using Eq.
(3.17) as in the current 3-D model simulations, and an
alternate form of Eq (3.17).

in Fig. 3.16 are derived from Eq. (3.17) using equivalent melted diameters corresponding to the abscissa values of frozen spectral diameter D. The plot for melted diameters using ρ_g = 0.6 g/cm^3, as assumed by the model, is a straight line, since the constant density affects D by a constant factor. The plot for melted diameters using the variable ρ_g is based on the frozen-to-melted diameter assumptions described by Heymsfield and Parrish (1979). Their formulation of density ranges from less than 0.1 g/cm^3 for the smallest graupel particles to just over 0.6 g/cm^3 for the largest. This curve would also be a straight line if plotted against the equivalent melted diameters.

The number-concentration of particles in a discrete size interval (or sensor spectral channel), N_i, is given by the integral of the curve in Fig. 3.16 over that size interval. Integrating Eq. (3.17),

$$N_i = \int_{D_1}^{D_2} N(D)\ dD = \int_{D_1}^{D_2} (N_{tg}/D_o)\ e^{-D/D_o}\ dD$$

$$= \frac{N_{tg}}{D_o} \int_{D_1}^{D_2} e^{-D/D_o} dD$$

$$= N_{tg}\left[e^{-D_1/D_o} - e^{-D_2/D_o}\right] \tag{3.19}$$

The three lower curves of N(D) in Fig. 3.16, which were based on the current model formulation of N_{tg}, were integrated over the spectral channel limits D_1 and D_2 specified in Table 3.2, using the actual frozen diameter or the appropriate equivalent melted diameter as required for each curve. The resultant 'current model formulation' particle concentration spectra are plotted in Fig. 3.17, along with the 'aircraft-

57
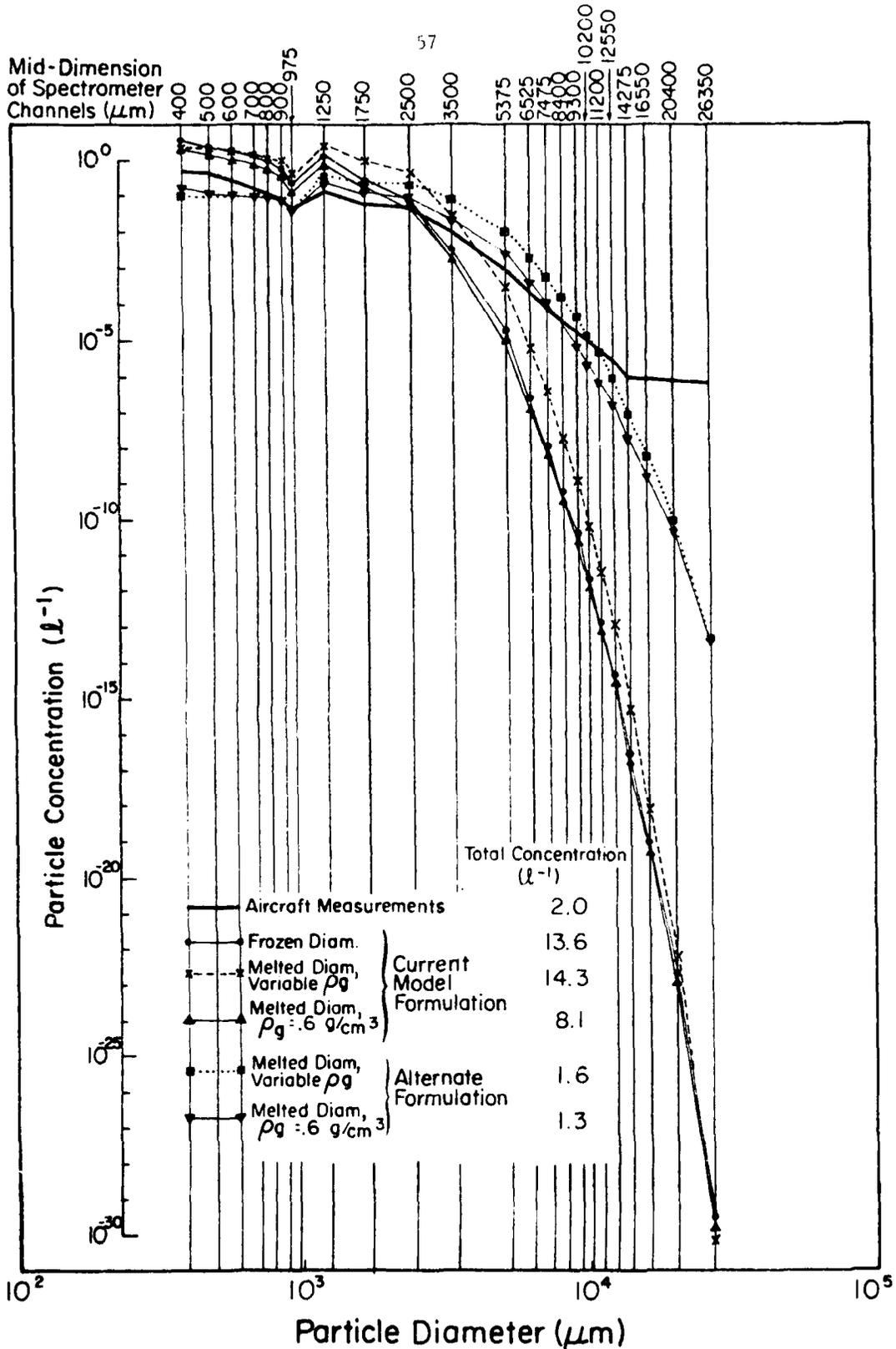
Figure 3.17: Plot of particle number concentrations integrated over spectral size channels. Measured hydrometeor size spectra ———; current 3-D model M-P spectra from Eq. (3.19) using: frozen diameters , ●, melted diameters (variable density), x , melted diameters (ρ_g = 0.6 g cm^{-3}), ▲ ; alternate M-P formulation using: melted diameters (variable ρ_g), ■, and melted diameters (ρ_g = 0.6 g cm^{-3}), ▼ .

measured' ('real') spectrum. It can be seen in Fig. 3.17 that the differences due to integrating between discrete "frozen" size intervals vs. the two melted size intervals (using two different ice density assumptions) are much less than the difference between any of the three curves and the measured spectrum. Further, smaller-sized particles are over-estimated in number by about an order of magnitude in comparison with the measured spectrum and the mid thru largest sizes are very seriously under-estimated. Due to the large magnitudes of the over-estimated concentrations of small particles, the modelled total particle concentrations are several times larger than the measured total concentration (see total concentrations summarized at the bottom of Fig. 3.17).

3.5.2 Model Formulation of Graupel Mass Concentration and Reflectivity Spectra

The modelled mass concentration spectra, corresponding to the 'current model formulation' particle concentration spectra in Fig. 3.17 are depicted in Fig. 3.18, along with the aircraft-measured mass concentration spectrum. The appropriate ice density assumptions as assumed by Heymsfield and Parrish (1979), variable ρ_g) and as used in the model (ρ_g = 0.6 g/cm^3), respectively, were applied to produce the two 'current model formulation' curves (the 'frozen diameter' curve corresponding to the third 'current model formulation' curve in Fig. 3.17 has been omitted, since using either ρ_g assumption at this point produces no significant differences from the other curves). As can be seen in Fig. 3.18, differences between the modelled and measured mass concentration spectra are similar to the differences in the particle concentration spectra in Fig. 3.17: mass in the smaller size channels is over-estimated with
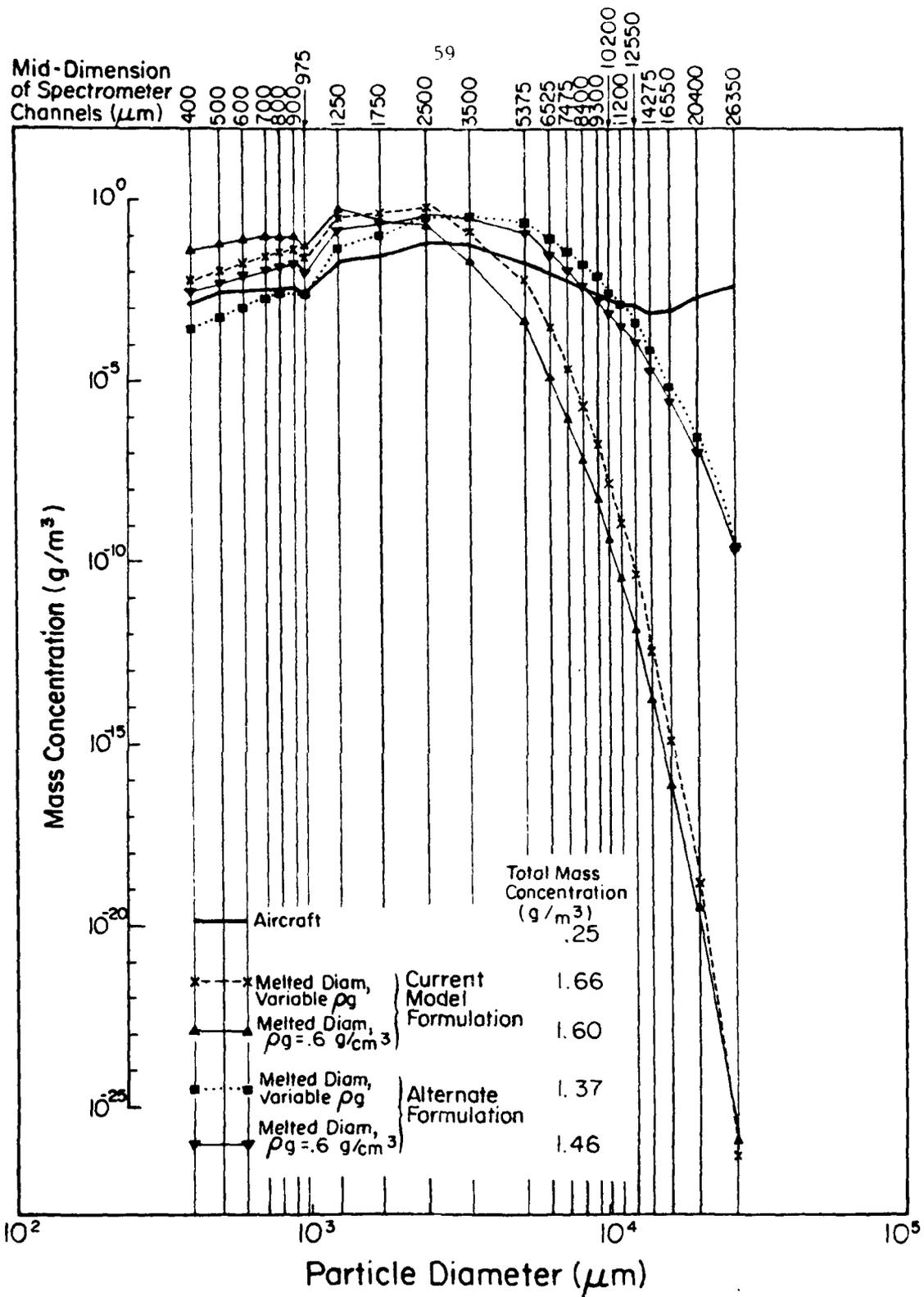
Figure 3.18: Measured and modelled spectral hydrometeor mass concentrations. Symbols same as in Fig. 3.17.

respect to the aircraft measurements, while at the large sizes, mass is very much under-estimated. Due to the large magnitudes of the over-estimates at the smaller sizes, the total mass concentrations are over-estimated by several times (see total mass concentration summaries at the bottom of Fig. 3.18).

The effect of the differences between modelled vs. measured particle concentration spectra shown in Fig. 3.17 on the 'current model formulation' vs. measured radar reflectivity spectra is shown in Fig. 3.19. It can be seen, that the reflectivities calculated from the 'current model formulation' particle concentration spectra, using the two ρ_g assumptions, vary insignificantly from each other, compared to the variation between either modelled spectrum and the aircraft-measured reflectivity spectrum. The modelled reflectivity spectra have similar trends, relative to the measured spectrum, as are exhibited by the modelled particle and mass concentration spectra: the spectral Z_i values are over-estimated at the small particle sizes because of the over-estimated number of small particles, while the reverse is true at the large particle sizes. However, the net effect on the modelled total reflectivity is opposite from the net effect on the modelled total mass concentration. Since the D^6 dependency of $Z(D)$ causes Z to be highly sensitive to large particles, the over-estimate of Z with respect to the measured values at small sizes (due to the over-estimate of particle concentrations at small sizes) is more than offset by the under-estimate of Z at large sizes (due to the many-orders under-estimate of large-particle concentrations). Indeed, the aircraft Z_i values peak at the large sizes, where the corresponding modelled Z_i values are negligible. The resultant total modelled reflectivity is an order of magnitude less than
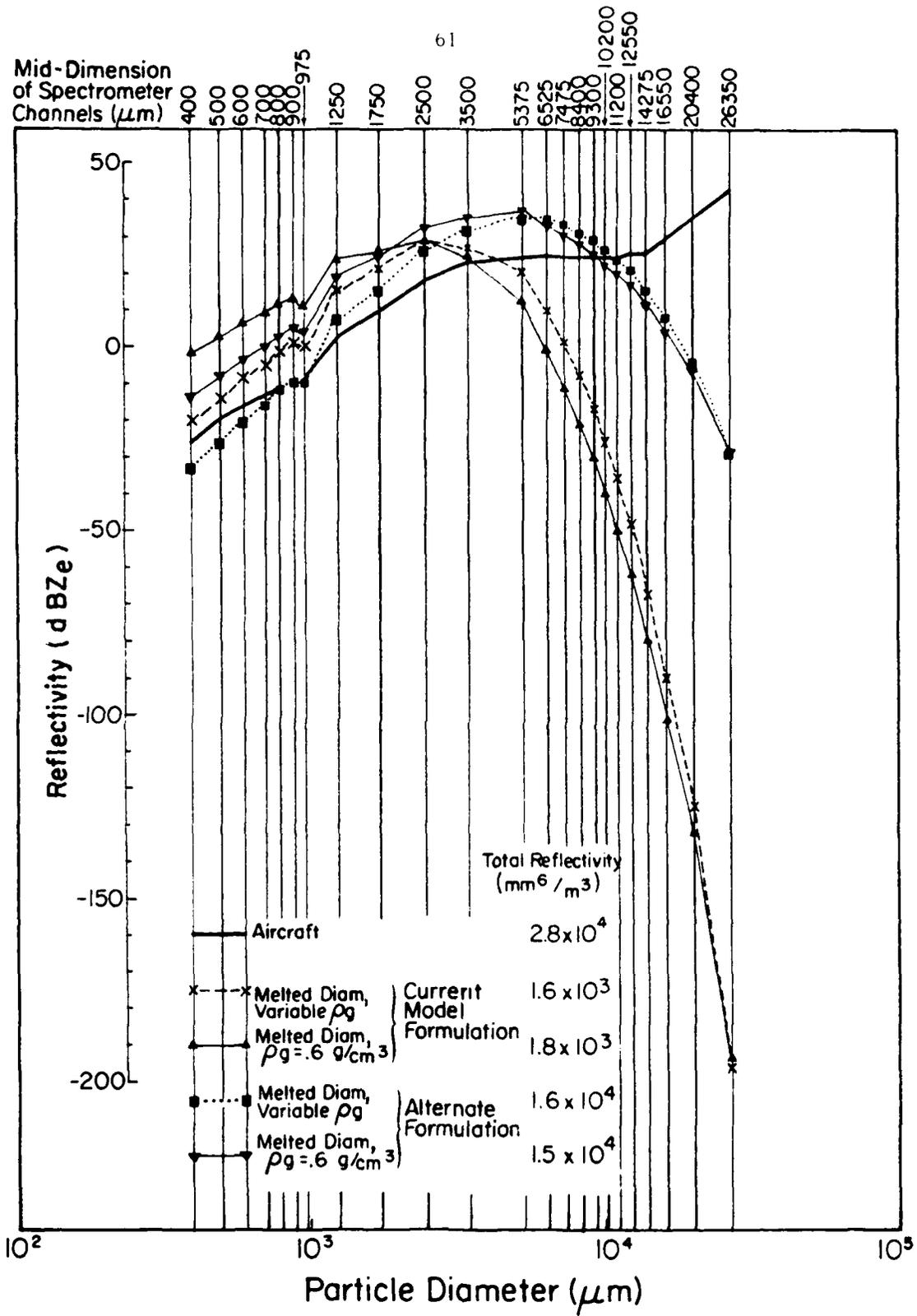
Figure 3.19: Measured and modelled spectral radar reflectivities.
Symbols are the same as in Fig. 3.17.

that measured (see total reflectivity summary at the bottom of Fig. 3.19).

Thus, the model formulation of a M-P distribution using the constants as specified in Eq. (3.18) result, for this comparison with measured hydrometeor spectra, in an over-estimate of total graupel mass concentration and an under-estimate of total graupel reflectivity, relative to the measured. Hence, either of the modelled parameters a and/or b (where b = 1.0, since $N_{tg} \alpha M_g$) in the modelled $M = aZ^b$ relation would appear to be too large.

3.5.3 Alternate Model Formulation of Graupel Spectra

What is clearly needed, as seen in Fig. 3.17, is a modelled distribution with fewer small particles and more large ones. The question is, can a M-P distribution do this? A more representative distribution can be accomplished, to some extent, by modelling a distribution with a flatter slope and a smaller intercept in Fig. 3.16; i.e., from Eq. (3.17), a larger value of D_o and/or a smaller value of N_{tg}. It should be noted that the previous value of N_{tg} was based on studies of raindrop spectra, and that this variable has yet to be 'calibrated' for graupel spectra. Thus, to accomplish the desired adjustments, we based a simple alternate formulation of N_{tg} on the measured total particle concentration (over all spectral channels) from Fig. 3.17. The new value of N_{tg} is 2.05×10^{-3} cm^{-3}. The value is an order of magnitude less than the value from Eq. (3.18) which was based on the measured mass concentration. Instead of assuming a characteristic particle size D_o of 0.027 cm, as before, we now compute D_o from the measured total particle and mass concentrations:

$$\frac{\pi}{6} \rho_1 \times D_o^3 = \frac{M_g}{N_{tg}} = \frac{2.5 \times 10^{-7} \text{ g/cm}^3}{2.05 \times 10^{-3} \text{ cm}^{-3}} = 1.222 \times 10^{-4} \text{ g}$$

$$D_o = 0.0616 \text{cm} \quad . \tag{3.20}$$

Note that we have reformulated N_{tg} and D_o in terms of an average measured particle concentration spectrum. Since the model predicts only r_g as a basic variable and not the particle concentration, this reformulation would not be able to be implemented into the model. Furthermore, since no explicit formulation of N_{tg} in terms of M_g is provided by this illustrative reformulation, its effect on the modelled $Z_g \propto \frac{1}{N_{tg}} M_g^2$ relation (and thus on the exponent in the $M = aZ^b$ relation) cannot be examined. It serves here only to modify the constants N_{tg} and D_o (and thus the slope and intercept) in the modelled Marshall-Palmer distribution. The modification yields reformulated spectral M and Z values that can be compared to the first formulation.

The resulting alternate M-P distributions are shown in Fig. 3.16 (using the identical ice density assumptions used for the various curves in the first formulation). As seen in Fig. 3.17, integration of the new N(D) curves over discrete intervals clearly gives reduced concentrations in the smaller channels and larger concentrations at the larger channels than with the first formulation. The resultant net concentrations are much closer to the measurements (see bottom of Fig. 3.17). The measured curve is better reproduced, with the errors now being under-estimation at the smallest sizes, over-estimation at mid sizes, and reduced under-estimation of large particle concentrations.

The spectral mass concentrations resulting from the alternate M-P spectra are shown in Fig. 3.18. It can be seen in Fig. 3.18, that the

region of over-estimation has been shifted to the middle part of the spectrum (still an order of magnitude too high), and the M_i values at the large-particle sizes remain under-estimated. The total mass concentrations are corrected slightly in the right direction, but the values remain several times larger than the measured values.

The spectral reflectivities (Fig. 3.18) calculated from the alternate M-P spectra show improvement. The total Z values are now within a factor of 2 of the values calculated from the airborne hydrometeor spectra. Note that the increase in total Z has been achieved by over-estimating Z_i values resulting from mid-size particles between 0.2 to 1.0 cm, while still grossly under-estimating the most significant measured Z_i values resulting from particles with sizes > 1 cm.

The alternate M-P formulation results in increased Z and decreased M (both towards the measured values), suggesting a reformulated Z-M relationship that is closer in line to the measured 0.2 exponent. It should again be stressed that the model does not have a 0.5 exponent 'built in', because while Z is proportional to the mass concentration squared (inverse of 0.5), it is also inversely proportional to N_{tg}, which is also related to mass concentration either directly [as in (3.18)] or indirectly through some sort of D_o parameterization.

For this particular case, it seems unlikely that the measured particle number-concentration 'tail' at the large end of the spectrum in Fig. 3.17 can be modelled with a M-P distribution, regardless of the adustments to N_{tg} and D_o. The 'tail' is due to the presence of large hail in this particular storm, where a raindrop-type breakup mechanism would not provide a stable anchor to the large-particle end of the graupel spectrum. Hence the hydrometeor spectra may defy M-P description.

3.5.4 Conclusions

The M-Z relationship derived in the section 3.4, $M = 0.065Z_e^{0.196}$, resulted in an exponent that is significantly less than the 0.5 to 1.0 value often cited in the literature. The 0.2 exponent was due to the presence of large hail in some of the samples.

The measured hydrometeor size distribution was compared with the Marshall-Palmer (M-P) approximation currently formulated, based on constants N_{tg} and D_o, in the 3-D model. It was found that these constants have much more significant impact on M and Z than do the assumptions concerning ice density. With the current M-P formulation, it was found that particles < 2.5 mm diameter are over-estimated in number by about an order of magnitude, in comparison with the measured size distribution, and the particles > 2.5 mm are seriously under-estimated. These differences produce corresponding over-estimations and under-estimations at the small-particle and large-particle ends, respectively, of both the modelled mass concentration and reflectivity spectra, relative to the measured M and Z spectra. However, total M is more sensitive to the over-estimations of the small-particle concentrations, while total Z is most sensitive to the under-estimations of large-particle concentrations. Thus, the M-P distribution, using N_{tg} and D_o constants as presently specified in the 3-D model, results in an over-estimate of total mass concentration and an under-estimate of total reflectivity, relative to the measured total M and Z values. Hence, an exponent of 0.5 to 1.0 appears to be too large for the M and Z values resulting from analysis of northeast Colorado hailstorm data.

Accordingly, an illustrative alternate M-P distribution was derived using measured total particle concentrations for N_{tg} (which cannot be

explicitly predicted by the model), and D_o was computed using N_{tg} and measured total mass concentration. The alternate M-P formulation resulted in increased Z values and decreased M values, suggesting a modelled M-Z relationship closer to agreement with the 0.2 exponent resulting from the hailstorm analysis.

For this particular case, it seems unlikely that the measured particle number-concentration 'tail' at hail sizes > 1.4 cm can be modelled with a M-P distribution, regardless of the adjustments to N_{tg} and D_o. Consequently, improved formulations of graupel spectra are needed.

M vs. Z relationships were ivestigated in three climatic regions during this study. In section 3.2, reflectivities were predicted for a South Park, Colorado thunderstorm using existing M-Z relationships in the 3-D numerical model. In section 3.3, reflectivities and particle mass concentrations were measured in Florida thunderstorms but too coarsely to develop rigorous M vs. Z relationships. In section 3.4 and 3.5, M-Z relationships were derived from airborne particle size-distribution measurements and a size distribution - Z relationship from Heymsfield and Parrish (1979). It can be seen from these investigations, no consistent analysis was applied to the three climatological regions. Consequently, it was not possible to draw conclusions as to the geographic or climatic contributions to the variability of M-Z relationships. What can be said from these analyses, through, is that regions where low number concentrations of large hail stones are produced, anomalous M-Z variations will occur.

3.6 Appendix A

Radar Reflectivity Algorithms

by William R. Cotton

In our analysis of radar reflectivity and its variability with liquid water content, we shall apply the Rayleigh approximation to the radar equation. Thus the power returned to the radar from an ensemble of cloud precipitation elements is

$$\overline{P}_r = \left[\frac{8\pi^5}{g} \left(\frac{P_t \theta \phi h A_p^2}{\lambda^6} \right) \frac{1}{r^2} \right] |K|^2 \sum_{vol} D_i^6 \quad .$$

The terms in [   ] are all properties of the radar and distance r from the radar and are defined in Battan (1973). For our purposes, the remaining terms are the main area of investigation. The term $|K|^2$ is a function of the complex index of refraction of the scattering elements. For an all water cloud, $|K|^2$ is approximately 0.93 and for ice particles, $|K|^2$ is 0.19. In our analysis of model results, we shall assume that ice particles in the melting zone are water-coated and therefore have a $|K|^2$ of 0.93.

Normally, meteorologists employ the so-called reflectivity factor Z to designate the effects of the particle-size distribution on the reflected power returned to the radar,

$$Z = \sum_{vol} n_i D_i^6 \quad .$$

In our analysis, we shall define a complex index of refraction-weighted reflectivity $\tilde{Z}$ such that

$$\tilde{Z} = |K|^2 \sum_{vol} n_i D_i^6 \quad .$$

Reflectivity factor $\tilde{Z}$ for Rain, r_r

It is assumed that

$$\phi(r) = \frac{N_r}{r_m} e^{-r/r_m} \quad .$$

Thus,

$$\tilde{Z} = |K_\ell|^2 \int_0^\infty (2r)^6 \phi(r) dr = |K_\ell|^2 \int_0^\infty (2r)^6 \frac{N_r}{r_m} e^{-r/r_m} dr$$

$$\tilde{Z} = |K_\ell|^2 \, 2^6 \, \frac{N_r}{r_m} \int_0^\infty r^6 \, e^{-r/r_m} dr \quad ,$$

where $|K_\ell|^2 = 0.93$.

Let

$$x = r/r_m \Rightarrow dr = r_m dx$$

$$\tilde{Z} = 2^6 \, \frac{N_r}{r_{/m}} \, |K_\ell|^2 \, r_m^6 \int_0^\infty x^6 \, e^{-x} \, dx$$

$$\tilde{Z} = 2^6 \, N_r r_m^6 \, \Gamma(7) \, |K_\ell|^2 \quad .$$

But

$$N_r = \frac{\rho_o r_r}{8\pi\rho_w r_m^3} \quad .$$

Thus

$$\tilde{Z}_r = \frac{2^6 \Gamma(7) r_m^3}{8\pi\rho_w} \, \rho_o |K_\ell|^2 \, r_r \quad .$$

Thus, $\tilde{Z}$ increases linearly with the rainwater content r_r. It is also interesting to note that $\tilde{Z}$ has a cubic dependence on the assumed characteristic radius r_m of the raindrop distribution.

Reflectivity factor for Graupel r_g

For graupel, $\tilde{Z}$ is

$$\tilde{Z} = |K_i|^2 \int_0^\infty D^6 N(D) e^{-\lambda D} dD$$

since

$$N(D) = N_{tg} \lambda e^{-\lambda D} \ ,$$

then

$$\tilde{Z} = |K_i|^2 N_{tg} \lambda \int_0^\infty D^6 e^{-\lambda D} dD \ ,$$

or letting $x = \lambda D \Rightarrow dx = \lambda dD$,

$$\tilde{Z} = |K_i|^2 N_{tg} \frac{1}{\lambda^6} \int_0^\infty x^6 e^{-x} dx$$

$$\tilde{Z} = \frac{|K_i|^2 N_{tg}}{\lambda^6} \Gamma(7) \ .$$

But

$$\lambda = \left(\frac{\pi \rho_g N_{tg}}{\rho_a r_g} \right)^{1/3} \Rightarrow \frac{1}{\lambda^6} = \frac{\rho_a^2 r_g^2}{\pi^2 \rho_g^2 N_{tg}^2} \ .$$

Thus

$$\tilde{Z}_g = \frac{\Gamma(7) \rho_a^2}{\pi^2 \rho_g^2 N_{tg}} |K_i|^2 r_g^2 \ .$$

where $N_{tg} = \rho_a r_g / \pi 6 \rho_\ell D_{mg}^3$

Thus, for graupel, $\tilde{Z}$ is proportional to $r_g^{\ 2}$ and inversely proportional to N_{tg}.

Reflectivity factor for Ice Crystals r_i

For ice crystals, $\tilde{Z}$ is given by

$$\tilde{Z} = |K_i|^2 \, N_i d_i^{\ 6} \quad ,$$

where N_i is the crystal concentration defined externally in many cases by the Fletcher formula, and

$$d_i = k_1 \, m_i^{\ \frac{1}{2}} \quad , \quad \text{where } k_1 = 0.515 \text{ mgm}^{-\frac{1}{2}} \text{ for } m_i < 1.7 \times 10^{-7} \text{gm, and}$$

$$k_1 = 0.192 \text{ mgm}^{-\frac{1}{2}} \text{ for } 1.7 \times 10^{-7} \text{ gm} \leq m_i < 1 \times 10^{-5} \text{ gm,}$$

and

$$d_i = k_1 \, m_i^{\ 0.417} \quad \text{for } m_i > 1 \times 10^{-5} \text{ gm, and}$$

$$k_1 = 8.89 \times 10^{-2} \text{ mgm}^{-0.417} \quad ,$$

and

$$m_i = \frac{r_i \rho_a}{N_i} \quad .$$

Since d_i is nearly always proportional to $m_i^{\ \frac{1}{2}}$, this shows that for ice crystals

$$\tilde{Z}_i \; \alpha \; r_i^{\ 3}/N_i^{\ 2} \quad .$$

Summary

In summary, depending upon the particular form of water substance and the assumed distribution functions for these respective components, the relationship between reflectivity factor $\tilde{Z}$ and water content varies as follows:

For rain only

$$\tilde{Z}_r \ \alpha \ |K_\ell|^2 \ r_m^{\ 3} \ r_r \quad ,$$

For graupel only

$$\tilde{Z}_g \ \alpha \ |K_i|^2 \ \frac{r_g^{\ 2}}{N_{tg}} \quad ,$$

For ice crystals

$$\tilde{Z}_i \ \alpha \ |K_i|^2 \ \frac{r_i^{\ 3}}{N_i^{\ 2}} \quad .$$

In the supercooled portions of a simulated cloud, we see that $\tilde{Z}$ varies substantially with total precipitation water r_p($r_p = r_r + r_g + r_i$) depending on the relative contributions of r_r, r_g and r_i. We should also note that $|K_i|^2$ will be assumed equal to that of pure ice, except below the melting level where we assume that $|K_i|^2 = |K_\ell|^2$.

To analyze the variability of $\tilde{Z}$ with r_p, we shall define $\tilde{Z}_r$ as the reflectivity factor computed as if all precipitation were in the form of rain,

$$\tilde{Z}_r \ \alpha \ |K_\ell|^2 \ r_m^{\ 3} \ r_p \quad .$$

Also, we define $\tilde{Z}_p = \tilde{Z}_r + \tilde{Z}_g + \tilde{Z}_i$, and then plot in our analyses.

$\dfrac{\tilde{Z}_p}{\tilde{Z}_r}$ along with plots of $\tilde{Z}_p$ and r_r, r_g, r_i, r_p .

4.0 Three-Dimensional Cloud/Mesoscale Model Investigations of Potential

Aircraft Icing Regions

4.1 Background

The problem of predicting aircraft icing conditions is primarily

one of predicting the amount of supercooled liquid water content in a

cloud. Simple as this problem may seem, it actually represents a very

challenging meteorological problem. This is because the amount of

supercooled liquid water content is the residual of the differences

between large production and removal mechanisms. Liquid water is

primarily produced by adiabatic cooling and occasionally by radiative

cooling. However, liquid water is removed from the cloud by entrainment

processes and precipitation processes. In a supercooled cloud this

means removal by supercooled rain, vapor deposition growth of ice

crystals (i.e., via the Bergeron-Findeisen mechanism), accretion or

riming growth of ice particles including pristine ice crystals, graupel

particles and aggregates of snow crystals, and the precipitation of

those particles.

In an earlier simulation of orographic clouds, Cotton et al. (1982)

concluded that an ice-crystal aggregation model was needed to properly

predict observed amounts of precipitation and supercooled liquid water.

Moreover, the ice-phase competition for supercooled water is greatly

dependent upon the concentration of ice crystals. Thus, two new

developments in the microphysical model are needed to better predict the

conditions suitable for aircraft icing conditions. These are:

i)   an ice crystal aggregation scheme

ii) prediction of the concentration of ice-crystals due to primary

and secondary nucleation, and removal by collection by other

precipitation species and by precipitation.

4.2 Ice Crystal Aggregation Model

4.2.1 Conversion of Ice Crystals to Aggregates

The rate of collection among a homogeneous population of ice crystals is given by

$$\frac{dN_i}{dt}\bigg]_{CN} = - K_i N_i^2 \qquad (4.1)$$

where N_i represents the concentration of "pristine" (non-aggregated) crystals in our model and K_i is the collection cross section.

The conversion rate of ice crystal mixing ratio r_i to aggregates

$$CN_{ia} = - \frac{m_i}{\rho_o} \frac{dN_i}{dt}\bigg] = + K_i N_i r_i \qquad (4.2)$$

where the average crystal mass m_i is given by

$$m_i = \frac{r_i \rho_o}{N_i} \qquad (4.3)$$

and ρ_o is the air density. [Note in our sign convention CN indexed ia (CN_{ia}) represents a positive contribution to aggregates, whereas CN_{ai} represents a negative contribution.] A pure sedimentation model for aggregation applied to our homogeneous population of pristine crystals gives $K_i = 0$. Therefore, to estimate K_i we adapt Passarelli and Srivastava's (1978) stochastic collection kernel model which estimates K_i based on a distribution of particle densities for equal-sized crystals. This model reduces to

$$K_i = \frac{\pi D_i^2}{6} V_i E_i X \qquad (4.4)$$

where X is a measure of the variance in particle fall speed, D_i and V_i are the average crystal diameter and fall speed, respectively. Passarelli and Srivastava's best estimate of X is 0.25, which we will use as a first guess on x. We plan to experimentally adjust x on specific observed cases to calibrate K_i.

4.2.2 The Distribution of Aggregates

Based on data reported by Rogers' (1974) and personal discussions with Passarelli we assume aggregates are distributed in the form

$$N(D) = \frac{N_T}{D_m} e^{-D/D_m} \qquad (4.5)$$

where N(D) represents the spectral density of aggregates of diameter D, N_T is the total aggregate concentration and D_m is a "characteristic" diameter of the aggregate population. From Roger's (1974) data, we estimate

$$D_m = 0.33 \text{ cm}$$

Employing the aggregate density relationship given by Passarelli and Srivastava (1978):

$$\rho_{ia} = \beta_1 D^{-0.6} \qquad (4.6)$$

where $\beta_1 = 0.015$ g m$^{-2.4}$ and integrating over the entire distribution (4.5), we find

$$N_T = 0.641 \beta_1^{-1} \rho_0 D_m^{-2.4} r_a \qquad (4.7)$$

where r_a represents the mixing ratio of aggregates.

The terminal velocity of aggregates is given by

$$V_a = \left[\frac{4g}{\rho_o}\right]^{1/2} C_D^{-1/2} \rho_{ia}^{1/2} D^{1/2} \tag{4.8}$$

where g is the acceleration due to gravity, and C_D is the drag coefficient here taken to be $C_D = 1.3$. Substitution of (4.6) into (4.8) gives us:

$$V_a = 2\left[\frac{g \beta_1}{\rho_o C_D}\right]^{1/2} D^{0.2} \tag{4.9}$$

Also substitution of (4.6) into (4.5) gives us

$$N(D) = 0.641 \beta_1^{-1} \rho_o r_a D_m^{-3.4} e^{-D/D_m} \tag{4.10}$$

4.2.3 Aggregates Collecting Ice Crystals

Once "pristine" ice crystals have been converted to aggregates distributed according to (4.10), the aggregates can collect "pristine" ice crystals. The change in concentration of crystals by aggregation is given by

$$\frac{dN_i}{dt}\bigg]_{CL} = - K(D_a,D_i) N_i N(D_a) d D_a \tag{4.11}$$

For large aggregates collecting pristine ice crystals, we can employ the standard gravitational collection kernel,

$$K(D_a, D_i) = \frac{\pi}{4}(D_a + D_i)^2 |V_a - V_i| E(a/i) \tag{4.12}$$

where we approximate

$$|V_a(D_a) - V_i| \simeq |\overline{V_a} - \overline{V_i}|$$

The average terminal velocity of ice aggregates is given by

$$\overline{V_a} = \frac{\int\limits_0^\infty V_a(D_a)\, m(D_a)\, N(D_a)\, dD_a}{r_a\, \rho_o} \tag{4.13}$$

which after substitution of (4.8), (4.10), and (4.6) becomes:

$$\overline{V_a} = 2.49\, \beta_1^{0.5} \left[\frac{g}{\rho\, C_D}\right]^{1/2} D_m^{0.2} \tag{4.14}$$

We can now estimate the change in aggregate mixing ratio due to collection as

$$CL_{ia} = -\left.\frac{m_i}{\rho_o}\frac{dN_i}{dt}\right]_{CL} = \frac{r_i}{N_i}\int\limits_0^\infty K(D_a, D_i)\, N_i\, N(D_a)\, d\, D_a \tag{4.15}$$

Substitution of (4.12), (4.14), and (4.10) into (4.15) and integration we find

$$CL_{ia} = 0.503\, \beta_1\, \rho_o\, E(a/i)\, |\overline{V_a} - \overline{V_i}|\, D_m^{-2.4}x \tag{4.16}$$
$$(2\, D_m^2 + 2\, D_i\, D_m + D_i^2)\, r_a\, r_i$$

We have experimented with several models of collection efficiency $E(a/i)$ and E_i in (4.16) and (4.4) based on data reported by Passarelli and Srivastava (1978), (1974), Hallgren and Hosler (1960) and Hosler and

Hallgen (1960). The temperature-influences on collection efficiency are evaluated from diagnosed surface temperatures for crystals growing by riming and vapor deposition. We have also assumed the hydrodynamic collision efficiency is 1.4 as evaluated in one case by Passarelli and Srivastava (1978) over the temperature range -12 to -15°C. Sensitivity experiments with these models demonstrated that the Hosler and Hallgren model results in an underestimate of aggregation formation and an incorrect vertical distribution of aggregates where $E \simeq 1.4$ results in a realistic vertical distribution of aggregates and reasonable snowfall rates.

4.2.4 Aggregate Riming

The growth of a single aggregated particle by riming can be approximated as

$$\frac{dM_a}{dt}\Bigg|_{RM} = \frac{\pi D^2}{4} \left| V_a - V_c \right| E(a/c) \, \rho_0 \, r_c \tag{4.17}$$

Assuming $V_a \gg V_c$ and applying (4.17) to a population of aggregates,

$$RM_{ca} = \frac{1}{\rho_0} \int_0^\infty \frac{dM_a}{dt}\Bigg|_{RM} N(D) \, dD \tag{4.18}$$

which gives us after integration and substitution of (4.17) and (4.5)

$$RM_{ca} = 2.42 \left[\frac{g \, \rho_0}{C_D \beta_1}\right]^{1/2} E(a/c) \, r_a \, r_c \, D_m^{-0.2} \tag{4.19}$$

where $E(a/c)$ is evaluated similar to individual crystals collecting cloud droplets (see Cotton et al., 1982).

4.2.5 Aggregate Collision with Raindrops

Aggregates can also collide with supercooled raindrops leading to a loss in concentration of raindrops

$$\frac{d\phi(R)dR}{dt} = - \int_0^\infty \pi(R + D/2)^2 \; |V(R) - V_a(D)| E(R/a)\phi(R)N(D)dRdD \tag{4.20}$$

as well as a loss in concentration of aggregates

$$\frac{dN(D)}{dt} \, dD = - \int_0^\infty \pi(R + D/2)^2 |V(R)-V_a(D)| E(R/a)\phi(R)N(D)dRdD \tag{4.21}$$

and providing a source of graupel. The change in mixing ratio of graupel due to collision between aggregates and supercooled raindrops is given by

$$CL_{rag} + CL_{arg} = \frac{1}{\rho_o} \int_0^\infty m(R)\frac{d\phi(R)}{dt}dR + \frac{1}{\rho_o} \int_0^\infty m(D)\frac{dN(D)}{dt}dD \tag{4.22}$$

which after some manipulation become

$$CL_{rag} = 2.530\rho_\omega\beta^{-1}|\overline{V_R} - \overline{V_a}|E(R/a)r_a N_R R_m^3 D_m^{-.24} \left[40R_m^2 + 8R_m D_m + D_m^2\right] \tag{4.23}$$

and

$$CL_{arg} = 6.32 \; r_a N_R|\overline{V_R}-\overline{V_a}|E(R/a)(R_m^2 + 1.7 \; R_m D_m + 1.87 \; D_m^2) \tag{4.24}$$

where the appropriate raindrop parameters are given in Cotton et al. (1982) and Tripoli and Cotton (1980).

4.2.6 Aggregate Vapor Deposition

The rate of mass growth of a single aggregate particle by vapor deposition can be approximated as:

$$\frac{dM_a}{dt}\bigg]_{VD} = 4\pi C \ G(T,D) \ f(R_e) \ (S_i - 1) \tag{4.25}$$

where C, the capacity is evaluated as a spherical particle thus

$$C = D/2,$$

$f(R_e)$ is the ventilation function and S_i is the saturation ratio with respect to ice. The change in aggregate mass due to vapor deposition is then given as

$$VD_{va} = \int_o^\infty \frac{1}{\rho_o} \frac{dM_a(D)}{dt} \ N(D) \ dD \tag{4.26}$$

which when integrated over the entire spectrum of aggregates becomes:

$$VD_{va} = 4.03 \ D_m^{-1.4} \ \beta_1^{-1} \ G(T,P) \ f(R_e) \ (S_i - 1) \ r_a \tag{4.27}$$

4.2.7 Melting of Aggregates

We treat the melting of aggregates in a similar manner to the melting of graupel particles (see Cotton et al., 1982). Consider an aggregate falling through a cloudy environment at temperature $T > 0^oC$ (T_f) and accreting cloud droplets having a temperature T and colliding with raindrops also at temperature T. It is assumed that the melting aggregate is in thermodynamic equilibrium with a surface temperature T_f such that

$$L_{li} \left. \frac{dm_a}{dt} \right]_{melt} = -2\pi D \left[Kf(R_e)(T-T_f) + L_{vi} \, \psi \, f(R_e)(\rho_v - \rho_{vs}(T_f)) \right]$$

$$- \left[\left. \frac{dm_a}{dt} \right]_{RM} + \left. \frac{dm_a}{dt} \right]_{CL} \right] c_w \, (T-T_f) \tag{4.28}$$

Application of (4.28) to the spectrum of aggregates give us:

$$ML_{ar} = -4.03 \; f(R_e) \; L_{il}^{-1}\beta_1^{-1}D_m^{-1.4} r_a (K(T-T_f) + L_{vi} \, \psi \rho_o (r_v - r_{vs}(T_f))$$

$$- \frac{1}{L_{il}} (RM_{ca} - CL_{rag}) \; c_w(T-T_f) \tag{4.29}$$

4.2.8 Aggregate Collection by Graupel

Aggregates can be collected by graupel particles thereby contributing to the mixing ratio of graupel particles. The change in concentration of aggregates of diameter $D \pm \delta D$ by colliding with graupel of diameter $D_g + \delta D_g$ is given by

$$\frac{dN(D)}{dt} dD = - \int_0^\infty \frac{\pi(D+D_g)^2}{4} \left| V(D) - V(D_g) \right| E(a/g) N(D) N(D_g) dD dD_g \tag{4.30}$$

The change in mixing ratio of aggregates is then

$$CL_{ag} = - \frac{1}{\rho_o} \int_0^\infty M(D) \; \frac{dN(D)}{dt} \; dD \quad , \tag{4.31}$$

which after integrating over the graupel and aggregate spectra becomes:

$$CL_{ag} = -1.57 \left| \overline{V_a} - \overline{V_g} \right| E(a/g) N_{tg} \; r_a (7.5 \; D_m^2 + 3.4\lambda^{-1} \; D_m + \lambda^{-2}) \tag{4.32}$$

4.2.9 Conversion of Aggregates to Graupel Due to Heavy Riming

If the riming rate on aggregates exceeds a certain amount we presume that the aggregates become a source for graupel.

Thus, we convert aggregates to graupel at the rate:

$$CN_{ag} = - \ MAX \ [RM_{ca} - B] \quad , \tag{4.33}$$

where B is a threshold for conversion. We estimate B as 20% of the graupel-equivalent riming rate given by

$$RM = K_{rg} \ E(glc) \ r_c r_a^{5/6}$$

where $K_{rg} = 1.16 \ (g/C_D)^{1/2} \left[\dfrac{\rho_o}{\rho_g}\right]^{1/3} N_{tg}^{1/6}$

4.2.10 Summary of Model Equations for Water Substance

The following is a summary of the relevant equations pertaining to the aggregate population:

$$\overline{V_a} = 2.49 \left[\frac{\beta_1 \ g}{\rho_o \ C_D}\right]^{1/2} D_m^{0.2} \tag{4.34}$$

$$CL_{ia} = 0.503 \ E(a/i)D_m^{-2.4} \rho_o |\overline{V_a} - \overline{V_i}| (2D_m^2 + 2D_m D_i + D_i^2) r_a r_i \tag{4.35}$$

$$RM_{ca} = 2.42 \ D_m^{-0.2} \left[\frac{g \ \rho_o}{C_D \ \beta_1}\right]^{1/2} E(a/c) \ r_a r_c \tag{4.36}$$

$$CL_{rag} = - \frac{(40 \ R_m^2 + 8 \ R_m D_m + D_m^2)}{\beta_1 \ D_m^{2.4}} \ E(R/a) \ \rho_o \ |\overline{V_a} - \overline{V_R}| r_a r_r \tag{4.37}$$

$$CL_{arg} = 0.25 \frac{(R_m^2 + 1.7 \, R_m D_m + 1.87 \, D_m^2)}{\rho_w \, R_m^3} \, E(R/a) \, \rho_o |\overline{V}_a - \overline{V}_R| r_a r_r \tag{4.38}$$

$$VD_{va} = \frac{4.03}{D_m^{-1.4} \, \beta_1} \, G(T,p) f(R_e) S_i^{-1} r_a \tag{4.39}$$

$$ML_{ar} = - \beta_1 \, D_M^{1.4} \, \frac{4.03}{L_{i1}} \, f(R_e) \left[K(T-T_f) + L_{iv} \rho_o (r_v - r_{vs}(T_f)) \right]$$

$$- \frac{c_w}{L_{i1}} \, (T-T_f)(RM_{ca} - CL_{rag}) \tag{4.40}$$

$$CL_{ag} = - 3.37 \, E(a/g) \, N_{tg} |\overline{V}_a - \overline{V}_g| \left[1.61 \, D_m^2 + 4.98 \, D_m \left[\frac{\rho_o \, r_g}{\rho_g \, N_{tg}} \right]^{1/3} \right.$$

$$\left. + (\frac{\rho_o \, r_g}{\rho_g \, N_{tg}})^{2/3} \right] r_a \tag{4.41}$$

$$CN_{ag} = -AMAX1 \left[(RM_{ca} - f_1 \, 1.16(\frac{g}{C_D})^{1/2} (\frac{\rho_o}{\rho_g})^{1/3} N_{tg}^{1.6} E(g/c) r_c r_a^{5/6}), 0 \right] \tag{4.42}$$

$$CN_{ag} = -MAX(Rm_{ca} - B, 0)$$

When combined with the water substance equations described in Cotton et al. (1982) a complete set of equations governing the distribution of water substance in the model is then given.

4.3 Summary of Conservation Equations for Ice Crystals

As can be seen in Eq. (4.1), the rate of production of aggregates

is proportional to N_i^2. Therefore it is necessary to develop a parallel equation for the continuity of ice crystal concentration.

The conservation equations for concentration of ice crystals (N_i) contains the following processes:

i) nucleation of ice by deposition

ii) nucleation of ice by contact freezing

iii) ice multiplication by the Hallett-Mossop mechanism

iv) removal of N_i by

    a) melting

    b) conversion to graupel

    c) collection by rain, graupel or aggregates

    d) precipitation

v) transport and diffusion

In order to simplify the transport and diffusion of crystal concentration, it is convenient to predict specific concentration (N_i/ρ_o). The conservation equation is then

$$\frac{\partial (N_i/\rho_o)}{\partial t} = - U_j \frac{\partial (N_i/\rho_o)}{\partial x_j} - \frac{\overline{\partial U_j (N_i/\rho_o)}}{\partial x_j} + NPR_i$$

$$+ \frac{N_i}{\rho_o r_i}\left[ML_{iv} + (CN_{ig} - CL_{ri}) + CL_{ig}\right]$$

$$+ NNUA_{vi} + \max(0, NNUB_{vi} + NNUC_{vi} + NNUD_{vi})$$

$$+ NSP_{vi} \qquad\qquad (4.43)$$

where NPR_i is the precipitation tendency of specific crystals concentration, ML_{iv} is the loss of crystal mixing ratio to melting, CN_{ig} - CL_{ri} is the loss of crystal mixing ratio to conversion to graupel and

CL_{ig} is the loss of crystal mixing ratio to collection by graupel. We consider nucleation by deposition ($NNUA_{vi}$) and contact nucleation due to Brownian diffusion ($NNUB_{vi}$), thermophoresis ($NNUC_{vi}$) and diffusiophoresis ($NNUD_{vi}$). Finally, production of specific concentration by Hallett-Mossop splintering ($NSFP_{vi}$) is considered. For a description of the terminology see Cotton et al. (1982). The precipitation term NPR_i is given by

$$NPR_i = - \frac{\partial V_i (N_i/\rho_0)}{\partial z} \tag{4.44}$$

where V is the crystal terminal velocity. The terms ML_{iv}, CN_{ig}, CL_{ri} and CL_{ig} are described by Cotton et al. (1982). Next we will describe the nucleation and splintering models.

4.3.1 Nucleation by Deposition

Empirical results of Fletcher (1962) show that, for a water saturated parcel, depositional nucleation will produce a relationship between temperature and concentration given by:

$$N_i = N_{io} \, e^{\beta_2 T_s} \tag{4.45}$$

where $N_{io} = 10^{-8} cm^{-3}$ and $\beta_2 = 0.6 C^{-1}$ and $T_s = (273.16-T)$. Differentiating Eq. (4.45) with respect to z we obtain

$$\frac{\partial N_i}{\partial z} = \beta_2 \, N_{io} \, e^{\beta_2 T_s} \frac{\partial T_s}{\partial z} \tag{4.46}$$

If we neglct the variation of temperature in the horizontal and time compared to the vertical, then

$$\left. \frac{\partial N_i}{\partial t} \right]_{dep} = w\beta_2 N_{io} \; e^{\beta_2 T_s} \; \frac{\partial T_s}{\partial z} \tag{4.47}$$

or, for specific concentration

$$NNUA_{vi} = \max\left[0., \frac{w\beta_x N_{io}}{\rho_o} \; e^{\beta_2 T_s} \; \frac{\partial T_s}{\partial z} \right] \tag{4.48}$$

4.3.2 Contact Nucleation

For a model of contact nucleation we shall follow the model that Young (1974) referred to as model A. Young considers contact by Brownian diffusion, thermophoresis and diffusiophoresis. Brownian-diffusion contact nucleation results from the random collision of aerosol particles with cloud droplets. Thermophoresis contact nucleation occurs due to the attraction or repulsion of aerosol particles to the droplet along the gradient of thermal diffusion. Diffusiophoresis contact nucleation, on the other hand, occurs due to the attraction or repulsion of aerosol particles to the droplet along the gradient of vapor diffusion. Hence, the net effect of thermophoresis and diffusiophoresis will be to inhibit contact nucleation in regions of supersaturation and have the opposite effect where subsaturation occurs. Since, as Young points out, thermophoresis is dominant, these processes can be important to the problem of aircraft icing.

For Brownian diffusion, the change in specific concentration is

$$NNUB_{ri} = F_1 \; DF_{ar} \tag{4.49}$$

where DF_{ar} is the aerosol diffusivity and where

$$F_1 = \frac{4\pi R_c N_c N_a}{\rho_o} \qquad (4.50)$$

We approximate the activated aerosol concentration by

$$N_a = N_{ao}(270.16 - T_c)^{1.3} \qquad (4.51)$$

where $N_{ao} = 2 \times 10^{-1}$ cm^{-3} at sea level. Young assumed N_{ao} decreased linearly with height to 1×10^{-2} cm^{-3} at 5000m MSL. We will assume a constant value of 2×10^{-1} cm^{-3} for now. Given the cloud droplet concentration (N_c), and the cloud water mixing ration r_c, the cloud droplet radius is given by

$$R_c = \left[\frac{\overline{r_c}\rho_o}{\frac{4}{3}\pi N_c \rho_w} \right]^{1/3} \qquad . \qquad (4.52)$$

Similarly, for thermophoretic contact nucleation, we scale Young's equations to obtain:

$$NNUC_{vi} = F_1 F_2 f_t \qquad (4.53)$$

where

$$F_2 = \frac{K}{p} (T-T_c) \quad , \qquad (4.54)$$

and K is the thermal conductivity of the air, T_c is the cloud droplet temperature and p is the atmospheric pressure. The function f_t is given by

$$f_t = \frac{.4[1+1.45K_n+.4K_n\exp(-1/K_n)](K+2.5K_nK_a)}{(1+3K_n)(2K+5K_aK_n+K_a)} \tag{4.55}$$

where K_n is the Knudsen number given by

$$K_n = \frac{7.37T}{288pr_a} \tag{4.56}$$

and r_a is the assumed aerosol radius of 3×10^{-5} cm. The aerosol thermal conductivity, K_a, is assumed to be 5.39×10^{-4} ergs^{-1}cm^{-1}K^{-1}.

Finally, we approximate diffusiophoresis contact nucleation by

$$NNUD_{vi} = F_1 \, DF_v \, \frac{(e_v - e(r_c))}{p} \tag{4.57}$$

where DF_v is the vapor diffusivity and e_v and $e(r_c)$ are the vapor pressures at infinity and the droplet surface. For a droplet in thermal equilibrium it can be shown that:

$$DF_v \, \frac{3_v - e(r_c))}{p} = F_2 \, \frac{R_v T}{L_{vl}} \quad , \tag{4.58}$$

therefore we can express diffusiophoresis contact nucleation as

$$NNUD_{bi} = F_1 F_2 \, \frac{R_v T}{L_{vl}} \quad . \tag{4.59}$$

Hence the sum of the contact nucleation may be written

$$NNUB_{vi} + NNUC_{vi} + NNUD_{vi} = F_1\left[DF_{ar} + F_2(f_t - \frac{R_v T}{L_{1v}})\right] \tag{4.60}$$

Since the quantity F_2 is dependent on $T-T_c$, the proper evaluation

of thermophoretic and diffusiophoretic contact nucleation must include a realistic estimation of this temperature difference. Assuming thermal equilibrium,

$$T - T_c = - \frac{G(T,p)(S-1)L_{vl}}{K} \qquad (4.61)$$

where $G(T,p)$ is the portion of mass tendency of a water particle resulting from vapor diffusion to or from the particle, since we normally diagnose cloud water in the model $(S-1)$ is zero thus both thermophoresis and diffusionphoresis would always be zero. In order to estimate a supersaturation, we assume $(S-1)$ results from a balance between production and removal mechanisms of supersaturation. We assume the dominant removal is by diffusional growth of cloud droplets and ice crystals and neglect all other growth processes. The dominant production is by temperature change in response to vertical motion. Following Tripoli and Cotton (1980) we write the production as

$$P_s = - \frac{dr_s}{dt} - \frac{\frac{\overline{w} r_s}{T_v} \frac{g}{R} (\frac{\varepsilon L_{vl}}{C_p \overline{T}} - 1)}{\frac{\varepsilon L_{vl}^2 r_s}{R C_p \overline{T}^2} + 1} \qquad (4.62)$$

where w is vertical velocity, $\overline{r}_s$ is saturation mixing ratio, T_v is virtual temperature, g is gravity acceleration, $\varepsilon = .611$, and C_p is specific heat at constant pressure. The dissipation of supersaturation D_s is given by

$$D_s = \frac{r_s}{r_v} \left[\frac{\overline{dr_c}}{dt} + \frac{\overline{dr_i}}{dt} \right] \quad ,$$

where

$$\frac{\overline{dr_c}}{dt} \Bigg]_{vd} = \frac{4\pi}{\rho_0} G(T,p)(S-1)N_c R_c \qquad (4.63)$$

and

$$\frac{\overline{dr_i}}{dt} \Bigg]_{vd} = VD_{vi} \quad . \qquad (4.64)$$

For a steady state supersaturation,

$$P_s = D_s \quad , \qquad (4.65)$$

or combining Eqs. (4.63) - (4.65) and (4.52) and assuming $(\frac{r_s}{r_v}) \simeq 1$, we obtain

$$(S-1) = \frac{-\rho_0 (VD_{vi} + \frac{dr_s}{dt})}{4\pi G(T,p)N_c R_c} \qquad (4.66)$$

4.3.3 Ice Multiplication

To model ice multiplication we shall make use of a parameterization of the Hallett-Mossop theory developed by Gordon and Marwitz (1981). Two mechanisms are parameterized:

1. Hallett and Mossop (1976) reported that approximately 350 ice splinters are produced for every 10^{-3} grams of rime accreted on graupel particles at $-5^{\circ}C$. The parameterization evaluates the rate

of crystal production as

$$P_p(I) = 3.5 \times 10^5 g^{-1} \left.\frac{dM}{dt}\right]_{riming} f_1(T_f) \qquad (4.67)$$

where $\left.\dfrac{dM}{dt}\right]_{riming}$ is the riming rate of an ice crystal or grapel

particle. The function $f(T_f)$ is given by:

$$f_1(T_f) = \begin{bmatrix} 0 & T > 270.16 \\ \dfrac{T - 268.16}{2} & 270.16 \geq T \geq 268.16 \\ \dfrac{T - 268.16}{3} & 268.16 \geq T \geq 265.16 \\ 0 & 265.16 \geq T \end{bmatrix} \qquad (4.68)$$

where T_f is the temperature of the crystal.

2. Approximately one ice crystal is produced for every 250 drops greater than 2×10^{-4} cm radius accreted onto each graupel particle at -5°C (Mossop, 1976). The ice crystal production rate per particle is then

$$P_p(II) = \frac{1}{250} \frac{\pi D_g^2}{4} \bar{V}_g E(g/c_{12}) N_{12} f_1(T_f) \qquad (4.69)$$

where N_{12} is the concentration of cloud droplets greater than 12×10^{-4} cm in radius, $E(g/c_{12})$ is the efficiency of collision between graupel particles and cloud droplets greater than 12×10^{-4} cm, $\bar{V}_g$ is the terminal velocity of graupel and D_g is the diameter of graupel.

To estimate the concentration of droplets greater than 12×10^{-4} cm in radius, we assume that the cloud droplet distribution is given by a Gamma distribution of the form:

AD-A142 690   MODEL CLOUD RELATIONSHIPS(U) COLORADO STATE UNIV FORT   2/2
              COLLINS DEPT OF ATMOSPHERIC SCIENCE   W R COTTON ET AL.
              30 OCT 83 AFGL-TR-84-0028 F19628-82-K-0003

UNCLASSIFIED   F/G 4/2   NL
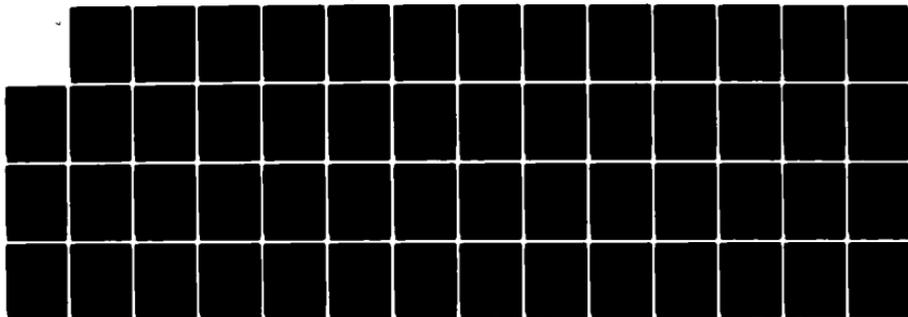
END
DATE
FILMED

8-84
DTIC
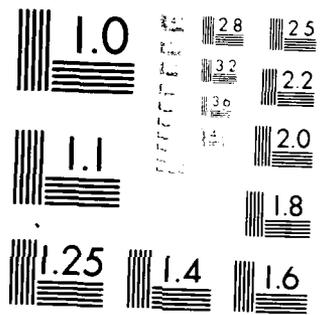
MICROCOPY RESOLUTION TEST CHART

$$f(r) = \frac{N_c r^{\alpha-1} e^{-r/\beta}}{\Gamma(\alpha)\beta^{\alpha}} \quad , \quad 0 < r < \infty \tag{4.70}$$

where Cotton (1970) showed that

$$\alpha = \frac{1}{\gamma_r^2} \tag{4.71}$$

where γ_r is the radius dispersion. We choose the typical value of $\gamma_r = 0.18$.

Furthermore, Cotton showed that

$$\beta = \left[\frac{3M_c}{4\pi\alpha(\alpha+1)(\alpha+2)}\right]^{1/2} \tag{4.72}$$

where

$$M_c = \frac{r_c \rho_o}{N_c} \quad . \tag{4.73}$$

The concentration of droplets having radii greater than 12×10^{-4} cm is then

$$N_{12} = \int_{r_{12}}^{\infty} f(r)dr = \frac{N_c}{\Gamma(\alpha)\beta^{\alpha}} \int_{o}^{\infty} r^{\alpha-1} e^{-r/\beta} dr \tag{4.74}$$

Letting $X = r/\beta(M_c)$, we find:

$$N_{12} = N_c \, f_3(M_c) \tag{4.75}$$

where

$$f_3(M_c) = \frac{1}{\Gamma(\alpha)} \int_{x=r_{12}/\beta(M_c)}^{\infty} X^{\alpha-1} e^{-X} dX \quad . \tag{4.76}$$

The evaluation of this incomplete gamma function is shown in Figure 1. It is also shown to a good approximation that

$$f_3(m_c) \begin{bmatrix} 0 & m_c < 1.26 \times 10^{-6}g \\ +2.27\ln m_c + 13.39 & 1.26 \times 10^{-6}g \leq m_c \leq 3.55 \times 10^{-6}g \\ 1 & m_c > 3.55 \times 10^{-6}g \end{bmatrix} \tag{4.77}$$

Applying Eqs. (4.69) and (4.67) to simulated riming tendencies we obtain

$$NSP_{ri} = \frac{1}{\rho_o} \left[\beta_5 \rho_o + 4 \times 10^{-3} \frac{N_c}{\bar{r}_c} f_3(M_c) \right]$$
$$\left[f_1(T_i) CL_{ci} + f_1(T_g) CL_{cg} + f_1(T_a) CL_{ca} \right] \tag{4.78}$$

where $\beta_5 = 3.5 \times 10^5 g^{-1}$.

Eq. (4.78) is then complete except for the evaluation of T_i, T_g and T_a. Assuming thermal equilibrium,

$$T_i = T + \frac{.25\rho_o}{D_i K N_i} (L_{vi} VD_{vi} + L_{il} CL_{ci}) \tag{4.79}$$

$$T_g = T + \frac{0.65}{K} \left[\frac{\rho_g \rho_o^2}{\bar{r}_g N_{tg}} \right]^{1/3} (L_{il} CL_{cg} + L_{vi} VD_{vg}) \tag{4.80}$$
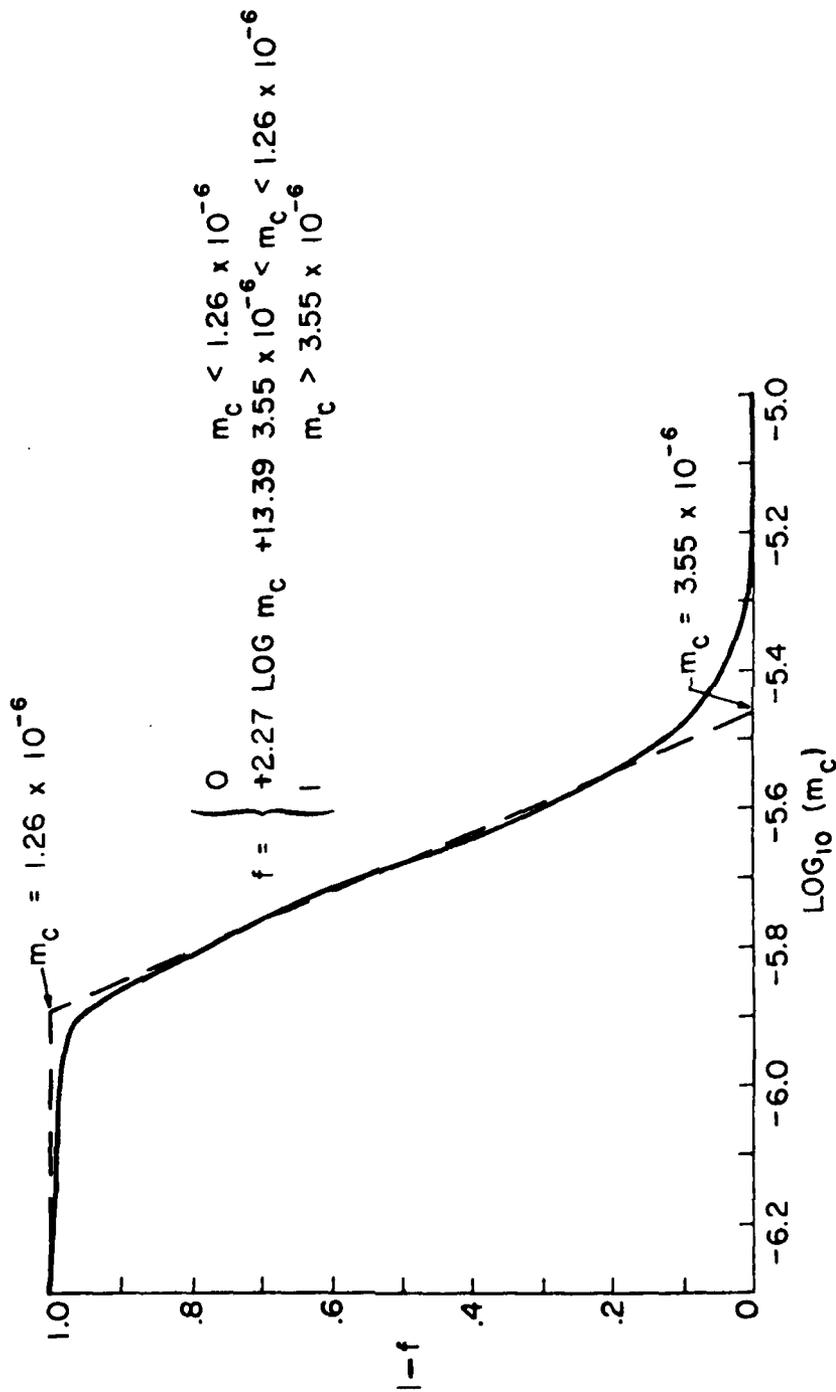
Figure 4.1: Approximation of incomplete gamma function to determine percent of cloud droplets size greater than 10 μm assuming droplets in gamma distribution, dispersion: γ = .018.

$$T_a = T + 0.25\rho_w \frac{D_{ma}^2}{K\bar{r}_a} (L_{vi}VD_{va} - L_{il}CL_{ca})$$

(4.81)

where D_i is the mean ice crystal diameter and N_{tg} is the graupel concentration.

4.4 Results of Experiments

The application of our aggregation and ice crystal concentration models to an orographic case study has thus far demonstrated the following

1) The ice nucleation deposition equation produced too many crystals at cold temperatures and was insignificant compared to other terms at warm temperatures. Therefore we elected to ignore it at the present.

2) Aggregates were produced only when the collection efficiency was enhanced at the colder temperature, i.e., -12 to -15°C.

3) Supercooled water diminished as nucleation took place. The mixing ratio of supercooled water was found to be very sensitive to contact nucleation. Apparently a close balance occurs between thermophoresis and diffusiophoresis contact nucleation. When one is limited, many more crystals are produced and much less liquid water exists. This is because a larger number of small crystals drive the Bergeron-Findeisen growth process more efficiently.

More experimentation is being done, but so far we have found an interesting relationship between nucleation and the existence of supercooled liquid water. The production of aggregates also affected the existence of liquid water because it removed large numbers of ice crystals and thus affected the overall balance.

5.0 Inclusion of Ice Processes in the Existing 1D Cloud/Turbulence Model

5.1 Introduction

Chen and Cotton (1983b) have described a one-dimensional higher order turbulence model which was applied to the simulation of a cloud-capped atmospheric boundary layer (ABL). The model has exhibited considerable skill in quantitatively reproducing the features of a marine ABL that have been predicted with Deardorff's (1980) three-dimensional large-eddy simulation (LES) model. More recently, the model has been tested against observations of a stable, marine ABL reported by Brost et al. (1982ab). The model has also been successful in reproducing the observed features reported by Brost et al. (1982ab) including the effects of wind shear and of drizzle on cloud organization. It, therefore, seemed natural to investigate the feasibility of expanding this cloud system into the ice-phase. To begin with we shall adopt the following notation.

Mean Equations

$\overline{VD}_{ab}$ = vapor diffusion

$\overline{CL}_{ab}$ = collection

$\overline{CN}_{ab}$ = conversion

$\overline{ML}_{ab}$ = melting

$\overline{NUA}_{ab}$ = nucleation by deposition

$\overline{NUB}_{ab}$ = nucleation by Brownian collection

$\overline{NUC}_{ab}$ = nucleation by thermophoresis

$\overline{NUD}_{ab}$ = nucleation by diffusiophoresis

$\overline{SP}_{ab}$ = splintering formation of ice crystals

$\overline{SH}_{ab}$ = shedding

Subscripts of the above terms define the source (second subscript) and sink (first subscript) water categories between which the transfer is made. The subscripts are also used with mixing ratios to define which category the mixing ratio is assigned. The water categories are as follows:

$v \equiv$ vapor

$c =$ cloud water

$r \equiv$ rain

$i =$ ice crystals

$g \equiv$ graupel

$a \equiv$ aggregates

When a process description is preceeded by the letter 'N' the term refers to an ice crystal concentration tendency.

Turbulence Equations

VD''_{ab} = turbulence contribution to vapor diffusion

CL''_{ab} = turbulence contribution to collection

CN''_{ab} = turbulence contribution to auto conversion

ML''_{ab} = turbulence contribution to melting

SH''_{ab} = turbulence contribution to shedding

The turbulence contributions to the nucleation by deposition, Brownian collection, thermophoresis, diffusiophoresis and splintering of ice crystals are not included.

r_T = total water mixing ratio

θ_{il} = ice-liquid water potential temperature

The method of deriving ensemble-average mean equations and second order turbulence equations has been reported by Cotton and Anthes (1983). Basically, we decompose every variable ϕ into Reynold's averaging mean $\bar{\phi}$ and perturbation ϕ'', i.e. $\phi = \bar{\phi} + \phi''$. In the following sections, we will introduce the summary of the mean equations, then the perturbation equations.

5.2 Summary of the Mean Equations and Microphysical Processes

5.2.1 Mean Equations

Rain Water

$$\frac{\partial \bar{r}_r}{\partial t} = - \frac{\partial}{\partial x_j} \bar{u}_j \bar{r}_r - \frac{\partial}{\partial x_j} \overline{u_j'' r_r''} - \frac{1}{\rho_o} \frac{\partial}{\partial z} (\rho_o \bar{V}_T \bar{r}_r)$$

$$+ \overline{VD}_{vr}$$

$$+ \overline{CL}_{cr} + \overline{CN}_{cr}$$

$$- \overline{CL}_{ri}$$

$$- \overline{CL}_{rg} + \overline{ML}_{gr} + \overline{SH}_{gr}$$

$$- \overline{CL}_{ra} + \overline{ML}_{ar} + \overline{SH}_{ar} \tag{5.1}$$

Ice Water

$$\frac{\partial \overline{r}_i}{\partial t} = - \frac{\partial}{\partial x_j} \overline{u}_j \overline{r}_i - \frac{\partial}{\partial x_j} \overline{u_j''r_i''} - \frac{1}{\rho_o} \frac{\partial}{\partial z} (\rho_o \overline{V}_i \overline{r}_i)$$

$$+ \overline{VD}_{vi} - \overline{ML}_{iv} + \overline{SP}_{vi}$$

$$+ \overline{NUA}_{vi} + \overline{NUB}_{vi} + \overline{NUC}_{vi} + \overline{NUD}_{vi}$$

$$+ \overline{CL}_{ci}$$

$$+ \overline{CL}_{ri}$$

$$- \overline{CL}_{ig} - \overline{CN}_{ig}$$

$$- \overline{CL}_{ia} - \overline{CN}_{ia} \tag{5.2}$$

Graupel Water

$$\frac{\partial \bar{r}_g}{\partial t} = - \frac{\partial}{\partial x_j} \bar{u}_j \bar{r}_g - \frac{\partial}{\partial x_j} \overline{u_j'' r_g''} - \frac{1}{\rho_o} \frac{\partial}{\partial z} (\rho_o \bar{V}_g \bar{r}_g)$$

$$+ \overline{VD}_{vg}$$

$$+ \overline{CL}_{cg}$$

$$+ \overline{CL}_{rg} - \overline{ML}_{gr} - \overline{SH}_{gr}$$

$$+ \overline{CL}_{ig} + \overline{CN}_{ig}$$

$$+ \overline{CL}_{ag} + \overline{CN}_{ag} \tag{5.3}$$

Aggregate Water

$$\frac{\partial \bar{r}_a}{\partial t} = - \frac{\partial}{\partial x_j} \bar{u}_j \bar{r}_a - \frac{\partial}{\partial x_j} \overline{u_j'' r_a''} - \frac{1}{\rho_o} \frac{\partial}{\partial z} \rho_o \bar{v}_a \bar{r}_a$$

$$+ \overline{VD}_{va}$$

$$+ \overline{CL}_{ca}$$

$$+ \overline{CL}_{ra} - \overline{ML}_{ar} - \overline{SH}_{ar}$$

$$+ \overline{CL}_{ia} + \overline{CN}_{ia}$$

$$- \overline{CL}_{ag} - \overline{CN}_{ag} \tag{5.4}$$

Ice Crystal Concentration

$$\frac{\partial}{\partial t} \left[\frac{\bar{N}_i}{\rho_o} \right] = - \frac{\partial}{\partial x_j} \bar{u}_j \left[\frac{\bar{N}_i}{\rho_o} \right] - \frac{\partial}{\partial x_j} \left[\frac{\overline{u_j'' N_i''}}{\rho_o} \right] - \frac{\bar{N}_i}{\rho_o^2} \frac{1}{\bar{r}_i} \frac{\partial}{\partial z} (\rho_o \bar{V}_i \bar{r}_i)$$

$$+ \overline{NNUA}_{vi} + \overline{NNUB}_{vi} + \overline{NNUC}_{vi} + \overline{NNUD}_{vi}$$

$$+ \overline{NSP}_{vi} + \overline{NML}_{iv}$$

$$+ \overline{NCN}_{ig} + \overline{NCL}_{ig}$$

$$+ \overline{NCN}_{ia} + \overline{NCL}_{ia} \tag{5.5}$$

5.2.2 Microphysics

The parameterization of microphysics follows the same scheme described in Section 4. However, because of the introduction of turbulence, some additional terms can be found in the following equations. For instance, the rate of accretion of cloud water by rain water is given by $CL_{cr} = a_2 r_c r_r$ (Note: Coefficients a_1, a_2 ... are defined in the Appendix, Section 5.5). Here the average accretion rate is given by $\overline{CL}_{cr} = a_2 (\bar{r}_c \bar{r}_r + \overline{r_c'' r_r''})$. Chen and Cotton (1983) found that the correlation term $\overline{r_c'' r_r''}$ cannot be neglected in a stratocumulus environment. Both terms $\bar{r}_c \bar{r}_r$ and $\overline{r_c'' r_r''}$ have the same order of magnitude.

The parameterization of nucleation by deposition, nucleation by Brownian collection, nucleation by thermophoresis, nucleation by diffusiophoresis and splintering of ice crystals are the same as described in Section 4. The turbulence contributions to the above mentioned processes are not considered here.

Collection

The parameterization for the mean accretion rate of rain, graupel, aggregates, ice water and ice crystal can be summarized as:

$$\overline{CL}_{ag} = a_{25} \left(\overline{r}_a \overline{r}_g + \overline{r_a'' r_g''} \right) \tag{5.6}$$

$$\overline{CL}_{ca} = a_{31} \left(\overline{r}_c \overline{r}_a + \overline{r_c'' r_a''} \right) \tag{5.7}$$

$$\overline{CL}_{cg} = a_{24} \left(\overline{r}_c \overline{r}_g + \overline{r_c'' r_g''} \right) \tag{5.6}$$

$$\overline{CL}_{ci} = a_{19} \left(\overline{N}_i \overline{r}_c + \overline{N_i'' r_i''} \right) h(T_s) \tag{5.9}$$

$$\overline{CL}_{cr} = a_2 \left(\overline{r}_c \overline{r}_r + \overline{r_c'' r_r''} \right) \tag{5.10}$$

$$\overline{CL}_{ra} = a_{11} \left(\overline{r}_r \overline{r}_a + \overline{r_r'' r_a''} \right) \tag{5.11}$$

$$\overline{CL}_{ri} = a_4 \left(\overline{r}_i \overline{r}_r + \overline{r_i'' r_r''} \right) \tag{5.12}$$

$$\overline{CL}_{rg} = a_5 \left(\overline{r}_r \overline{r}_g + \overline{r_r'' r_g''} \right) \tag{5.13}$$

$$\overline{CL}_{ia} = a_{21} \ (\overline{r_a}\overline{r_i} + \overline{r_a{}''r_i{}''}) \ h(T_s) \tag{5.14}$$

$$\overline{CL}_{ig} = a_{20} \ (\overline{r_i}\overline{r_g} + \overline{r_i{}''z_g{}''}) \ h(T_s) \tag{5.15}$$

Conversion

The mean conversion can be written as:

$$\overline{CN}_{ag} = (a_{26}(\overline{r_c}\overline{r_a} + \overline{r_c{}''r_a{}''}) + a_{27} \ (\overline{r_a}\overline{r_r} + \overline{r_a{}''r_r{}''})) \ h(T_s) \tag{5.16}$$

$$\overline{CN}_{cr} = a_3(\overline{r_c})^{4/3} \ \overline{r_c} \ h(r_c - r_{cm}) \tag{5.17}$$

$$\overline{CN}_{ia} = a_{22}(\overline{N_i}\overline{r_i} + \overline{N_i{}''r_i{}''}) \tag{5.18}$$

$$\overline{CN}_{ig} = (\max(a_{28}(\overline{r_c}\overline{r_i} + \overline{r_c{}''r_i{}''}) - \frac{\overline{N_i}}{\rho_o}C_m,0) + a_{29}(\overline{r_r}\overline{r_i} + \overline{r_r{}''r_i{}''}))h(T_s) \tag{5.19}$$

Melting

The melting rate can be represented by

$$\overline{ML}_{ar} = (a_{12}\bar{r}_a + a_{13}(\bar{r}_a\bar{r}_c + \overline{r_a''r_c''}) + a_{14}(\bar{r}_a\bar{r}_c + \overline{r_a''r_c''}))h(-T_s) \tag{5.20}$$

$$\overline{ML}_{gr} = (a_6\bar{r}_g + a_7(\bar{r}_c\bar{r}_g + \overline{r_c''r_g''}) + a_8(\bar{r}_r\bar{r}_g + \overline{r_r''r_g''}))h(-T_s) \tag{5.21}$$

$$\overline{ML}_{iv} = a_{18}\,\bar{r}_i\,h(-T_s) \tag{5.22}$$

Nucleation

The mean nucleation rate can be summarized as:

$$\overline{NCL}_{ia} = a_{38}(\bar{N}_i\bar{r}_a + \overline{N_i''r_a''}) \tag{5.23}$$

$$\overline{NCL}_{ig} = a_{36}(\bar{r}_g\bar{N}_i + \overline{r_g''N_i''}) \tag{5.24}$$

$$\overline{NCN}_{ia} = a_{37}(\bar{N}_i^2 + \overline{N_i''^2}) \tag{5.25}$$

$$\overline{NCN}_{ig} = (a_{34}(\bar{r}_c\bar{N}_i + \overline{r_c''N_i''}) + a_{35}(\bar{r}_r\bar{N}_i + \overline{r_r''N_i''}))h(-T_s) \tag{5.26}$$

$$\overline{NUA}_{vi} = \frac{m_{io}}{\rho_o}\left[\max\left[w\beta_2 N_{io}\,\exp\,(\beta_2 T_s)\frac{\partial T_s}{\partial z}, 0.\right]\,h(T_s)\right.$$

$$= \frac{CN10}{\rho_o}\,\max\left[\exp(\beta_2 T_s)\,w\frac{\partial T_s}{\partial z}, 0.\right]\,h(T_s) \tag{5.27}$$

$$\overline{NUB}_{vi} = \frac{4\pi R_c N_c n_a m_{io}}{\rho_o} DF_{ar} \, h(T_s)$$

$$= \frac{7.79 \, m_{io} N_c^{2/3}}{\rho_w^{1/3}} \, n_{ao} \, (270.16 - T_c)^{1.3} \left[\frac{r_c}{2 \rho_o}\right]^{1/3} DF_{ar} \, h(T_s)$$

$$= CN11 (270.16 - T_c)^{1.3} \left[\frac{r_c}{2 \rho_o}\right]^{1/3} DF_{ar} \, h(T_s) \tag{5.28}$$

$$\overline{NUC}_{vi} = CN11 (270.16 - T_c)^{1.3} \left[\frac{\overline{r_c}}{2 \rho_o}\right]^{1/3} K \, \frac{\max(T - T_c, 0.)}{10 \, p} \, h(T_s) \tag{5.29}$$

$$\overline{NUD}_{vi} = CN11 (270.16 - T_c)^{1.3} \left[\frac{\overline{r_c}}{2 \rho_o}\right]^{1/3} \frac{.04 R_c (RT)^{1/2}}{\rho_o DF_v} \, G(T,p) \max(SS_1, 0.) h(T_s)$$

$$= CN11 \, CN12 (270.16 - T_c)^{1.3} \left[\frac{r_c}{2 \rho_o}\right]^{1/3} \frac{G(T,p) T^{1/2}}{DF_v} \max(SS_1, 0.) \, h(T_s) \tag{5.30}$$

$$\overline{NML}_{iv} = a_{33} \, \overline{N}_i \tag{5.31}$$

Shedding

The mean shedding terms are:

$$\overline{SH}_{ar} = (a_{15}(\overline{r_a r_c} + \overline{r_a'' r_c''}) + a_{16}(\overline{r_a r_r} + \overline{r_a'' r_r''}))h(-T_s)$$

(5.32)

$$\overline{SH}_{gr} = (a_9(\overline{r_c r_g} + \overline{r_c'' r_g''}) + a_{10}(\overline{r_r r_g} + \overline{r_r'' r_g''}))h(-T_s)$$

(5.33)

Splintering

The mean splintering term is:

$$\overline{SP}_{vi} = \frac{m_{io}}{\rho_o}\left[\beta_5\rho_o + 4 \times 10^{-3}\frac{N_c}{r_c}f_3(m_c)\right]\left[f_1(T_i)CL_{ci} + f_1(T_g)CL_{cg} + f_1(T_a)CL_{ca}\right]$$

(5.34)

where CL_{ci}, CL_{cg} and CL_{ca} are mean accretion terms which can be found in the section on collection.

Vapor deposition

The mean vapor deposition terms are:

$$\overline{VD}_{va} = a_{30}\,\overline{r}_a$$

(5.35)

$$\overline{VD}_{vg} = a_{23}\,\overline{r}_g$$

(5.36)

$$\overline{VD}_{vi} = a_{17}\,\overline{N}_i\,h(T_s)$$

(5.37)

$$\overline{VD}_{vr} = a_1 \, \overline{r}_r \tag{5.38}$$

5.3 Summary of Turbulence Fluxes and Covariances

5.3.1 Introduction

The procedure to derive the formulation for the mean variables, turbulence fluxes and its covariances follows the same methodology as described by Manton and Cotton (1977). Since the introduction of rain, ice, graupel, aggregate and ice crystal in this report, the equations for the turbulence fluxes and covariances are much more complicated than the formulation described by Chen and Cotton (1982, 1983ab). In spite of the complication of the equations, some simple and consistent patterns of equations can be derived. In the next section the terminology for the correlation between various terms is introduced. The summary of the turbulent microphysics is described in a later section.

5.3.2 Terminology

In the equations below many terms have similar structure, but their difference depends upon what variables are taken into account. The perturbation variables are represented by

$$\phi' = \left| u_i{}'', \ r_T{}'', \ \Theta_{il}{}'', \ r_r{}'', \ r_i{}'', \ r_g{}'', \ r_a{}'', \ N_i{}''/\rho_o \right|$$

The variable $r_\gamma{}''$ denotes the perturbation mixing ratios

$$(r_r{}'', \ r_i{}'', \ r_g{}'', \ r_a{}'' \text{ and } \frac{N_i{}''}{\rho_o})$$

The following equations represent the production terms for turbulent fluxes (Equation 5.39) and turbulent covariances (Equation 5.40). The various terms on the right hand side (RHS) of Equation

(5.39) represent: shear production, advection, eddy transport, isotropy redistribution and buoyancy. The terms on the RHS of Equation (5.40) represent: advection, shear productions, eddy transport and dissipation of the covariances.

$$A(r_\gamma{}'') = - \overline{u_j{}''r_\gamma{}''} \frac{\partial}{\partial x_j} \bar{u}_i - \bar{u}_j \frac{\partial}{\partial x_j} \overline{u_i{}''r_j{}''} - \frac{\partial}{\partial x_j} \overline{u_i{}''u_j{}''r_\gamma{}''}$$

$$- \frac{\overline{r_\gamma{}''}}{\rho_o} \frac{\partial}{\partial x_i} p'' - \frac{\overline{\rho''r_\gamma{}''}}{\rho_o} g\delta_{i3} \qquad (5.39)$$

$$B(\phi'',r_\gamma{}'') = - \bar{u}_j \frac{\partial}{\partial x_j} \overline{\phi''r_\gamma{}''} - \overline{r_\gamma{}''u_j{}''} \frac{\partial}{\partial x_j} \bar{\phi}$$

$$- \overline{\phi''u_j{}''} \frac{\partial}{\partial x_j} \overline{r_\gamma{}''} - \frac{\partial}{\partial x_j} \overline{u_j{}''\phi''r_\gamma{}''}$$

$$-2\ \varepsilon(\phi'',r_r{}'')$$

$$(5.40)$$

where $\varepsilon\ (\phi'',\ r_r{}'')$ is the dissipation term which can be parameterized as

$$\varepsilon(\phi'',r_r{}'') = \frac{\overline{\mu\phi''r_r{}''}}{\tau_\theta} \qquad (5.41)$$

where $\mu = 0.31$, τ_θ is defined in Chen and Cotton (1983a).

In the following equations, the turbulent microphysical processes to produce rain, aggregate, graupel, ice and ice crystal are denoted by $R_\mu{}''$, $A_\mu{}''$, $G_\mu{}''$, $I_\mu{}''$, and $IC_\mu{}''$. The mean equations for those processes correlated with other turbulence variable (ϕ'') can be written as

$$\overline{\phi 'R_{\mu}''} = \overline{\phi 'VD_{vr}''} + \overline{\phi 'CL_{cr}''} + \overline{\phi 'CN_{cr}''}$$

$$- \overline{\phi 'CL_{ri}''} - \overline{\phi 'CL_{rg}''} + \overline{\phi 'ML_{gr}''}$$

$$+ \overline{\phi 'SH_{gr}''} - \overline{\phi 'CL_{ra}''} + \overline{\phi 'ML_{ar}''}$$

$$+ \overline{\phi 'SH_{ar}''} \tag{5.42}$$

$$\overline{\phi 'A_{\mu}''} = \overline{\phi 'VD_{va}''} + \overline{\phi 'CL_{ca}''} + \overline{\phi 'CL_{ra}''} - \overline{\phi 'ML_{ar}''}$$

$$- \overline{\phi 'SH_{ar}''} + \overline{\phi 'CL_{ia}''} + \overline{\phi 'CN_{ia}''}$$

$$- \overline{\phi 'CL_{ag}''} - \overline{\phi 'CN_{ag}''} \tag{5.43}$$

$$\overline{\phi 'G_{\mu}''} = \overline{\phi 'VD_{vg}''} + \overline{\phi 'CL_{cg}''} + \overline{\phi 'CL_{rg}''} - \overline{\phi 'ML_{gr}''}$$

$$- \overline{\phi 'SH_{gr}''} + \overline{\phi 'CL_{ig}''} + \overline{\phi 'CN_{ig}''}$$

$$+ \overline{\phi 'CL_{ag}''} - \overline{\phi 'CN_{ag}''} \tag{5.44}$$

$$\overline{\phi 'I_{\mu}''} = \overline{\phi 'VD_{vi}''} - \overline{\phi 'ML_{iv}''} + \overline{\phi 'CL_{ci}''} + \overline{\phi 'CL_{ri}''}$$

$$- \overline{\phi 'CL_{ig}''} - \overline{\phi 'CN_{ig}''} - \overline{\phi 'CL_{ia}''} - \overline{\phi 'CN_{ia}''} \tag{5.45}$$

$$\overline{\phi 'IC_{\mu}''} = \overline{\phi 'NCN_{ig}''} + \overline{\phi 'NCL_{ig}''} + \overline{\phi 'NCN_{ia}''}$$

$$+ \overline{\phi 'NCL_{ia}''} \tag{5.46}$$

5.3.3 Turbulent Microphysics

Turbulent flux of rain water

$$\frac{\partial}{\partial t} \, (\overline{u_i{}''r_r{}''}) = A(r_r{}'') + \overline{u_i{}''R_\mu{}''}$$

$$(5.47)$$

$$\frac{\partial}{\partial t} \, (\overline{r_r{}''^2}) = B(r_r{}'',r_r{}'') + 2 \, \overline{r_r{}''R_\mu{}''}$$

$$(5.48)$$

$$\frac{\partial}{\partial t} \, (\overline{r_T{}''r_r{}''}) = B(r_T{}'',r_r{}'') + \overline{r_T{}''R_\mu{}''}$$

$$(5.49)$$

$$\frac{\partial}{\partial t} \, (\overline{\theta_{il}{}''r_r{}''}) = B(\theta_{il}{}'',r_r{}'') + \overline{\theta_{il}'{}'R_\mu{}''}$$

$$(5.50)$$

$$\frac{\partial}{\partial t} \, (\overline{r_i{}''r_r{}''}) = B(r_i{}'',r_r{}'') + \overline{r_i{}''R_\mu{}''} + \overline{r_r{}''I_\mu{}''}$$

$$(5.51)$$

$$\frac{\partial}{\partial t} \, (\overline{r_g{}''r_r{}''}) = B(r_g{}'',r_r{}'') + \overline{r_g{}''R_\mu{}''} + \overline{r_r{}''G_\mu{}''}$$

$$(5.52)$$

$$\frac{\partial}{\partial t} \, (\overline{r_a{}''r_r{}''}) = B(r_a{}'',r_r{}'') + \overline{r_a{}''R_\mu{}''} + \overline{r_r{}''A_\mu{}''}$$

$$(5.53)$$

$$\frac{\partial}{\partial t} \left[\overline{\frac{N_i{}''r_r{}''}{\rho_o}} \right]) = B(\frac{N_i{}''}{\rho_o}, \, r_r{}'') + \overline{N_i{}''/\rho_o R_\mu{}''} + \overline{r_r{}''IC_\mu{}''}$$

$$(5.54)$$

Turbulent flux of ice water

$$\frac{\partial}{\partial t} \left(\overline{u_i'' r_i''} \right) = A(r_i'') + \overline{u_i'' I_\mu''} \tag{5.55}$$

$$\frac{\partial}{\partial t} \left(\overline{r_T'' r_i''} \right) = B(r_T'', r_i'') + \overline{r_T'' I_\mu''} \tag{5.56}$$

$$\frac{\partial}{\partial t} \left(\overline{\Theta_{il}'' r_i''} \right) = B(\Theta_{il}'', r_i'') + \overline{\Theta_{il}'' I_\mu''} \tag{5.57}$$

$$\frac{\partial}{\partial t} \left(\overline{r_i''^2} \right) = B(r_i'', r_i'') + 2\overline{r_i'' I_\mu''} \tag{5.58}$$

$$\frac{\partial}{\partial t} \left(\overline{r_g'' r_i''} \right) = B(r_g'', r_i'') + \overline{r_g'' I_\mu''} + \overline{r_i'' G_\mu''} \tag{5.59}$$

$$\frac{\partial}{\partial t} \left(\overline{r_a'' r_i''} \right) = B(r_a'', r_i'') + \overline{r_a'' I_\mu''} + \overline{r_i'' A_\mu''} \tag{5.60}$$

$$\frac{\partial}{\partial t} \left[\overline{\frac{N_i'' r_i''}{\rho_o}} \right] = B\left(\frac{N_i''}{\rho_o} , r_i'' \right) + \overline{N_i''/\rho_o I_\mu''} + \overline{r_i'' IC_\mu''} \tag{5.61}$$

Turbulent flux of graupel water

$$\frac{\partial}{\partial t} \left(\overline{u_i'' r_g''} \right) = A(r_g'') + \overline{u_i'' G_\mu''} \tag{5.62}$$

$$\frac{\partial}{\partial t} \left(\overline{r_T'' r_g''} \right) = B(r_T'', r_g'') + \overline{r_T'' G_\mu''} \tag{5.63}$$

$$\frac{\partial}{\partial t} \left(\overline{\Theta_{il}{}''r_g{}''} \right) = B(\Theta_{il}{}'', r_g{}'') + \overline{\Theta_{il}{}''G_\mu{}''}$$

$$(5.64)$$

$$\frac{\partial}{\partial t} \left(\overline{r_g{}''^2} \right) = B(r_g{}'', r_g{}'') + 2\, \overline{r_g{}''G_\mu{}''}$$

$$(5.65)$$

$$\frac{\partial}{\partial t} \left(\overline{r_a{}''r_g{}''} \right) = B(r_a{}'', r_g{}'') + \overline{r_a{}''G_\mu{}''} + \overline{r_g{}''A_\mu{}''}$$

$$(5.66)$$

$$\frac{\partial}{\partial t} \left[\overline{\frac{N_i{}''r_g{}''}{\rho_o}} \right] = B\left(\frac{N_i{}''}{\rho_o}, r_g{}'' \right) + \overline{N_i{}''/\rho_o G_\mu{}''} + \overline{r_g{}''IC_\mu{}''}$$

$$(5.67)$$

Turbulent flux of aggregate water

$$\frac{\partial}{\partial t} \left(\overline{u_i{}''r_a{}''} \right) = A(r_a{}'') + \overline{u_i{}''A_\mu{}''}$$

$$(5.68)$$

$$\frac{\partial}{\partial t} \left(\overline{r_T{}''r_a{}''} \right) = B(r_T{}'', r_a{}'') + \overline{r_T{}''A_\mu{}''}$$

$$(5.69)$$

$$\frac{\partial}{\partial t} \left(\overline{\Theta_{il}{}''r_a{}''} \right) = B(\Theta_{il}{}'', r_a{}'') + \overline{\Theta_{il}{}''A_\mu{}''}$$

$$(5.70)$$

$$\frac{\partial}{\partial t} \left[\overline{\frac{N_i{}''r_a{}''}{\rho_o}} \right] = B\left(\frac{N_i{}''}{\rho_o}, r_a{}'' \right) + \overline{N_i{}''/\rho_o A_\mu{}''} + \overline{r_a{}''IC_\mu{}''}$$

$$(5.71)$$

$$\frac{\partial}{\partial t} \left(\overline{r_a{}''^2} \right) = B(r_a{}'', r_a{}'') + 2\, \overline{r_a{}''A_\mu{}''}$$

$$(5.72)$$

Turbulent flux of ice crystals

$$\frac{\partial}{\partial t}\left[\frac{\overline{u_i{''}N_i{''}}}{\rho_o}\right] = A\left(\frac{N_i{''}}{\rho_o}\right) + \overline{u_i{''}IC_\mu{''}}$$

(5.73)

$$\frac{\partial}{\partial t}\left[\frac{\overline{r_T{''}N_i{''}}}{\rho_o}\right] = B\left(r_T{''}, \frac{N_i{''}}{\rho_o}\right) + \overline{r_T{''}IC_\mu{''}}$$

(5.74)

$$\frac{\partial}{\partial t}\left[\frac{\overline{\Theta_{il}{''}N_i{''}}}{\rho_o{''}}\right] = B\left(\Theta_{il}{''}, \frac{N_i{''}}{\rho_o}\right) + \overline{\Theta_{il}{''}IC_\mu{''}}$$

(5.75)

$$\frac{\partial}{\partial t}\left[\frac{\overline{N_i{''}}}{\rho_o}\right]2 = B\left(\frac{N_i{''}}{\rho_o},\frac{N_i{''}}{\rho_o}\right) + 2\,\overline{N_i{''}/\rho_o IC_\mu{''}}$$

(5.76)

5.3.4 Definitions of Turbulent Microphysics Terms

In this section, the terms on the right hand side of Equations (5.43), (5.44), (5.45), (5.46), and (5.47) are defined according to the following processes: collection, conversion, melting, shedding, and deposition.

Collection

$$\overline{\phi{'}CL_{ag}{''}} = a_{25}\left(\overline{r}_a\,\overline{\phi{''}r_g{''}} + \overline{r}_g\,\overline{\phi{''}r_a{''}} + \overline{\phi{''}r_g{''}r_a{''}}\right)$$

(5.77)

$$\overline{\phi' CL_{ca}''} = a_{31}(\overline{r}_c \ \overline{\phi'' r_a''} + \overline{r}_a \ \overline{\phi'' r_c''} + \overline{\phi'' r_a'' r_c''}) \tag{5.78}$$

$$\overline{\phi' CL_{cg}''} = a_{24}(\overline{r}_c \ \overline{\phi'' r_g''} + \overline{r}_g \ \overline{\phi'' r_c''} + \overline{\phi'' r_g'' r_c''}) \tag{5.79}$$

$$\overline{\phi' CL_{ci}''} = a_{19}(\overline{N}_i \ \overline{\phi'' r_c''} + \overline{r}_c \ \overline{\phi'' N_i''} + \overline{\phi'' N_i'' r_c''}) h(T_s) \tag{5.80}$$

$$\overline{\phi' CL_{cr}''} = a_2(\overline{r}_c \ \overline{\phi'' r_r''} + \overline{r}_r \ \overline{\phi'' r_c''} + \overline{\phi'' r_r'' r_c''}) \tag{5.81}$$

$$\overline{\phi' CL_{ia}''} = a_{21}(\overline{r}_a \ \overline{\phi'' r_i''} + \overline{r}_i \ \overline{\phi'' r_a''} + \overline{\phi'' r_i'' r_a''}) h(T_s) \tag{5.82}$$

$$\overline{\phi' CL_{ig}''} = a_{20}(\overline{r}_i \ \overline{\phi'' r_g''} + \overline{r}_g \ \overline{\phi'' r_i''} + \overline{\phi'' r_g'' r_i''}) h(T_s) \tag{5.83}$$

$$\overline{\phi' CL_{ra}''} = a_{11}(\overline{r}_r \ \overline{\phi'' r_a''} + \overline{r}_a \ \overline{\phi'' r_r''} + \overline{\phi'' r_a'' r_r''}) \tag{5.84}$$

$$\overline{\phi' CL_{ri}''} = a_4(\overline{r}_i \ \overline{\phi'' r_r''} + \overline{r}_r \ \overline{\phi'' r_i''} + \overline{\phi'' r_i'' r_r''}) \tag{5.85}$$

$$\overline{\phi' CL_{rg}''} = a_5(\overline{r}_r \ \overline{\phi'' r_g''} + \overline{r}_g \ \overline{\phi'' r_r''} + \overline{\phi'' r_g'' r_r''}) \tag{5.86}$$

Conversion

$$\overline{\phi' CN_{ag}''} = (a_{26}(\overline{r}_c \ \overline{\phi'' r_a''} + \overline{r}_a \ \overline{\phi'' r_c''} + \overline{\phi'' r_a'' r_c''})$$
$$+ a_{27}(\overline{r}_a \ \overline{\phi'' r_r''} + \overline{r}_r \ \overline{\phi'' r_a''} + \overline{\phi'' r_r'' r_a''})) h(T_s) \tag{5.87}$$

$$\overline{\phi'CN''_{cr}} = a_3 \, \overline{r}_c^{4/3} \, \overline{\phi''r_c''} \, h(r_c - r_{cm}) \qquad (5.88)$$

$$\overline{\phi'CN''_{ia}} = a_{22}(\overline{N}_i \, \overline{\phi''r_i''} + \overline{r}_i \, \overline{\phi''N_i''} + \overline{\phi''N_i''r_i''}) \qquad (5.89)$$

$$\overline{\phi'CN''_{ig}} = (max(a_{28}(\overline{r}_c \, \overline{\phi''r_i''} + \overline{r}_i \, \overline{\phi''r_c''} + \overline{\phi''r_i''r_c''}) - \frac{\overline{\phi''N_i''}}{\rho_o} c_m, 0)$$
$$+ a_{29}(\overline{r}_r \, \overline{\phi''r_i''} + \overline{r}_i \, \overline{\phi''r_r''} + \overline{\phi''r_i''r_r''}))h(T_s) \qquad (5.90)$$

Melting

$$\overline{\phi'ML''_{ar}} = (a_{12}\overline{\phi''r_a''} + a_{13}(\overline{r}_a \, \overline{\phi''r_c''} + \overline{r}_c\overline{\phi''r_a''} + \overline{\phi''r_a''r_c''})$$
$$+ a_{14}(\overline{r}_a \, \overline{\phi''r_c''} + \overline{r}_c \, \overline{\phi''r_a''} + \overline{\phi''r_c''r_a''}))h(-T_s) \qquad (5.91)$$

$$\overline{\phi'ML''_{gr}} = (a_6\overline{\phi''r_g''} + a_7(\overline{r}_c \, \overline{\phi''r_g''} + \overline{r}_g\phi''r_c'' + \overline{\phi''r_g''r_c''})$$
$$+ a_8(\overline{r}_r \, \overline{\phi''r_g''} + \overline{r}_g \, \overline{\phi''r_r''} + \overline{\phi''r_r''r_g''}))h(-T_s) \qquad (5.92)$$

$$\overline{\phi'ML''_{iv}} = a_{18} \, \overline{\phi''r_i''} \, h(-T_s) \qquad (5.93)$$

$$\overline{\phi'CL''_{ci}} = a_{19}(\overline{N}_i \, \overline{\phi''r_c''} + \overline{r}_c \, \overline{\phi''N_i''} + \overline{\phi''N_i''r_c''})h(T_s) \qquad (5.94)$$

$$\overline{\phi'NCL''_{ia}} = a_{38}(\overline{N}_i \, \overline{\phi''r_a''} + \overline{r}_a \, \overline{\phi''N_i''} + \overline{\phi''r_a''N_i''}) \qquad (5.95)$$

$$\overline{\phi'NCL''_{ig}} = a_{36}(\overline{r}_g \ \overline{\phi''N_i''} + \overline{N}_i \ \overline{\phi''r_g''} + \overline{\phi''N_i''r_g''})$$

(5.96)

$$\overline{\phi'NCN''_{ia}} = a_{37} \ (2 \ \overline{N}_i \ \overline{\phi''N_i''} + \overline{\phi''N_i^2})$$

(5.97)

$$\overline{\phi'NCN''_{ig}} = (a_{34}(\overline{r}_c \ \overline{\phi''N_i''} + \overline{N}_i \ \overline{\phi''r_c''} + \overline{\phi''N_i''r_c''})$$

$$+ a_{35}(\overline{r}_r \ \overline{\phi''N_i''} + \overline{N}_i \ \overline{\phi''r_r''} + \overline{\phi''N_i''r_r''}))h(-T_s)$$

(5.98)

$$\overline{\phi'NML''_{ar}} = a_{33} \ \overline{\phi''N_i''}$$

(5.99)

Shedding

$$\overline{\phi'SH''_{ar}} = (a_{15}(\overline{r}_a \ \overline{\phi''r_c''} + \overline{r}_c \ \overline{\phi''r_a''} + \overline{\phi''r_c''r_a''})$$

$$+ a_{16}(\overline{r}_a \ \overline{\phi''r_r''} + \overline{r}_r \ \overline{\phi''r_a''} + \overline{\phi''r_a''r_r''}))h(-T_s)$$

(5.100)

$$\overline{\phi'SH''_{gr}} = (a_9(\overline{r}_c \ \overline{\phi''r_g''} + \overline{r}_g \ \overline{\phi''r_c''} + \overline{\phi''r_g''r_c''})$$

$$= a_{10}(\overline{r}_r \ \overline{\phi''r_g''} + \overline{r}_g \ \overline{\phi''r_r''} + \overline{\phi''r_g''r_r''}))h(-T_s)$$

(5.101)

Splintering

Not parameterized

Vapor deposition

$$\overline{\phi'VD''_{va}} = a_{30} \overline{\phi''r''_a}$$

(5.102)

$$\overline{\phi'VD''_{vi}} = a_{17} \overline{\phi''N''_i} \, h(T_s)$$

(5.103)

$$\overline{\phi'VD''_{vg}} = a_{23} \overline{\phi''r''_g}$$

(5.104)

$$\overline{\phi'VD''_{vr}} = a_1 \overline{\phi''r''_r}$$

(5.105)

Nucleation by deposition, Brownian collection thermophoresis, diffusiophoresis

Since very little is known, especially for the turbulence contribution to the nucleation process by deposition, Brownian collection, thermophoresis and diffusiophoresis is the incorporation of turbulent fluctuations in the parameterization processes would be meaningless. Thus, the parameterization for the turbulent related nucleation is not proposed in this report.

APPENDIX

Summary of coefficients

$$a_1 = (CN1 + CN2 \ (\rho_o^{1/2} T745I)^{1/2}) SS_1 . G(T,P)$$

$$a_2 = CN4 \ E_{cr} \ \rho_o^{1/2}$$

$$a_3 = CN3 \ \rho_o^{4/3} \ T745I$$

$$a_4 = CN5 \ \rho_o \ |\bar{v}_r - \bar{v}_i|$$

$$a_5 = 1.57 |\bar{v}_r - \bar{v}_g| (CN18 + CN19 \ D_{gm} + D_{gm}^2) \rho_o / (\pi \rho_g D_{gm}^3)$$

$$a_6 = \frac{k'_{3g}}{L_{i\ell}} (-KT_s + DF_v L_{iv} \rho_o (\bar{r}_r - r_{s1}(T_f)))$$

$$k'_{3g} = \left[4.3(\pi^2 \rho_g^3 D_{gm}^6)^{-1/3} + CN37 \left[T745I \left[\frac{\pi \rho_g D_{gm}^3}{\rho_o} \right] \right]^{1/4} \left[\frac{\rho_o^3}{\pi^4 \rho_g^6 D_{gm}^{12}} \right]^{1/6} \right]$$

$$a_7 = \frac{-c_w T_s}{L_{i1}} a_{24}$$

$$a_8 = \frac{-c_w T_s}{L_{i1}} a_5$$

$$a_9 = a_{24}$$

$$a_{10} = a_5$$

$$a_{11} = CN34 \rho_o |\bar{v}_a - \bar{v}_r|$$

$$a_{12} = CN22 f_2 (Re_a)(-kT_s + L_{iv} DF_v \rho_o (\bar{r}_r - r_{s1}(T_f)))$$

$$a_{13} = -CN35 \ T_s \ a_{31}$$

$$a_{14} = -CN35 \ T_s \ a_{11}$$

$$a_{15} = a_{31}$$

$$a_{16} = a_{11}$$

$$a_{17} = (\frac{1}{\rho_o}(4D_i SS_i f_2(Re_i)) - \min\left[\max \frac{1}{\rho_o}(4D_i SS_i f_2(Re_i), 0.), \frac{CN39CL_{ci}}{kT^2 N_i}\right] G(T,P)$$

$$a_{18} = \frac{1}{\Delta t}$$

$$a_{19} = .79\bar{v}_i \ D_i^2 \ E_{ci}$$

$$a_{20} = 1.1 \ \bar{E}(T_g) |\bar{v}_i - \bar{v}_g| \ \left[\frac{1}{\pi \ D_{gm}^3}\right]^{1/3} \left[\frac{\rho_o}{\rho_g}\right]$$

$$a_{21} = CN7 \ \bar{E}(T_a) |\bar{v}_a - \bar{v}_i| \rho_o (CN8 + CN9D_i + D_i^2)$$

$$a_{22} = 0.056 \ D_i^2 v_i \ E(T_i)$$

$$a_{23} = SS_i G(T,P) k'_{3g}$$

$$a_{24} = CN38 \ E_{cg} \ \rho_o^{1/2}$$

$$a_{25} = 1.57 \ \bar{E}(\max(T_a, T_g)) |\bar{v}_a - \bar{v}_g| (CN15 - CN16D_{gm} + D_{gm}^2) \frac{\rho_o}{\pi \rho_g D_{gm}^3}$$

$$a_{26} = [\max(a_{31} - CN14 \ \rho_o^{1/2}, 0.)]$$

$$a_{27} = CN17 \ \rho_o |\bar{v}_a - \bar{v}_r| + a_{11}$$

$$a_{28} = a_{19}$$

$$a_{29} = a_4$$

$$a_{30} = \text{CN20 } G(T,P)f_2(\text{Re}_a)SS_i$$

$$a_{31} = \text{CN21 } E_{ac}\ \rho_o^{1/2}$$

$$a_{33} = \rho_o^{-1}a_{18}\ h(T_s)$$

$$a_{34} = \rho_o^{-1}a_{28}$$

$$a_{35} = \rho_o^{-1}a_4$$

$$a_{36} = \rho_o^{-1}a_{20}\ h(T_s)$$

$$a_{37} = \rho_o^{-1}a_{22}$$

$$a_{38} = \rho_o^{-1}a_{21}\ h(T_s)$$

5.4 Simplified 1D Cloud/Turbulence Model

As one can readily see, expansion of the higher-ordered turbulence model to the ice-phase results in an extremely complex system of equations. Application of this system to a one-dimensional model has possibilities, but the extension to the 2D/3D flow model appears hopeless. We have, therefore, decided to develop a simpler "hybrid" version of Chen and Cotton's (1983b) cloud/turbulence model. Following Mellor and Yamada's (1974) terminology we will refer to Chen and Cotton's model as a level 3.5 turbulence model with the new form called a level 2.5 model. The objective is to develop a turbulence model in which the number of prognostic variables is greatly reduced, yet essential features of the level 3.5 model, such as cloud fractional coverage and entrainment rates are properly predicted. The level 2.5 model will be tested and developed against the level 3.5 model, first in dry ABL applications and then a liquid-phase-only cloudy ABL. After we

have decided we have a satisfactory "compromise" model, it will then be extended to the ice-phase system described in the previous sections.

The proposed level 2.5 model has three prognostic equations $(q^2, \overline{a''^2})$ and diagnostic equations for the remaining turbulence variables. The diagnostic equations compute $\overline{u_i''}$, $\overline{u_j''a''}$, and $\overline{a''b''}$. In the derivation of diagnostic equations, we assume no time derivative, no vertical divergence of the third order term and the dissipation of the turbulence energy (ε) is balanced by shear production (P_s) and buoyancy production (P_b) of the turbulence energy. The summary of equations for the level 2.5 model is given as follows:

$$\frac{\partial}{\partial t}q^2 = -\frac{\partial}{\partial z}(\overline{u''^2 w'} + \overline{v''^2 w'} + \overline{w'^3} + 2\frac{1}{\rho_0}\overline{p'w'})$$

$$+ 2(P_s + P_b - \varepsilon) \tag{5.106}$$

where

$$P_s = -\overline{u'w'}\frac{\partial}{\partial z}\overline{u} - \overline{v'w'}\frac{\partial}{\partial z}\overline{v} \tag{5.107}$$

$$P_b = -R_1\overline{w'\theta_{i1}''} - R_2\overline{w'r'} \tag{5.108}$$

$$\varepsilon = \mu\, q^2/\tau \tag{5.109}$$

$$\overline{u''^2} = \frac{1}{3}q^2 + \frac{\tau}{c_1}[-\frac{4}{3}\overline{u'w'}\frac{\partial}{\partial z}\overline{u} + \frac{2}{3}\overline{v'w'}\frac{\partial}{\partial z}\overline{v} - \frac{2}{3}P_b] \tag{5.110}$$

$$\overline{v'^2} = \frac{1}{3} q^2 + \frac{\tau}{c_1} [-\frac{2}{3} \overline{u''w''} \frac{\partial}{\partial z} \bar{u} + \frac{4}{3} \overline{v'w''} \frac{\partial}{\partial z} \bar{v} - \frac{2}{3} P_b] \quad \cdot (5.111)$$

$$\overline{w'^2} = \frac{1}{3} q^2 + \frac{\tau}{c_1} [-\frac{2}{3} \overline{u''w''} \frac{\partial}{\partial z} \bar{u} + \frac{2}{3} \overline{v'w''} \frac{\partial}{\partial z} \bar{v} - \frac{4}{3} P_b] \quad \cdot (5.112)$$

$$\overline{u_i'w''} = \frac{\tau}{c_1} [-\overline{w'^2} \frac{\partial}{\partial z} \bar{u}_i - R_1 \overline{u_i''\Theta_{i1}''} - R_2 \overline{u_i''r''}] \quad i=1,2 \quad (5.113)$$

$$\overline{u_i'\Theta_{i1}''} = \frac{\tau}{c_\theta} [-\overline{u_2'w''} \frac{\partial}{\partial z} \bar{\Theta}_{i1} - \overline{w'\Theta_{i1}''} \frac{\partial}{\partial z} \bar{u}_i] \quad ; \quad i=1,2 \quad (5.114)$$

$$\overline{u_i''r_T''} = \frac{\tau}{c_\theta} [-\overline{u_i''w''} \frac{\partial}{\partial z} \bar{r}_T - \overline{w'r_T''} \frac{\partial}{\partial z} \bar{u}_i] \quad ; \quad i=1,2 \quad (5.115)$$

$$\overline{w'\Theta_{i1}''} = \frac{\tau}{c_\theta} [-\overline{w'^2} \frac{\partial}{\partial z} \bar{\Theta}_{i1} - R_1 \overline{\Theta_{i1}''^2} - R_2 \overline{\Theta_{i1}''r_T''}] \quad (5.116)$$

$$\overline{\Theta_{i1}''r_T''} = - \frac{\tau_\theta}{2\mu} [\overline{w'\Theta_{i1}''} \frac{\partial}{\partial z} \bar{r}_T + \overline{w'r_T''} \frac{\partial}{\partial z} \bar{\Theta}_{i1}] . \quad (5.117)$$

In order to solve Equations (5.110) to (5.117), we can define

$$\overline{u''w''} \approx - K_M \frac{\partial}{\partial z} \bar{u} \quad (5.118)$$

$$\overline{v'w''} \approx - K_M \frac{\partial}{\partial z} \bar{v} \quad (5.119)$$

$$\overline{w'\Theta_{i1}''} = - K_H \frac{\partial}{\partial z} \bar{\Theta}_{i1} \quad (5.120)$$

$$\overline{w''r_T''} = - K_H \frac{\partial}{\partial z} \overline{r}_T \qquad (5.121)$$

Substitution of Equations (5.120) and (5.121) into Equation (5.117) and (5.108) results in

$$\overline{\theta_{il}''r_T''} = B \; K_H \frac{\partial}{\partial z} \overline{\theta}_{il} \qquad (5.122)$$

$$P_b = C \; K_H \qquad (5.123)$$

where

$$B = \frac{\tau_\theta}{\mu} \frac{\partial}{\partial z} \overline{r} \qquad (5.124)$$

$$C = (R_1 \frac{\partial}{\partial z} \overline{\theta}_{il} + R_2 \frac{\partial}{\partial z} \overline{r}_T) \qquad (5.126)$$

Substitution of Equations (5.118), (5.119) and (5.123) into Equation (5.112) results in

$$\overline{w''^2} = \frac{1}{3} q^2 + D \; K_M + E \; K_H \qquad (5.126)$$

where

$$D = - \frac{2\tau}{3c_1} ((\frac{\partial}{\partial z} \overline{u})^2 + (\frac{\partial}{\partial z} \overline{v})^2) \qquad (5.127)$$

$$E = \frac{4}{3} \frac{\tau}{c_1} C \qquad (5.128)$$

Substitution of Equations (5.126), (5.121) and (5.122) into Equation

(5.116) results in

$$\overline{w''\Theta''_{i1}} = - K_H \frac{\partial}{\partial z} \overline{\Theta}_{i1} \tag{5.129}$$

$$= \frac{\tau}{c_\Theta} [-(\frac{1}{3} q^2 + D K_M + E K_H) \frac{\partial}{\partial z}\overline{\Theta}_{i1} - R_1 \overline{\Theta_{i1}}^2 - R_2 B K_H \frac{\partial}{\partial z} \overline{\Theta}_{i1}].$$

Equation (5.130) can be reduced to

$$K_H = \frac{\tau}{c_\Theta} [(\frac{1}{3} q^2 + D K_M + E K_H) + R_1 A + R_2 B K_H] \tag{5.130}$$

where

$$A = \overline{\Theta''^2_{i1}}/(\frac{\partial}{\partial z} \overline{\Theta}_{i1}) \tag{5.131}$$

Substitution of Equations (5.118), (5.119), (5.120) and (5.121) into
Equations (5.114) and (5.115) results in

$$\overline{u''_i\Theta''_{i1}} = F(K_M + K_H) \frac{\partial}{\partial z} \overline{u}_i \tag{5.132}$$

$$\overline{u''_i r''_T} = G(K_M + K_H) \frac{\partial}{\partial z} \overline{u}_i \tag{5.133}$$

where

$$F = \frac{\tau}{c_\Theta} \frac{\partial}{\partial z} \overline{\Theta}_{i1} \tag{5.134}$$

$$G = \frac{\tau}{c_\Theta} \frac{\partial}{\partial z} \overline{r}_T \tag{5.135}$$

Substitution of Equations (5.126), (5.132) and (5.133) into Equation (5.113) results in

$$\overline{u_i''w'} = - K_M \frac{\partial}{\partial z} \overline{u}_i$$

$$= \frac{\tau}{c_1}[-(\frac{1}{3} q^2 + D K_M + E K_H) \frac{\partial}{\partial z} \overline{u}_i - R_1 F(K_M + K_H) \frac{\partial}{\partial z} \overline{u}_i$$

$$- R_2 G(K_M + K_H) \frac{\partial}{\partial z} \overline{u}_i \tag{5.136}$$

Equation (5.136) can be reduced to

$$K_M = \frac{\tau}{c_1}[(\frac{1}{3} q^2 + D K_M + E K_H) + R_1 F(K_M + K_H)$$

$$+ R_2 G (K_M + K_H)] \tag{5.137}$$

We can obtain K_M and K_H by solving Equations (5.130) and (5.137).

5.5 The Parameterization of Dissipation and the Turbulence Time Scale

As mentioned before, $\overline{\varepsilon}$, $\overline{\varepsilon}_{\theta\theta}$, $\overline{\varepsilon}_{\theta r}$ represent the mean rates of turbulence energy dissipation, destruction of $\overline{\theta_{i1}''^2}$, $\overline{r_T''^2}$, and $\overline{\theta_{i1}''r_T''}$ respectively. Various ways can be found in the literature to parameterize those dissipation and destruction terms. For example, Zeman and Lumley (1976) use prognostic equations, while Andre et al. (1977) and Sun and Ogura (1980) try to diagnose those terms. Both Andre and Sun and Ogura approach the above problems by adopting Blackadar's (1962) length scale which is very popular and is employed by many authors. The advantage of using Blackadar's length scale (shown by Eq. 5.143) is its simplicity. Blackadar's length scale tells us the

mixing length near the surface is proportional to kz, where k is the Von-Karman's constant. This mixing length can be derived from the similarity theory. As in the well mixed layer, Blackadar's length scale converges to a constant mixing length which is around 50 m ~ 60 m. The disadvantage in using Blackadar's length scale is that it may not be appropriate to apply it to a cloud layer. The reason can be explained as follows: The release of latent heat due to the condensation or the convective instability created by the cloud top radiation cooling and the cloud base radiation warming may be accompanied by the production of turbulence kinetic energy (TKE). Ususally, the dissipation of TKE should respond very quickly to the production of TKE. Therefore, Blackadar's length scale can not function well in this instance.

Therefore, a new scheme to diagnose a turbulence length scale is proposed in this study. This new scheme not only contains Blackadar's length scale, which is valid in the unstable ABL, but also can deal with an unstable cloud layer as well.

This new turbulence length scale is defined by

$$\frac{1}{L} = \frac{1}{L_s} + \frac{1}{L_{us}}$$

(5.138)

where

$$\frac{1}{L_s} = \begin{bmatrix} 0 & ; & \text{if} & \frac{\partial \overline{\theta}_{il}}{\partial z} \leq 0 \\ \\ \frac{1}{L_D} & ; & \text{if} & \frac{\partial \overline{\theta}_{il}}{\partial z} > 0 \end{bmatrix}$$

(5.139)

$$L_D = .75 \left[\frac{q^2}{2} / (-R_1 \frac{\partial}{\partial z} \bar{\theta}_{i1}) \right]^{\frac{1}{2}} \tag{5.140}$$

$$\frac{1}{L_{us}} = \max(\frac{1}{L_B}, \frac{1}{L_C}) \tag{5.141}$$

$$\frac{1}{L_c} = \begin{vmatrix} 0 & ; \text{ if } B \leq 0 \\ \dfrac{c_1 q^3}{(0.6 \sqrt{8B})} & ; \text{ if } B > 0 \end{vmatrix} \tag{5.142}$$

$$L_B = kz/(1 + kz/\Delta z) \tag{5.143}$$

$$B = -(R_1 \overline{w''\theta''_{i1}} + R_2 \overline{w''r''_T} + R_2 \overline{w''r''_L}) \tag{5.144}$$

$$c_1 = .102$$

The length scale L_D represents the turbulence length scale for the stable stratified layer. The Blackadar's length scale is denoted by L_B. The buoyancy production of turbulence kinetic energy is defined by Eq. (5.144). We define Eq. (5.142) based on the fact that the buoyancy production of turbulence kinetic energy (B) is always a dominant term. Dissipation therefore should always adjust to B. Eq. (5.142), indicated that the dissipation is about 60% of B. Kaimal et al. (1976) found that the mid-layer dissipation rate is about 0.4 -0.5times the buoyant production rate.

Three types of turbulence time scales (τ, τ_θ, τ_3) have been discussed. These are defined by

$$\tau = \frac{\mu \sqrt{8} \, L}{c_1 q} \qquad (5.145)$$

$$\tau_\theta = 0.5 \, \tau \qquad (5.146)$$

$$\tau_3 = \tau/3 . \qquad (5.147)$$

Eq. (5.146) is defined by assuming that τ_θ/τ is about .5 as discussed by Zeman and Lumley (1976).

5.6 Summary

The scheme for the level 2.5 turbulence model is summarized in this report. We hope to implement this scheme into the 1D version of the CSU cloud/mesoscale model in the near future.

Because of the various options of the CSU cloud/mesoscale model, we have presented an example to show the relationship between the 1D and 3D model code. The newly formulated scheme and coefficients can be tested in the 1D code and then applied to the 3D code. This interaction between the 1D code and the 3D code can be very crucial for the future development of the 3D model.

6.0 Expansion of the 3D Cloud/Mesoscale Model into a Hydrostatic Mesoscale Model

A hydrostatic option has been successfully implemented in the non-hydrostatic 3D cloud/mesoscale model (Tripoli and Cotton, 1982; hereafter referred to as TC). It provides greater computational efficiency on large scale simulations ($\Delta x \geq 10$ km). Since it is an option to the cloud/mesoscale model, most of the numerical formulations are the same as described in TC. The differences will be detailed in the following sections.

6.1 Features of the Hydrostatic Model

Most aspects of the model described in TC are the same including the coordinate system, thermodynamics, microphysics, advective operators, turbulence parameterization and lateral and bottom boundary conditions. The only differences arise in the pressure and vertical velocity computations. Vertical velocity may be diagnosed with a choice of the incompressible, anelastic, or compressible continuity equations. A compressible or incompressible version of the hydrostatic option is available with the compressible version formulated in a "time-split" mode. This allows for a factor of 2-3 increase in computational efficiency.

6.1.1 Vertical Velocity Diagnosis

The vertical velocity may be diagnosed with a choice of the 1) incompressible, 2) anelastic, or 3) compressible continuity equations. (All notation after TC.)

1) incompressible continuity equation

$$\frac{\partial w}{\partial z} = -\frac{\partial u}{\partial x} - \frac{\partial v}{\partial y} \tag{6.1}$$

2) anelastic continuity equation

$$\frac{\partial \rho_o w}{\partial z} = - \frac{\partial \rho_o u}{\partial x} - \frac{\partial \rho_o v}{\partial y} \tag{6.2}$$

3) compressible continuity equation

$$\frac{\partial \rho_o w}{\partial z} = - \frac{\partial \rho_o u}{\partial x} - \frac{\partial \rho_o v}{\partial y} - \frac{\partial \rho}{\partial t} \tag{6.3}$$

To diagnose the compressible term ρ is substituted from the hydrostatic equation and the last term becomes:

$$\frac{1}{g} \frac{\partial}{\partial z}(\frac{\partial p}{\partial t}) \tag{6.4}$$

To compute $\partial p/\partial t$, p is substituted from the integrated form of the hydrostatic equation $p_k = p_{k-1} \exp (\frac{-g\Delta z}{R\bar{T}})$ where the subscript k denotes a vertical level and the overbar represents a vertical layer average from k to $k-1$. The partial derivative $(\partial/\partial t)$ is taken to obtain the expression:

$$\frac{\partial p_k}{\partial t} = \exp(\frac{-g\Delta z}{R\bar{T}}) \frac{\partial p_{k-1}}{\partial t} + p_k \frac{g\Delta z}{R\bar{T}^2} \frac{\partial \bar{T}}{\partial t} \tag{6.5}$$

From Poisson's equation:

$$\frac{\partial \bar{T}}{\partial t} = \frac{T}{\theta} \frac{\partial \theta}{\partial t} + \frac{KT}{p} \frac{\partial p}{\partial t} \tag{6.6}$$

where $K = \frac{R}{C_p}$

Substituting Eq. (6.6) into (6.5) and decomposing the averages yields the expression for $\frac{\partial p}{\partial t}$:

$$\frac{\partial p_k}{\partial t} = \frac{\dfrac{\partial p_{k-1}}{\partial t}\left[\dfrac{p_k}{p_{k-1}}\left(1 + \dfrac{Kg\Lambda z T_{k-1}}{2R\overline{T}^2}\right)\right] + \dfrac{p_k g\Delta z}{2R\overline{T}^2}\left(\dfrac{T_k}{\Theta_k}\dfrac{\partial\Theta_{k-1}}{\partial t} + \dfrac{T_{k-1}}{\Theta_{k-1}}\dfrac{\partial\Theta_{k-1}}{\partial t}\right)}{1 - \dfrac{Kg\Delta z T_k}{2R\overline{T}^2}} \tag{6.7}$$

To close this equation, the pressure tendency at the ground (compressible version) or a time difference of the perturbation pressure at the model top (incompressible version) is computed. These will be described below. The potential temperature tendency is computed from $\partial\Theta_{i1}/\partial t$ of the current time step.

6.1.2 The Compressible Hydrostatic Model

Aside from the vertical velocity diagnosis, compressibility can enter a hydrostatic model in Cartesian coordinates through the form of the boundary condition for the hydrostatic equation. This is the case for the compressible hydrostatic version. The pressure boundary condition is a prognostic surface pressure derived from the substitution of the hydrostatic equation into the compressible continuity equation.

$$\frac{\partial}{\partial z}\left(\frac{\partial p}{\partial t}\right) = g\,\frac{\partial\rho_0 u_i}{\partial x_i} \tag{6.8}$$

Integrating from the ground (z_g) to the height where $p = 0$ (z_p) and assuming the boundary condition that $\partial p/\partial t = 0$ at $p = 0$.

$$\frac{\partial p_s}{\partial t} = -g\int_{z_g}^{z_p}\left[\frac{\partial\rho_0 u}{\partial x} + \frac{\partial\rho_0 u}{\partial y}\right]dz \tag{6.9}$$

Since it is obviously not possible to extend a Cartesian model to p = 0, a one-layer "sigma-p" model is attached to the top of the

Cartesian model. This provides the required divergence which is assumed to apply from the top of the Cartesian model (z_T) to $p = 0$. The surface pressure tendency equation then becomes:

$$\frac{\partial p_s}{\partial t} = - g \int_{z_g}^{z_T} \left[\frac{\partial \rho_0 u}{\partial x} + \frac{\partial p_0 u}{\partial y} \right] dz$$

$$- g \int_1^0 \left[\frac{\partial p_* u}{\partial x} + \frac{\partial p_* v}{\partial y} \right] d\sigma \qquad (6.10)$$

where $\sigma = p/p_*$ and p_* is the pressure at the base of the σ_p layer.

The σ_p layer is configured as follows: The horizontal stagger of the variables is identical to the main model. In the vertical, p_* and $\dot\sigma$ are defined at $\sigma = 1$, while u, v, θ, and z are defined at $\sigma = .5$. The top boundary condition is $\dot\sigma = 0$ at $\sigma = 0$. The equations which govern the σ_p layer are:

$$\frac{\partial u}{\partial t} = - u \frac{\partial u}{\partial x} - v \frac{\partial u}{\partial y} - \dot\sigma \frac{\partial u}{\partial \sigma} + fv - \frac{RT}{p_*} \frac{\partial p_*}{\partial x} - g \frac{\partial z}{\partial x} + K(\frac{\partial^2 u}{\partial x^2} + \frac{\partial^2 u}{\partial y^2}) \qquad (6.11)$$

$$\frac{\partial v}{\partial t} = - u \frac{\partial u}{\partial x} - v \frac{\partial v}{\partial y} - \dot\sigma \frac{\partial u}{\partial T} - fu - \frac{RT}{p_*} \frac{\partial p_*}{\partial y} - g \frac{\partial z}{\partial x} + K(\frac{\partial^2 v}{\partial y^2} + \frac{\partial^2 v}{\partial y^2}) \qquad (6.12)$$

$$\frac{\partial \theta}{\partial t} = - u \frac{\partial \theta}{\partial x} - v \frac{\partial \theta}{\partial y} - \dot\sigma \frac{\partial \theta}{\partial \sigma} + K (\frac{\partial^2 \theta}{\partial x^2} + \frac{\partial^2 \theta}{\partial y^2}) \qquad (6.13)$$

$$\frac{\partial z}{\partial \sigma} = - \frac{RT}{g\sigma} \qquad (6.14)$$

$$\dot{\sigma}_{\sigma=1} = w_{z_T} \, g/(p_* \alpha_*)$$

$$(6.15)$$

$$p_* = P_{z_T}$$

$$(6.16)$$

Note that since p_* is given by the hydrostatic integration from the ground, the continuity equation for the σ_p model is not required.

One of the major advantages of the compressible model is that mass is implicitly conserved since, in a hydrostatic model, mass is directly related to pressure. However, the price that is paid is in slower execution time since the time step is limited by the stability criterion for the Lamb wave, which travels at the speed of sound. Therefore, the compressible version has been formulated in a time-split mode similar to TC which splits the Lamb wave and part of the external gravity wave onto the small time step. A summary of the computational procedure for the time split mode follows:

1) All tendency terms for the prognostic variables except for the horizontal pressure and geopotential gradients and $\dot{\sigma} \, \partial\theta/\partial\sigma$ are computed over the interval $t - \Delta t_L$ to $t + \Delta t_L$.

2) The horizontal velocities at $t - \Delta t_L$ are stepped forward to $t - \Delta t_L + \Delta t_s$ with the horizontal pressure and geopotential gradients and large time step tendencies. θ at $\sigma = .5$ is stepped forward with $\dot{\sigma} \frac{\partial\theta}{\partial\sigma}$.

3) The vertical velocity is calculated and the surface pressure at $t - \Delta t_L + \Delta t_s$ is evaluated in a backward step with horizontal velocities at $t - \Delta t_L + \Delta t_s$.

4) The pressure profile (which is constant over the small time

steps at time t since Θ has no component on the small time step) is shifted by the boundary condition.

5) Steps 2-4 are repeated up to $t + \Delta t_L$.

This procedure effectively isolates the Lamb wave on the small time step and also the portion of the external gravity wave which is produced by the σ_p layer. The execution time for a compressible hydrostatic run can be reduced by a factor of 2 or 3 by this technique.

6.1.3 The Incompressible Hydrostatic Model

The incompressible hydrostatic model uses the internal gravity wave radiation boundary condition of Klemp and Durran (1983). This condition is derived from the linear, Boussinesq hydrostatic irrotational equations. By transforming these equations to wave space and allowing only upward propagating solutions, a boundary condition is derived.

$$p' = \frac{N\alpha_0}{|k|} w \qquad (6.17)$$

where p' and w are the Fourier coefficients of p' and w, k is the horizontal wavenumber and N is the Brunt-Vaisala frequency. In practice, the horizontal w field at z_T is Fourier transformed, the coefficients are multiplied by $N\alpha_0/|k|$, and the result is reverse transformed to obtain the perturbation pressure field at z_T. This serves as the pressure boundary condition for the hydrostatic equation.

Although this condition has been derived from a simplified equation set, Klemp and Durran perform several scale analyses which show that this condition may still be valid in the presence of   linear, rotational, and compressible effects. Preliminary numerical tests have shown this to be the case. Therefore, this boundary condition can be run with any of the three forms of the vertical velocity diagnosis.

The time step of the incompressible model is limited by the speed of the external gravity wave which is partially contained on the large time step. Hence, there is no benefit in the time-splitting mode. However, the incompressible is still usually more efficient than the compressible. The external gravity wave speed is proportional to the height of the model top (z_T). In the *compressible version* with the σ_p-layer, the *effective model top* is much higher than z_T since the variables are defined at $\sigma = .5$. Even though the terms of the σ_p layer responsible for the external wave propagation are on the small time step, the external wave of the main model, which is partially on the large time step, manifests itself in the σ_p layer through the $\partial p_*/\partial x$ term. The net result is that, as z_T become larger (as the external wave speed approaches that of the Lamb wave), the compressible version efficiency approaches that of the incompressible version.

6.1.4 Plans for Further Development

The current plans for the further development of the hydrostatic/non-hydrostatic CSU cloud/mesoscale model include:

  - initialization with observed data fields

  - continued development of a convective parameterization

  - option for a latitude-longitude grid

  - inclusion of the long and shortwave radiation parameterization of Chen and Cotton (1983)

  - inclusion of the planetary boundary layer and surface energy and moisture budget parameterizations of Mahrer and Pielke (1977).

6.2 The Data Assimilation and Analysis Package

As the first step toward the initialization of the CSU cloud/mesoscale model with observed data, a package of data assimilation

and analysis programs has been written. These programs have been designed to be a general and flexible data analysis system which produce data sets that can be used for a variety of purposes ranging from synoptic analysis to the initial and boundary conditions for numerical models.

The package has the ability to assimilate data from several sources. The current version accesses as the basic data sets the NMC 2.5° latitude-longitude mandatory level pressure data, NMC mandatory and significant level rawinsonde report, and USAF 1° average surface elevation data.

The assimilation procedure is as follows:

- The NMC 2.5° pressure data are accessed. These are originally hemispheric fields which are reduced down to a grid that is specified by the user. This grid is then stored as an output file which can be plotted and analyzed by the plotting routines.

- The pressure data grid is interpolated to isentropic surfaces and combined with the surface elevation data to form a complete synoptic scale 2.5° latitude-longitude isentropic data set on the user-specified grid size. This data set is again stored as an output file to be plotted and analyzed if desired.

- The rawinsonde reports are accessed and interpolated to the isentropic surfaces. Options exist at this point to include only a specified number of the NMC reports, eliminate any of the NMC reports, or include any special observations at the analysis time that were not included in the NMC data set.

- Objective analysis are done to the same or different resolution horizontal latitude-longitude grid. This grid could be a coarser grid

for general circulation studies, the same 2.5° for synoptic studies, or a finer resolution for mesoscale analysis or model initialization. The objective analyses are done on the isentropic surface using the Barnes (1973) technique utilizing both the rawinsonde reports and the 2.5° data as observation. Optionally, only the rawinsonde reports can be included in the objective analyses if the data coverage is adequate.

- The final product is an "enhanced" isentropic data set on a latitude-longitude grid which can be plotted and analyzed or used is the initial conditions for a numerical model.

6.3 Plans for Merger with Pielke's Model

Recently an agreement has been reached with Dr. Roger Pielke wherein our modeling group and Dr. Pielke's will jointly use the PP1 preprocessor package and incorporate physical modules developed by Pielke's group as options in the cloud/mesoscale model system. These options would include his surface energy budget model, the ABL parameterization, and possibly radiation schemes.

This, we believe, will reduce our developmental time and further increase the flexibility of the model.

7.0 Investigations of Wind Shears Produced by Precipitating Convective
    Clouds

Strong wind shears are often associated with precipitating
convective cloud downdrafts. Some of the early work in this area was
based on analyses of flight records (Fujita and Byers, 1977; Fujita and
Caracena, 1977) from aircraft which experienced sudden indicated
airspeed drops in the vicinity of thunderstorms. More recent analyses
by Fujita (1981), Fujita and Wakimoto (1981), Mueller and Hildebrand
(1983) and Kessinger et al. (1983) have disclosed that downdrafts and
their associated near surface wind shears can exhibit substantial
temporal variability. Extreme wind shears were found to occur in the
lowest few hundred meters.

Similar variability in low level shears have been analyzed in South
Park, Colorado thunderstorms with an example shown in Fig. 7.1. In this
case a very strong wind shear (~ 30 m/s over a 500-1000 m vertical
distance) occurred along an inflow/outflow boundary. This shear zone
exhibited significantly less magnitude 9 min later. Preliminary
modeling activities with the 3D cloud/mesoscale model have also produced
extreme transient wind shears at the base of downdraft circulations.
The example shown in Fig. 7.2 from model studies reveals significant
vertical shear of horizontal winds in addition to horizontal variations
in horizontal winds at the base of the downdraft.

Further experiments will address the transience and evolution of
such shear zones associated with downdraft circulations.

For extreme shear near the surface (the lowest ~ 1 km), adiabatic
mixed layers are needed. For a given rainfall rate, a deeper ABL will
in general produce stronger downdrafts and associated shear. When the
ABL depth exceeds 3 km as it often does in dry climates, almost any
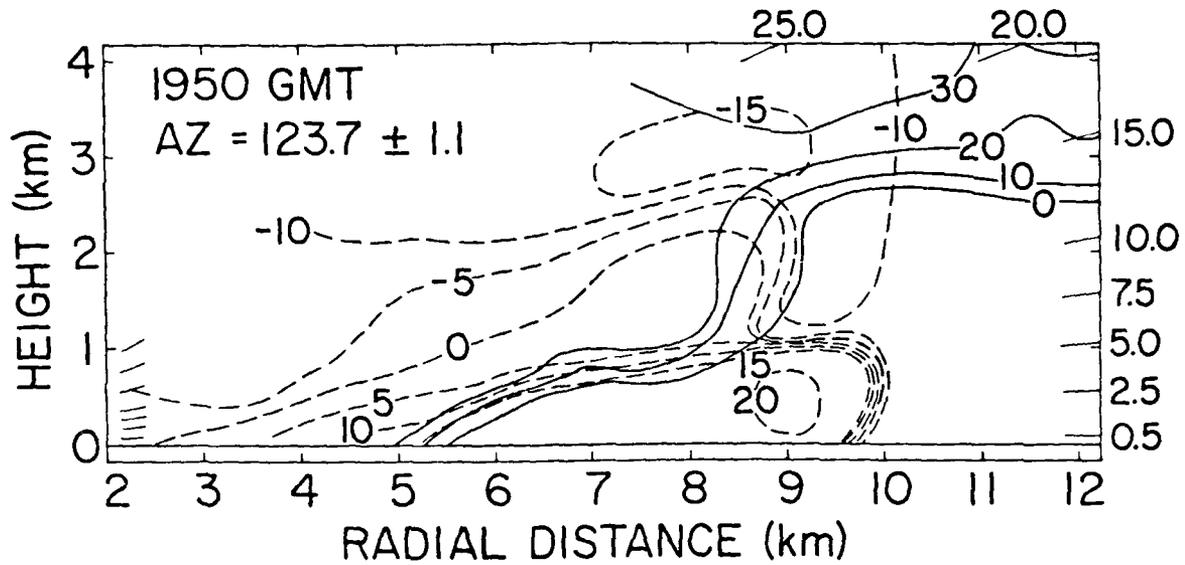
Figure 7.1: Storm relative radial velocity patterns through the core of
a storm over South Park on 4 Aug 1977. Dashed lines are
radial velocity contoured every 10 dBZ. Numbers along top
and right edge are radar elevation in degrees.

SPACE   26 JULY 1977   CASE STUDY (2D) RUN 3

10 M/S   Y =   0.0KM RC.RI.RG.RA TIME=3480.SEC

SPACE   26 JULY 1977   CASE STUDY (2D) RUN 3

10 M/S   Y =   0.0KM   PRESS   TIME=3480.SEC
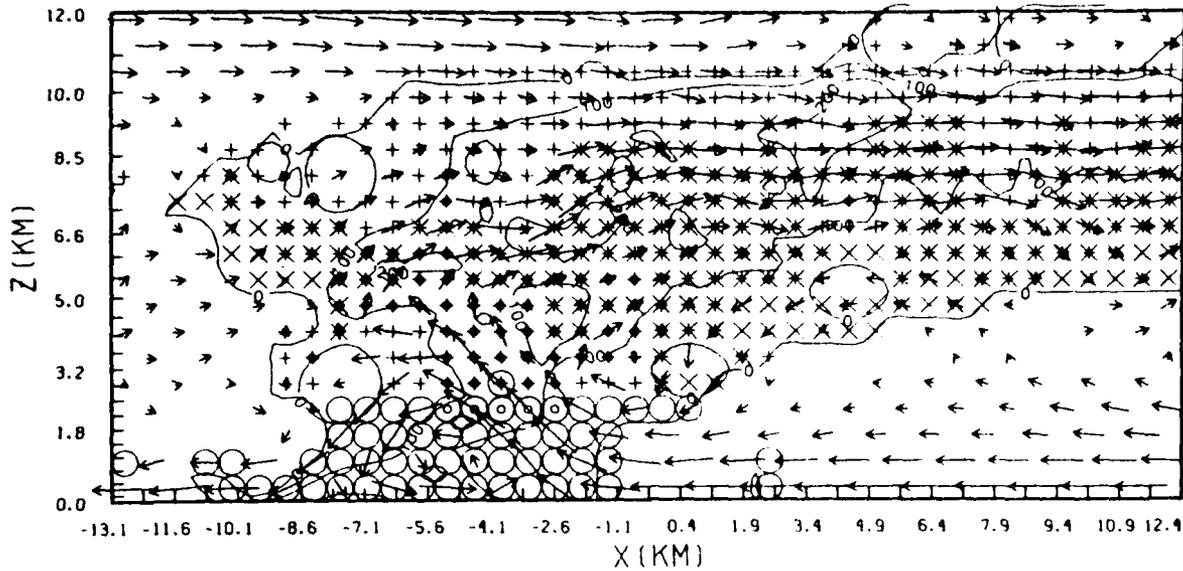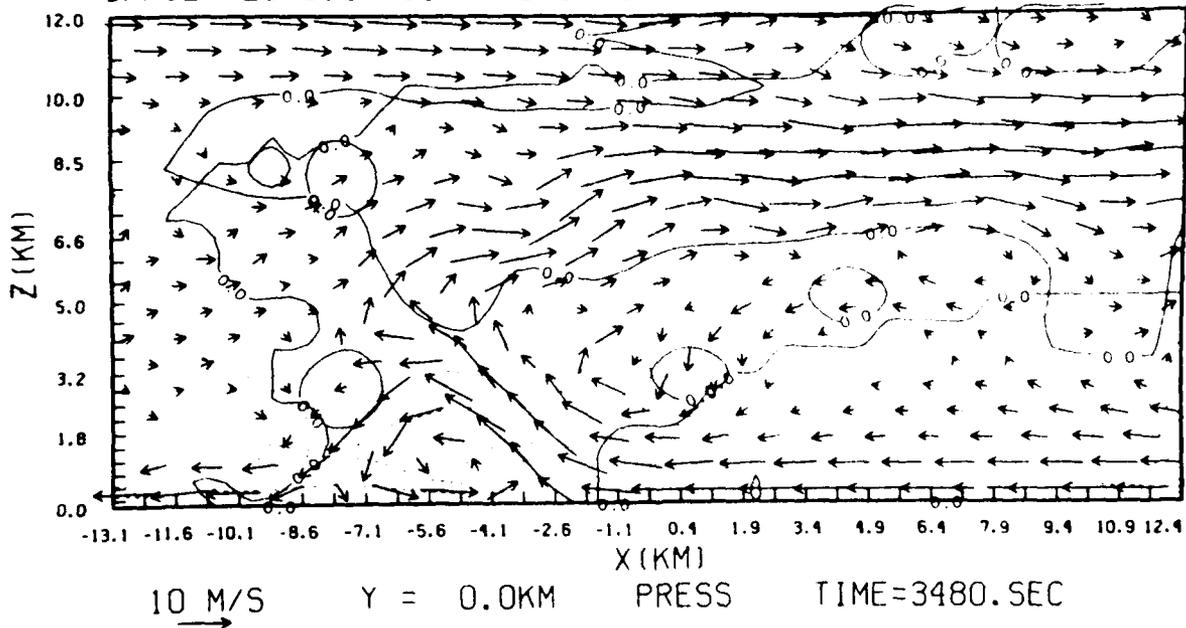
Figure 7.2:   2D simulation initilized with the 26 July 1977 1700 MDT
South Park sounding. Microphysical quantities are plotted
in the top panel, with the symbols representing: 0 -
rainwater, x - graupel, + - ice crystals, and o - cloud
water. In the lower panel perturbation pressure contours
are superimposed on the relative flow field.

precipitating cloud is capable of generating strong downdrafts. For a shallow ABL, downdraft magnitudes tend to be a function of rainfal rate, so that only heavily precipitating systems are likely to produce strong downdrafts and wind shear.

8.0 Recent Changes in the 3D Cloud/Mesoscale Model Sent to Kirtland AFB.

Since January 1983, when the CSU 3D Cloud/Mesoscale model was installed at Kirtland AFB, some major changes have been made. These change are as follows:

8.1 Prediction of p'

Because of apparent instabilities associated with prediction of $\overline{\rho_a}$, we made a change to predict $\overline{p'}$ instead. In doing so, we have used the truncated form of the pressure equation (described by Klemp and Wilhelmson, 1978). Following the notation of Tripoli and Cotton (1982), the pressure equation is now:

$$\frac{\partial p'}{\partial t} + \frac{\gamma p'}{\rho_0 \theta_0} \frac{\partial u_i \rho_0 \theta_0}{\partial x_i} = 0 \qquad (8.1)$$

There are no large time-step terms. The terms dropped were shown by Klemp and Wilhelmson (1978) to have no apparent effect on the meteorological dynamics.

The w equation then becomes:

$$\frac{\partial w}{\partial t} + \frac{1}{\rho_0} \frac{\partial p'}{\partial z} + g \frac{p'}{\gamma p_0}$$
$$= g \left(\frac{\theta'}{\theta_0} + 1.61 r_v r_T\right) + ADV + DIFF. \qquad (8.2)$$

The other equations remain unchanged.

Because the $\frac{\partial \theta'}{\partial z}$ part of $\frac{\partial p'}{\partial z}$ is evaluated on the large time step, this set of equations seems to be capable of a longer large time step, limited only by the $g \frac{\theta'}{\theta_0}$ part of the gravity wave acceleration due to w. Since finite differencing is not involved, the gravity wave associated time step limitation is from the Brunt-Vasallia frequency (N) such that:

$$\Delta t \ L \ \alpha \ (\frac{g}{\theta} \ \frac{\partial \theta}{\partial z})^{1/2} \tag{8.3}$$

where α is some constant. We think α is between 0.2 and 0.1 since we need about 5-10 points in time sampled as a wave goes by to properly resolve it without aliasing.

8.2 Top Boundary Condition

We have added the Klemp and Durran (1983) gravity wave radiation top boundary condition as an option replacing the acoustic radiation top boundary condition option. This option is implemented only for two-dimensional simulations thus far. The extension to 3 dimensions will be relatively trivial. In essence the top boundary condition is

$$w' = \frac{p'g}{|k|} \tag{8.4}$$

where k is the wave number and the refers to the value in wave space. The condition was implemented on the small time step and hence a major recoding of the small time step routine ACOUSTC was made. For the case of the boundary condition use

```
. AC          X

. SE          EX = 1  .
```

In order to implement this change the NZP thermodynamic grid point was redefined to be coincident with the NZ w point. The NZP thermodynamic point is then predicted. In this way a prediction of w' and p' will occur at the same point so Eq. (8.4) can be used. A fast fourier transform routine is called and will also be needed in the Kirtland library.

8.3 Redefinition of DIR2 and DIR3

The definition of DIR2 and DIR3 have been redefined to be NXP and NYP instead of NX and NY. NX and NY are limits to which scalar points are predicted in the X and Y directions, respectively. NXP and NYP are NX + 1 and NY + 1 and DIR2 and DIR3 are the limits to which grid points are stored. This change means X and Y I/O loops must now go one point longer. The change was made to accomodate the introduction of a specified variation in space and time of quantities beyond the integration grid.

8.4 Introduction of Packing Input/Output

The ability to run a core to packed core input/output routine on previously core-contained-only-variables was added. The scheme allows much large domain sizes to be integrated with minimal loss of accuracy.

When packing is activated (activation character "p"), all specified packing variables are placed in memory packed by slabs in ratios of one to one, two, three or four. Each variable may have a different ratio. The variables are unpacked into a slab stencil as with the disk/core I/O scheme. Three or five slab stencils may be specified. NCAR system integer packing routines are used which attempt to limit biased truncation errors. The results are impressive. A four to one packing rate leads to a 15% increase in CPU usage with little difference in the predicted results.

8.5 Globalizing of ADVECT

In order to simplify the advection routine, the flow for x, y and z advection was made into a large global containing the finite difference scheme and the boundary condition logic. This shortens the advection scheme by 60% and makes the remaining logic more readable.

8.6 Changes in MICROPKG

The continuing debugging and development process has led to many changes in the microphysics package. The current package is described in Chapter 4.

9.0 References

Andre, J.C., G. DeMoor, P. Lacarrere, G. Therry and R. DuVachat, 1978: Modeling the 24-hour evolution of the mean and turbulent structures of the planetary boundary-layer model. *J. Atmos. Sci.*, *35*, 1861-1883.

Barnes, S.L., 1973: Mesoscale objective map analysis using weighted time series observations. NOAA Tech. Memo. ERL NSSL-62, 60 pp. [NTIS COM-73-10781].

Battan, L.S., 1973: *Radar Observation of the Atmosphere*. University of Chicago Press, 324 pp.

Blackadar, A.K., 1962: The vertical distribution of wind and turbulent exchange in neutral atmosphere. *J. Geophy. Res.*, *67*, 3095-3102.

Brost, R.A., D.H. Lenschow and J.C. Wyngaard, 1982a: Marine stratocumulus layers. Part I: Mean conditions. *J. Atmos. Sci.*, *39*, 800-817.

Brost, R.A., J.C. Wyngaard, D.H. Lenschow, 1982b: Marine stratocumulus layers. Part II: Turbulence budgets. *J. Atmos. Sci.*, *39*, 818-836.

Chen, C., and W.R. Cotton, 1983b: Numerical experiments with a one-dimensional higher order turbulence model: Simulation of the Wangara Day 33 Case. *Boundary-Layer Meteorol.*, *25*, 375-404.

Chen, C., and W.R. Cotton, 1983a: A one-dimensional simulation of the stratocumulus-capped mixed layer. *Boundary-Layer Meteorol.*, *25*, 289-321.

Chen, C. and W.R. Cotton, 1982: The physics of marine stratocumulus clouds. Cloud Physics Conference, Nov. 15-18, 1982, Chicago, IL, AMS.

Cotton, W.R., 1970: A numerical simulation of precipitation development in supercooled cumuli. Thesis in Meteorology to Pennsylvania State University, September.

Cotton, W.R., M.A. Stephens, T. Nehrkorn, and G.J. Tripoli, 1982: The Colorado State University three-dimensional cloud/mesoscale model - 1982. Part II: An ice phase parameterization. *J. de Rech. Atmos.*, *16*, 295-320.

Cotton, W.R. and R.A. Anthes, 1984: *The Dynamics of Clouds and Mesoscale Meteorological Systems*. Academic Press, Inc., New York, New York, in preparation.

Cunning, J.G., R.I. Sax, R.L. Holle and H. Poor, 1979: Morphology of seeded cloud as determined from triple-doppler radar - A case study. *Ppts. 7th Conf. Inadvertent and Planned Wea. Modif.*, Am. Meteor. Soc., Boston, pp. 142-143.

Deardorff, J. W., 1980: Stratocumulus-capped mixed layer derived from a three-dimensional model. Boundary-Layer Meteorol., 18, pp. 495-527.

Fletcher, N. H., 1962: Physics of Rain Clouds. Cambridge Univ. Press, London, Eng.

Fujita, T.T., and F. Caracena, 1977: An analysis of three weather-related aircraft accidents. Bull. Amer. Meteor. Soc., 58, 1164-1181. Fujita, T. and H. Byers, 1977: Spearhead echo and downdraft in the crash of an airliner. Mon. Wea. Rev., 105, 129-146. Fujita, T., 1981: Tornadoes and downbursts in the context of generalized planetary scales. J. Atmos. Sci., 38, 1511-1534.

Fujita, T. and R.M. Wakimoto, 1981: Five scales of airflow associated with a series of downbursts on 16 July 1980. Mon. Wea. Rev., 109, 1438-1456.

Gordon, G. and J. D. Marwitz, 1981: Secondary ice crystal production in stable orographic clouds over the Sierra Nevada. 8th Conf. on Inad. and Planned Wea. Mod., Reno, Nevada, Oct. 5-7, '81, pp. 62-63.

Hallett, J., and S. C. Mossop, 1974: Production of secondary ice particles during the riming process. Nature, 249, pp. 26-28.

Hallgren, R.E. and C.L. Hosler, 1960: Preliminary results on the aggregation of ice crystals. Geo. Monogr., 5, 257-263.

Heymsfield, A. and J. Parrish, 1979: Techniques employed in the processing of particle size spectra and state parameter data obtained with the T-28 aircraft platform. NCAR/TN-137+IA, Convective Storms Division, National Center for Atmospheric Research, Boulder, CO, 78 pp.

Hosler, C.L. and R.E. Hallgren, 1960: The aggregation of small ice crystals. Disc. Farad. Soc., 30, 200-208.

Hunter, S.M., 1980: 25 July 1976: Mature storm case. Case studies on convective storms, Case study 7, NCAR/TN-153+STR, Convective Storms Division, National Center for Atmospheric Research, Boulder, CO, 72 pp.

Kaimal, J.C., J.C. Wyngaard, D.A. Haugen, O.R. Cote, Y. Izumi, S.J. Caughey, and C.J. Readings, 1976: Turbulence structure in the convective boundary layer. J. Atmos. Sci., 33, 2152-2169.

Kessinger, C., M. Hjelmfelt, and J. Wilson, 1983: Low-level microburst wind structure using Doppler radar and PAM data. Preprints 21st Conf. on Radar Meteorology, AMS, 609-615.

Klemp, J.B. and R.B. Wilhelmson, 1978a: The simulation of three-dimensional convective storm dynamics. J. Atmos Soc., 35, 1070-1096.

Klemp, J.B. and R.B. Wilhelmson, 1978b: Simulations of right- and left-moving storms produced through storm splitting. J. Atmos. Sci., 35, 1097-1110.

Klemp, J.B. and D.R. Durran, 1983: An upper boundary condition permitting internal gravity wave radiation in numerical mesoscale models. Mon. Wea. Rev., 111, 430-444.

Knollenberg, R.G., 1970: The optical array: An alternate to extinction and scattering for particle size measurements. J. Appl. Meteor., 9, 86-103.

Levy, G., 1982: Communication mechanisms in dynamically seeded cumulus clouds. Atmos. Sci. Paper #357, Dept. of Atmos. Sci., Colorado State University, Fort Collins, CO, 80523, 142 pp.

Mahrer, Y. and R.A. Pielke, 1977: A numerical study of the airflow over irregular terrain. Beitrage zur Physik der Atmosphare, 50, 98-113.

Manton, M.J., and W.R. Cotton, 1977: Parameterization of the atmospheric surface layer. J. Atmos. Sci., 34, 331-334.

Mellor, G.L. and T. Yamada, 1974: A hierarchy of turbulence closure models for planetary boundary layers. J. Atmos. Sci., 31, 1791-1806.

Mossop, S. C., 1976: Production of secondary ice particles during the growth of graupel by riming. Quart. J. Roy. Meteorol. Soc., 102, pp. 25-44.

Mueller, C.K. and P.H. Hildebrand, 1983: The structure of a microburst: As observed by ground-based and airborne Doppler radar. Preprints, 21st Conf. on Radar Meteorology, AMS, 602-608.

Passarelli, R.E. and R.C. Srivastava, 1978: A new aspect of snowflake aggregation theory. J. Atmos. Sci., 36, 484-493.

Plank, V.G., R.O. Berther, and A.A. Barnes,Jr., 1980: An improved method for obtaining the water content values of ice hydrometeors from aircraft and radar data. J. Appl. Meteor., 19, 1293-1299.

Rogers, D.C., 1974: The aggregation of natural ice crystals. Revised M.S. Thesis by August H. Auer, Jr., Dept. of Atmospheric Research, University of Wyoming, Laramie, WY.

Sanborn, V.G., ed., 1979: National Hail Research Experiment data catalog (1972-1976). NCAR/TN-148+STR, Convective Storms Division, National Center for Atmospheric Research, Boulder, CO, 271 pp.

Sun, W.-Y., and Y. Ogura, 1980: Modeling the evolution of the convective planetary boundary layer. J. Atmos. Sci., 37, 1558-1572.

Tripoli, G.J. and W.R. Cotton, 1980: A numerical investigation of several factors contributing to the observed variable intensity of deep convection over South Florida. *J. Appl. Meteor.*, 19, 1037-1063.

Tripoli, G.J., and W.R. Cotton, 1982: The Colorado State University three-dimensional cloud/mesoscale model - 1981. Part I: General theoretical framework and sensitivity experiments. *J. de Rech. Atmos.*, 16, 185-220.

Young, K.C., 1974b: A numerical simulation of wintertime, orographic precipitation: Part I. Description of model microphysics and numerical techniques. *J. Atmos. Sci.*, 31, 1735-1748.

Young, K.C., 1974c: A numerical simulation of wintertime, orographic precipitation: Part II. Comparison of natural and agI-seeded conditions. *J. Atmos. Sci.*, 31, 1749-1767.

Zeman, O. and J.L. Lumley, 1976: Modeling buoyancy driven mixed layers. *J. Atmos. Sci.*, 33, 1974-1988.